F.T.H. Liu

Model Assisted Probability of Detection of Phased Array Ultrasonic on an Aircraft Metallic Part

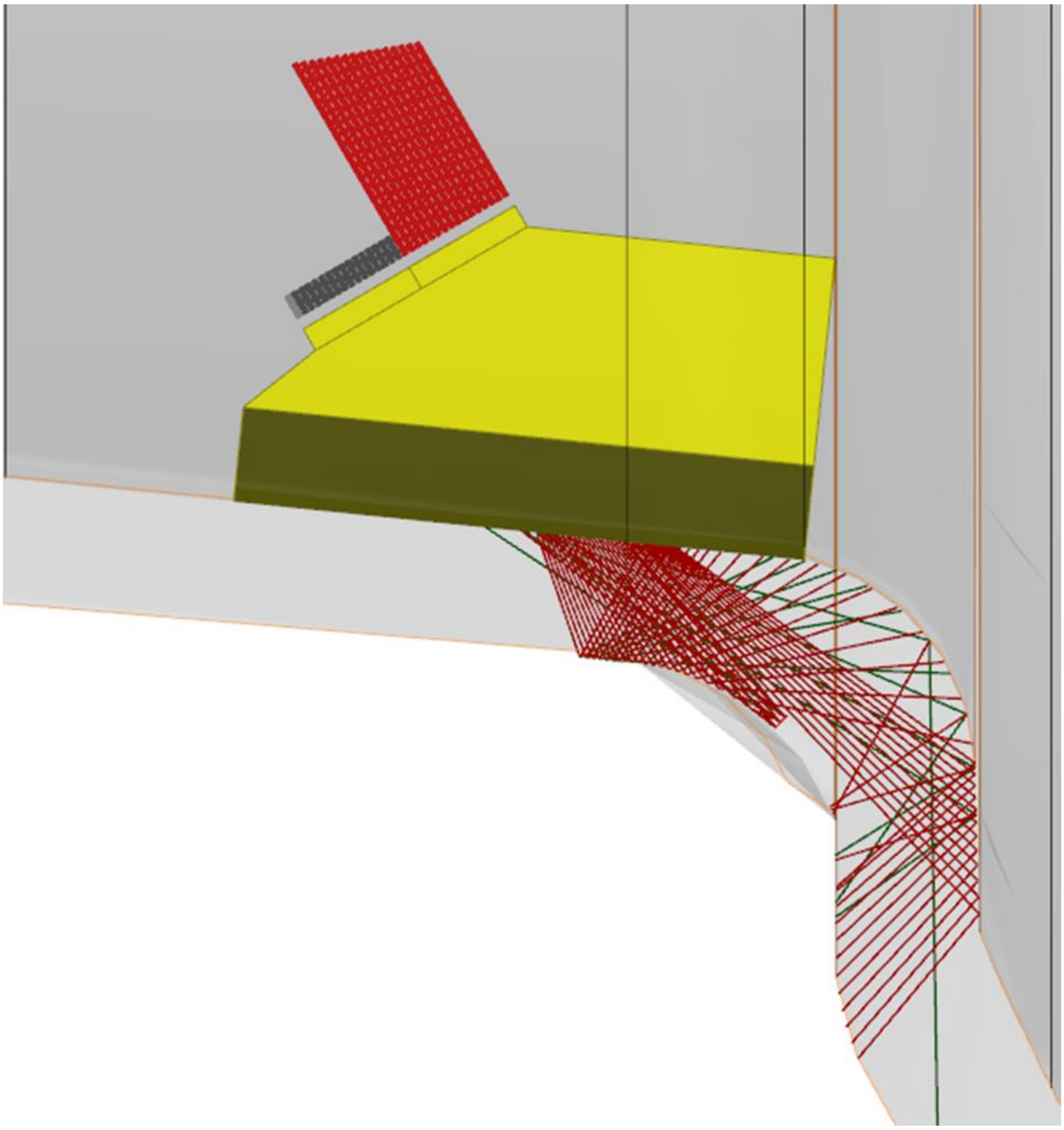

Model Assisted Probability of Detection of Phased Array Ultrasonic on an Aircraft Metallic Part

By

F.T.H. Liu

in partial fulfilment of the requirements for the degree of

Master of Science
in Aerospace Engineering

at the Delft University of Technology,
to be defended publicly on Aerospace Engineering July 18, 2022 at 13:00 PM.

Supervisors:	Dr. R.M. Groves	TU Delft
	Dr. J. Hwang	NLR
Thesis committee:	Dr. I. Langella	TU Delft
	Dr.ir. E. Mooij	TU Delft
	Dr. V. Dhanisetty	NLR

This thesis is confidential and cannot be made public until July 18, 2022.

Preface

This thesis is an original work by Frankie Liu and is part of a research project initiated by the Royal Netherlands Air Force. The research is conducted in cooperation with Delft Technical University (TU Delft) and the Royal Netherlands Aerospace Centre (NLR).

The research was conducted part time as throughout the entire project I was also working full time for Defence Material Organisation (DMO). The project was challenging both time wise and due to the complexity of the topic. However, thanks to the guidance of my supervisors from the TU Delft and the NLR I was able to finalize the research.

I would like to thank my supervisors Dr. Roger Groves, Dr. Jason Hwang and Dr. Vis Dhanisetty from the TU Delft and the NLR for their professional guidance throughout this project. I would also like to thank my NLR colleagues from the NDI department for supporting me performing the physical inspections and guiding me through creating my model used for the simulated inspections. Lastly I would like to thank my DMO colleagues for allowing me to be part of this research project and providing me the equipment required to perform the measurements.

F.T.H. Liu

Ridderkerk, June 2022

Contents

Abstract

In recent years many new non-destructive inspection (NDI) equipment have been developed and have become available on the market. New NDI equipment comes with new possibilities as sensors are getting better at providing inspection results with higher resolutions. In the aviation industry NDI is used intensively as damage tolerance is the preferred design philosophy. However this method requires the user to detect damage on time and take action before it becomes critical. NDI methods are useful assets to be used to assist in inspection procedures as it is capable in detecting type of damage that cannot be detected visually. Some NDI methods even have the capability to “look through” materials like radiography or ultrasound, making it possible to perform inspections without the need of disassembling systems or subsystems.

Usually the Original Equipment Manufacturer (OEM) of the aircraft has documentation that describes how frequently certain inspections need to be performed, what equipment is required, and how the sensors have to be calibrated. Operators have the option to switch to newer or more practical NDI methods . However the operator must then provide a number of test specimens for reliability demonstration purposes so that the entire range of the inspection is covered. Because of this complexity operators are reluctant to switch to new NDI methods even though they may come with a lot of benefits. As a result it is very likely that state of the art NDI methods are being underutilized.

One way to overcome this obstacle is the utilization of model assisted probability of detection (MAPOD) analysis. MAPOD allows the engineer to simulate a large number of inspections on a large number of numerical modelled test specimens, flawed or unflawed, required for reliability demonstration, which is part of the certification process. This reduces the number of physical test specimens required significantly and instead of reserving inspectors to perform the large number of inspections for the reliability demonstration, one can leave the computer running the simulations.

However one cannot just blindly rely on MAPOD analyses as one needs to validate the model used for the MAPOD analysis as the output needs to be representative of real inspection results. Furthermore inspections that are sensitive to human factors are challenging because human factors cannot be fully implemented. Therefore sound engineering judgements need to be made about the output of the model and the range of inspections covered by the model as well as the assumptions made and the limitations need to be known beforehand. If MAPOD can be more widely used to assist in the certification procedure then operators have the potential to use newer and more effective NDI

This research investigate the certification procedure of a new NDI method, assisted by MAPOD. NDI methods are very broad and the techniques are very different among the available NDI methods. Furthermore NDI methods are used in a wide variety of applications from aviation to oil and gas industry. This research is limited to the use of phase array ultrasound inspections on complex aluminium aircraft part.

Abbreviations

ACRONYM	DESCRIPTION
AI	Artificial Intelligence
CAD	Computer-aided Design
DDF	Dynamic Depth Focus
ED	Engineering Disposition
EDM	Electronic discharge machined
FEM	Finite Element Method
FMC	Full Matrix Capture
FSH	Full Screen Height
MAPOD	Model Assisted Probability of Detection
NAN	Not a Number
NDE	Non Destructive Evaluation
NDI	Non Destructive Inspection
NDT	Non Destructive Testing
NLR	Royal NLR - Netherlands Aerospace Centre
PA	Phased Array
PAUT	Phased Array Ultrasound Testing
POD	Probability of Detection
ROI	Region of interest
RNLAF	Royal Netherlands Air Force
SAFT	Synthetic Aperture Focusing Techniques
SNR	Signal to Noise ratio
USAF	United States Air Force
UT	Ultrasound Testing
TFM	Total Focus Method
TOF	Time of Flight

1 Introduction

Non-destructive inspection (NDI) is widely used in different applications, from medical fields [1] to the oil and gas industry [2] to aviation [3]. The main advantage of NDI is that it has the potential to detect the presence of flaws in a test specimen without damaging it [4]. Different NDI inspection methods are available and the development of NDI technology goes rapidly. Examples are the utilization of phased array ultrasound for quantification of low velocity impact in composite plates [5] or the utilization of radiography for examination of friction stir welds of aluminium alloys [6]. However NDI also have disadvantages, as most NDI methods can only be used under certain conditions. An example is that magnetic particle inspections can only be performed on ferromagnetic materials [3].

However before a new NDI method can be used, which can be more reliable, practical or a combination of both, it needs to go through a thorough certification procedure, which requires a lot of inspection results performed on a large number of test specimens. To perform such a large number of inspections is very time consuming and acquiring a large number of test specimens is costly. Therefore operators are reluctant to implement new NDI technology, which is unfortunate as newly developed NDI technology provides a wide array of possibilities, like performing inspections on internal aircraft structures without removing panels using radiography [7] or performing ultrasonic inspections using drones [8].

A potential solution is to certify NDI method with assistance of model simulations. In NDI this is called Model assisted probability of detection (MAPOD). MAPOD reduces the number of test specimens and the number of inspections required for a reliability analysis. This research investigates the possibility of certifying new NDI methods using MAPOD. I will look at what is required to certify an NDI method using MAPOD. For this investigation a case study from the Royal Netherlands Air Force (RNLAF) will be used. This specific case study was chosen because it was a typical example of certifying a new NDI method that will supersede a current inspection method.

1.1 Case study

In the past two incidents happened with one specific aircraft type of the Royal Netherlands Air Force (RNLAF), where the wheel rim has failed. Both cases happened during taxiing and no crew members got injured [9] [10]. The Netherlands Aerospace Centre (NLR) was requested to investigate the root cause of the incidents. The main conclusion of this study reports that it was a result of crack initiation and crack growth due to cyclic loading, and merging of several cracks which decreased the number of cycles to failure compared to other wheel rims of the same specific aircraft within the fleet [9].

Currently the RNLAF has a procedure to inspect this type of wheel rim using eddy current testing [3] after a hard landing, every tire change or every 800 flight hours [9]. On average a tire lasts about 400 flight hours.

In order to perform the eddy current inspection the tire and the wheel rim needs to be removed which is very time consuming. On top of that the NLR recommends the inspection interval to be reviewed as more data is needed to use statistical analysis to determine the failure rate and inspection interval [9].

As performing the Eddy Current inspection on the aircraft wheel rim is very time consuming, the RNLAF would like to use an alternative inspection method. The alternative inspection method utilizes phased array ultrasonic testing (PAUT) as non-destructive testing (NDT) method. PAUT was chosen over other NDT methods as it is the only method that is sensitive enough to detect cracks without the need to remove the wheel. The inspection can thus be performed directly on the aircraft, which is beneficial if the inspection interval is reduced to perform a statistical analysis as described in [10].

Currently the RNLAF has an own procedure to inspect the wheel rim utilizing their PAUT NDT system. The inspection procedure is written in an Engineering Disposition (ED) and is used as initial inspection. If the initial inspection gives a signal response exceeding a threshold, the wheel rim needs to be removed and the conventional Eddy Current inspection will be performed.

The NLR has analysed the RNLAF's inspection procedure utilizing PAUT and concluded that the method is a suitable NDT method to detect cracks in the inspection area of the wheel rim [11]. However this is based on one test specimen of a wheel rim containing one Electrical Discharge Machined (EDM) notch. Further studies need to be performed to find out if this NDT method is capable to detect cracks of different lengths, depths and at different positions within the region of interest (ROI) of the test specimen.

In order to investigate the detectability of cracks with different dimensions at various locations, a large number of test specimens are required. This is practically not feasible due to budget constrain and time limit to produce a large batch of test specimen. An alternative method is to utilize numerical modelling to predict the performance of the NDT method. Numerical modelling allows the user to predict the performances of an NDT method with different variables.

Before the numerical model can be used to analyse the performance of the inspection method from the RNLAF, the accuracy of the numerical model needs to be determined. This can be done by first performing a number of experiments using the NDT equipment from the RNLAF. Those experiments will then be replicated using a simulation tool. The results of the experiments and the simulations are then used to determine the accuracy of the model. Eventual adjustments to the model can be made to improve accuracy. Adjustments which can be made are to optimize the location of the flaw and the position of the wedge, such that it is more in agreement with the physical experiment.

Once the model provides results that are sufficiently representative to actual inspections, a model assisted probability of detection (MAPOD) analysis is performed. The MAPOD analysis shows a minimum crack length that can be detected with the NDT method for a given probability within a confidence bound. Based on the corresponding crack length one can conclude whether the NDT method is capable of detecting a crack length before it reaches the critical crack length of 2 mm [10]. Each individual inspection shall be recorded and a summary of the results shall be given. A guideline how to perform a reliability analysis and how to use MAPOD to assist the analysis can be found in MIL-HDBK-1823A [12].

The case study is used to determine the what is required to use MAPOD to assist a certification process of a new NDI method. The possibility, limitations and obstacles will be identified and discussed in this research.

1.2 Report structure

This report consists of the following chapters: Chapter 2 gives a brief summary of the literature study performed before this research and explains the methods used to answer the research question. Chapter 3 explains the physical experiments performed. In this chapter the specification of the test specimen and the NDI equipment is explained. Chapter 4 explains the model to perform the simulated inspection results whereas chapter 5 compares the actual physical inspections with the simulated inspections and give a judgement about the accuracy of the model. In chapter 6 a POD analysis is performed using a dataset generated by the model with a combination of multiple variables related to the flaw. Chapter 7 describes the certification process of an NDI method in details. Chapter 8 provides an overall conclusion of this research.

2 Literature review and research questions

This chapter gives a brief summary of the literature study and introduce the research question and sub questions. Once the research question and the sub questions are introduced the research methodology to answer the research question will be explained.

2.1 Summary literature study

2.1.1 Aircraft materials and structures

In order to assess the capability of NDT methods an understanding of the properties of materials is required. Since this study is focused on applying NDT on an aircraft part, the focus is limited to aircraft materials. Aircraft materials need to be able to withstand load exerted on the aircraft during operations, needs to be light weighted to enhance performance and be able to withstand extreme temperatures [13].

The next step was to investigate the most commonly used aircraft materials nowadays, which are aluminium and composites. These two materials were thoroughly analysed and compared with each other. Compared to aluminium composite materials are lighter and thus results in higher structural efficiency. Furthermore it has better fatigue resistance and corrosion resistance properties [14]. Major drawbacks of composite materials are the higher costs, anisotropic properties [14]. Since composite materials usually consists of different layers of materials, some NDI techniques, like eddy current or dye penetrant, cannot be used on composite materials.

Operational loads cause the aircraft structure to degrade over time leading to failure. This is not acceptable but cannot be avoided as it can lead to loss of lives or loss of equipment [13]. Therefore possible failure modes are investigated. Common failure modes are fracture and fatigue [15].

To ensure structural integrity different design philosophies can be considered. Two common design philosophies used in the aerospace industry are Safe-life approach and damage tolerance [16]. Safe-life approach assumes that no significant cracking will occur that could lead to failure in the lifetime of an airframe [16]. Damage tolerance assumes that flaws are present in the material and needs to be detected before it reaches critical size [16]. The United States Air Force for example requires an inspection interval at half the time required for the potential crack to grow to a critical size [17]. NDI methods can be used to enhance detectability of flaws which cannot be detected through visual inspection [3].

2.1.2 NDI Techniques

This section gives an overview of possible NDI methods that can be used to detect and remove flaws before it reaches its critical size which can eventually lead to failure. Without the use of NDI methods most damage cannot be detected before it becomes a safety issue [3].

The NDI methods investigated are:

- Visual inspection
- Eddy Current
- Ultrasonic
- Radiography
- Thermography
- Liquid Dye penetrant

These techniques were analysed as they are commonly used in the aerospace industry and are already utilised by the RNLAF. The practicality of each methods was analysed whether it can be applied for the RNLAF's case study.

Visual inspection was out of the question due to the fact that critical crack length is 2 mm, which can be easily missed by the inspector. Eddy current is the current inspection method which is sensitive enough to detect fatigue cracks that are around 2 mm. However it requires the wheel component to be removed before inspection can take place. The same goes for radiography, due to the need of placing a film layer at the opposite side of the X-ray tube. Liquid dye penetrant can only be applied to the side where the crack is present and also require the wheel to be removed. Therefore, based on the analysis Ultrasonic Testing (UT) was the most practical method taking sensitivity and time required to perform the inspection into account.

2.1.3 Fundamentals of Ultrasonic NDI

The fundamentals of UT NDT is further elaborated here as it was chosen as NDI method for the RNLAF to inspect the wheel rim. UT detects flaws in materials by transmitting an ultrasonic pulse through the material. If no flaw is present then the signal will reach the back wall and reflects back to the transmitter. However, when a flaw is present and is in the wave path, part of the energy will be reflected back from the flaw surface. This can be visualized in Figure 2-2 [18]. Piezoelectric transducers are used to generate an ultrasonic wave in the test object through a coupling medium (i.e. liquid) [3]. Coupling materials are needed due to the fact that the acoustic impedance mismatch between air and the solid materials are large. And therefore most energy is reflected and very little is transmitted in the solid materials [18]. Typical pulses ranges from 1 to 15 MHz [19]. The excited ultrasonic waves are either longitudinal waves (L-waves) or shear waves (S-waves) which are shown in Figure 2-1.

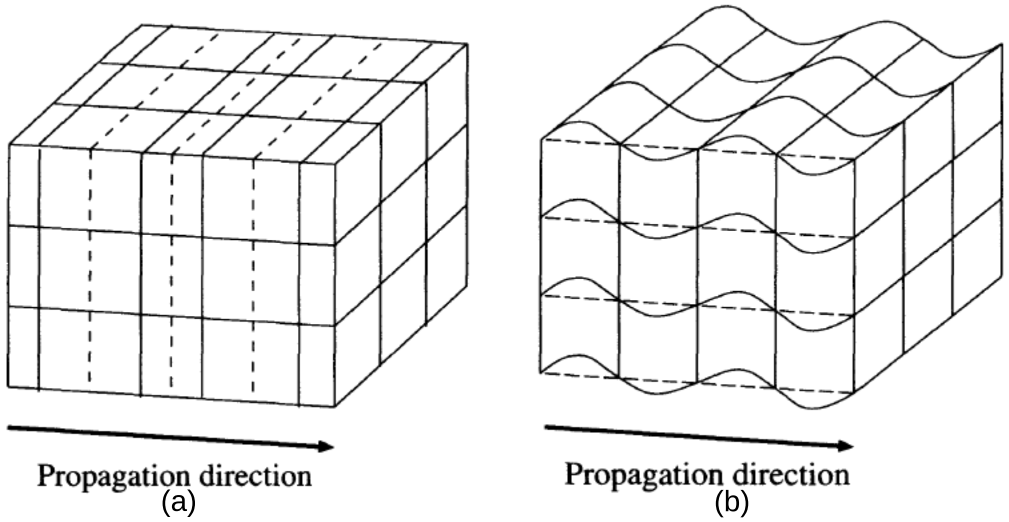

(a) (b)

Figure 2-1 Longitudinal wave (a) and Shear wave (b) [20].

While L-waves can propagate in both liquid and solid materials S-waves can only propagate in solid materials [4].

L-waves and S-waves are most often used in UT. However surface waves and guided waves also exist which are combinations of L-waves and S waves [21]. This research will use S waves because the goal is to detect flaws on a metallic surface with crack lengths in order of millimetres. Therefore high sensitivity is required and shorter wave lengths results in higher sensitivity [22]. S waves are also called transversal waves.

When soundwaves encounter a difference in acoustic impedance, they reflect, scatter and diffract. This can be caused by a crack or a void in the material. This difference in acoustic impedance results in a loss in acoustic intensity. In the most basic form this can be visualized in an A-scan as shown in Figure 2-2, where 3 peaks can be seen. The first peak is the initial pulse (IP). The second peak is the crack echo and the third peak is the back surface echo.

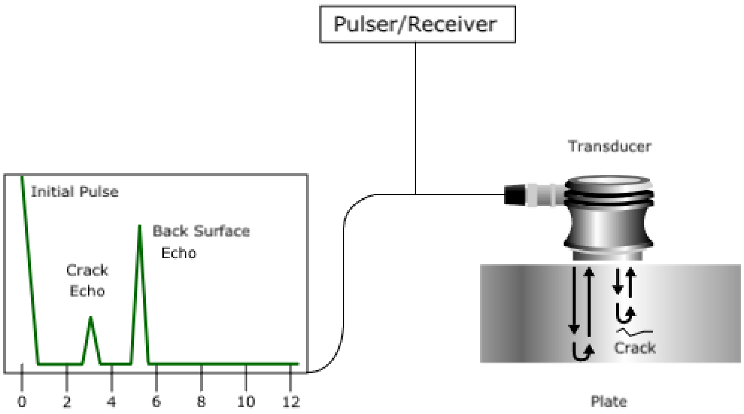

Figure 2-2 An A scan from a typical UT scan [18].

Other ways to present results from UT are B-scans and C-scans. B-scans show the cross sectional view of a specimen where the travel time of the ultrasonic energy is shown in the vertical axis and the location of the transducer is shown in the horizontal axis. A C-scan shows the top view of the test specimen. In order to generate a C-scan of a specimen, the transducer needs to follow a scan pattern to map the entire surface of the specimen. As a result the top view of the specimen can be visualized in a colour map showing the difference in depth. A schematic view of a B-scan and a C-scan is shown in Figure 2-3.

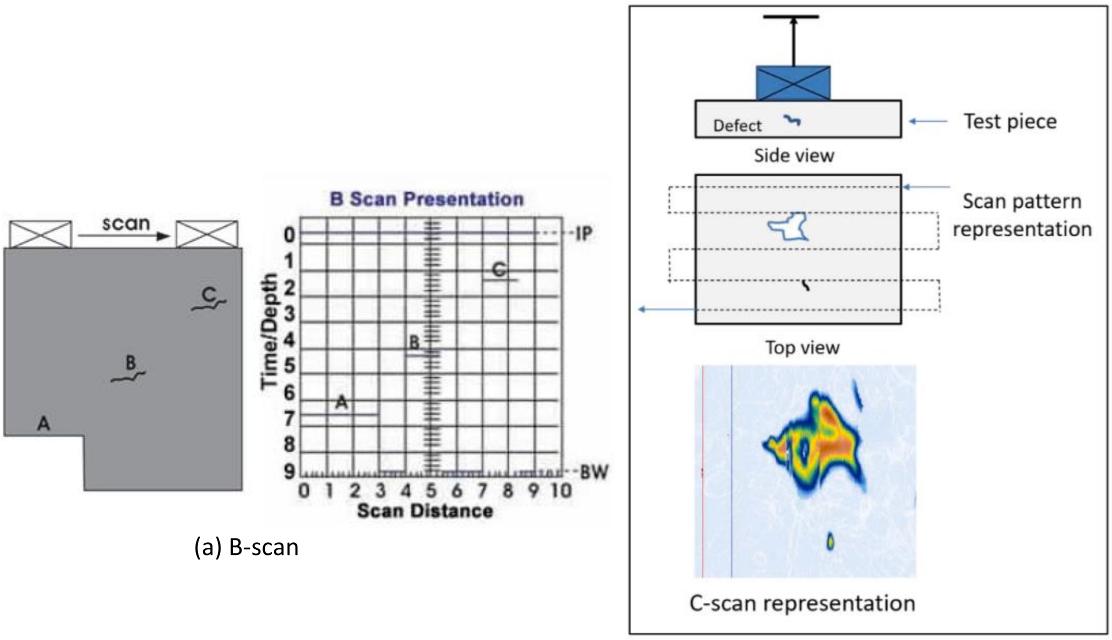

(a) B-scan

(b) C-scan

Figure 2-3 Data representation of (a) a B-scan. The Initial Pulse (IP) and Backwall (BW) can be seen in the B-scan representation. [18] and (b) a C-scan where the scan is performed at the top of the test piece and the entire surface is mapped. Flaws are shown on the colour map. [23].

2.1.3.1 Phased array ultrasonic testing

Phased array ultrasonic testing (PAUT) differs from conventional ultrasonic testing by utilizing a probe containing multiple elements. Each element can generate and receive ultrasound independently. The elements are controlled by a computer. By time delaying the different elements beams can be created. The beam can be steered, scanned, swept and focused electronically [4]. Different scanning patterns can be achieved. Scanning patterns like Electronic scanning, sectoral scanning and dynamic depth focusing can be performed.

Electronic scanning is performed by having a group of active elements scanning at a constant angle following the same focal law at the same time, which is useful for corrosion mapping [19]. The same result can be achieved using conventional UT by performing a raster scan, which is much more time consuming [19]. A visualization of Electronic scanning is shown in Figure 2-4.

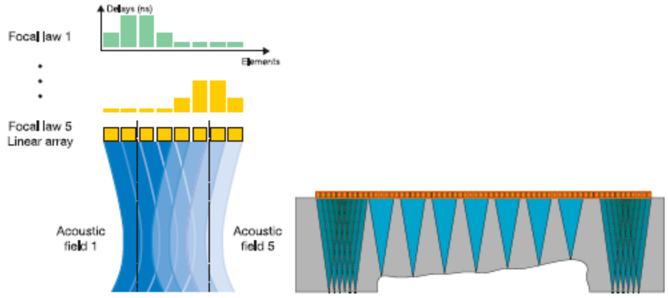

Figure 2-4 Electronic scanning [21].

Sectoral scanning is performed by making a sweep angle through the material. This type of scan is useful to scan objects of complex shapes like turbine blades. The sector being scanned is shown in a 2D view of the cross section of the specimen, called an S-scan [21]. A visualisation of an S-scan is shown in Figure 2-5.

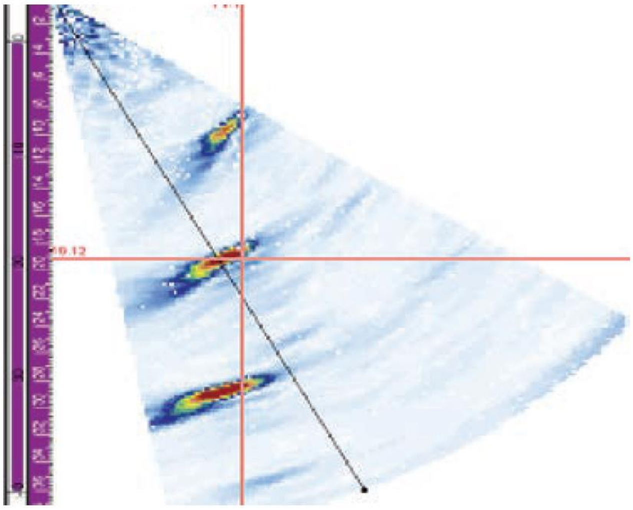

Figure 2-5 An S-scan [19]. In this S-scan 3 flaws can be seen.

Dynamic depth focusing (DDF) changes a single focal point to a focal range. This significantly increases the depth-of-field and Signal to Noise Ratio (SNR). This is achieved by modifying the delay line, gain and excitation of each elements as a function of time [19], which is shown in Figure 2-6

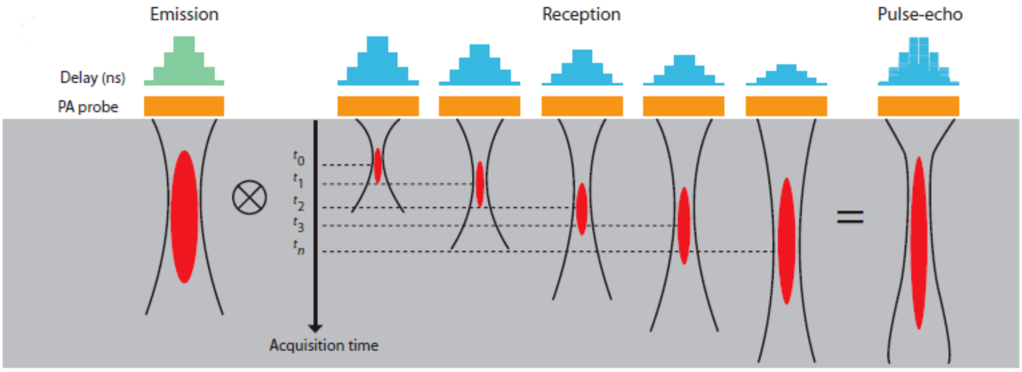

Figure 2-6 Dynamic depth focusing with focus points varying with time, resulting in a focal range [21].

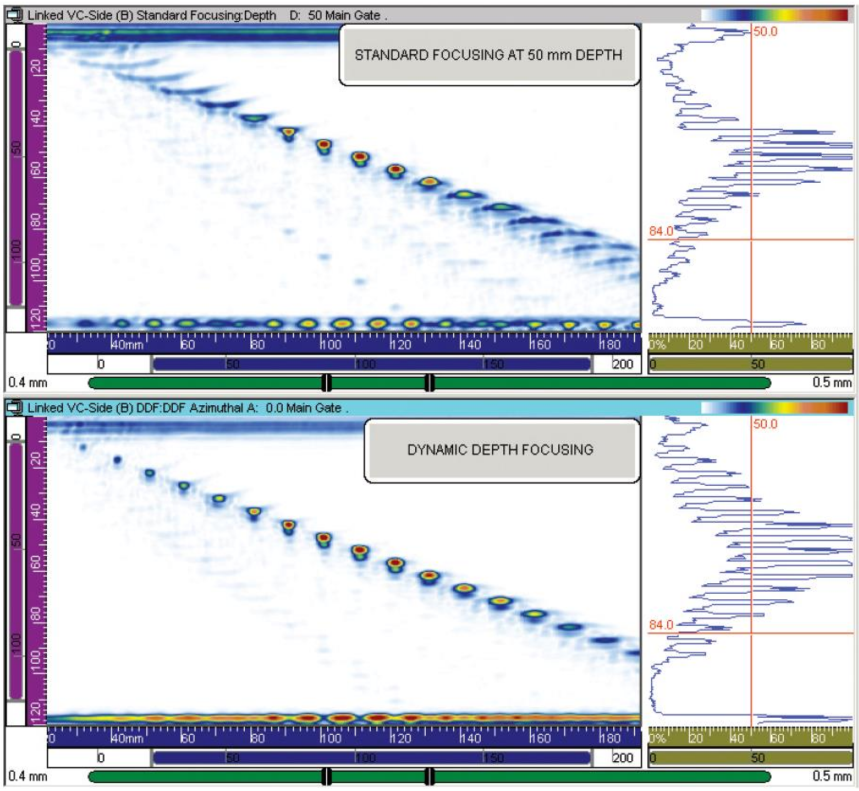

Figure 2-7 Comparison of a standard phased array focusing and a dynamic depth focusing [21].

PAUT has become a popular NDT method due to its speed, flexibility electronic setups and small probe dimensions and it does not require radiation [4] [21]. Furthermore analysis in [24] has shown that PAUT has great potentials in detecting internal damage in composite materials which cannot be seen on the surface. The same study also shows that PAUT is capable of displaying the size and location of defects within a specimen.

So far the PAUT techniques discussed utilized beam forming as basis to perform inspections. A limitation of beam forming technique is that it usually provide one focus zone in the image that appears to be clear and locations within the specimen outside the focus zone appear to be blurry [25]. Techniques that can be used to avoid this problem are Synthetic Aperture Focusing Techniques (SAFT), Full Matrix Capture (FMC), Total Focus Method (TFM) and Dynamic Depth Full Focusing. In SAFT each element of the transducer emits and receives a pulse-echo data, creating an A-scan. Thus a transducer with N elements generate N a scans [26]. FMC works in a similar way, except that when one element generates a pulse, all other elements receive the pulse echo data. Thus N^2 A-scans will be generated [27]. An algorithm like the TFM can be used to generate an image out of the A-scans [28]. Using advanced imagine techniques like SAFT or FMC in combination with TFM requires a lot of data to be processed. As a result inspections are performed much slower than traditional beam forming where results are generated in real-time. However, optimization techniques like Threaded data capture, Look-up tables and Half matrix are available to reduce computation time [29]. Research has been performed to utilize Artificial Intelligence (AI) to analyse FMC pulse-echo signals data without pre-processing [30]. Although [30] showed promising results as a first step towards complete automation process for PAUT, the accuracy of the model needs to be improved by increasing the amount of experimental data which is required for deep learning.

2.1.4 Reliability of NDI procedures

Before a new NDI procedure can be introduced the reliability of the NDI procedure needs to be investigated. This is to make sure that the NDI procedure is capable to detect a flaw before it reaches a critical size. The reliability of an NDI method is expressed in terms of the flaw size having a detection probability of 90%, denoted as a_{90}. However statistical uncertainties related to a_{90} is present. For NDI reliability a_{90} it is required to have a confidence interval of 95%, denoted as $a_{90/95}$ [31].

In aircraft design the design philosophy damage tolerance is often used, where it is assumed that initial flaws exist in materials and will grow over time depending on the load and environmental effects until it reaches the critical flaw size. Therefore flaws must be found before the critical flaw size is reached. The United States Airforce (USAF) requires an inspection at half the time required for the potential crack to grow to critical size [22]. This creates the requirement of the probability of detection (POD).

The POD is usually shown as a function of flaw size, as shown in Figure 2-8 , where an idealized and a realistic POD curve can be seen.

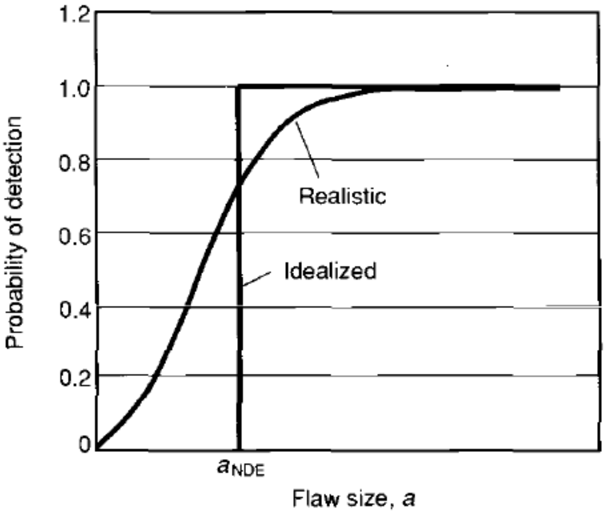

Figure 2-8 Schematic view of the probability of detection curves, ideal versus realistic [22].

In the ideal situation a minimum flaw size exists which can always be detected when the flaw size is larger than this minimum flaw size. However this is not possible in reality as other factors play a role that influences the detectability of a flaw, like orientation and location of defect, noise and human factors. a_{NDE} is the flaw size an NDI method has a POD of 90% with a confidence interval of 95% [32].

In order to obtain the POD for an NDI method a lot of data is required. Data used for a POD model can be either hit/miss data or NDE signal response data [33]. Hit/miss data are binary as data are registered as either a hit or a miss. NDE signal response data, also denoted as $\hat{a}$ data are showing the signal response on flaws. Generally a larger flaw size gives a larger signal response. The USAF MIL-HDBK-1823 [12] recommends that the specimen test set contains at least 60 flaw sites if the system provides only hit/miss results and at least 40 flaw sites if the system provides a quantitative response, $\hat{a}$, to a flaw with size *a* [34].

Once enough empirical data according to [12] has been gathered, POD analysis can be performed to obtain a POD curve as a function of the flaw size *a* (POD(*a*)). Different models are available to obtain a POD(*a*) relationship, but according to several sources like [31], [22]and [33] the log-logistic (or log-odds, or Logit) distribution function is the most acceptable function for a POD(*a*) function. For hit/miss data the POD(*a*) can be written as [35]:

$$POD(a) = \frac{e^{\frac{\pi}{\sqrt{3}}} \cdot \{(\ln a - m)/\sigma\}}{1 + e^{\frac{\pi}{\sqrt{3}}} \cdot \{(\ln a - m)/\sigma\}} \qquad (3.1)$$

in which a is a defect dimension and m and σ are mean and standard deviations. This can be rewritten as:

$$POD(a) = \frac{e^{\alpha + \beta \ln a}}{1 + \alpha + \beta \ln \alpha} \qquad (3.2)$$

which can be rewritten in the simple form as:

$$\ln\left(\frac{POD(a)}{1-POD(a)}\right)=\alpha+\beta\ln\alpha \tag{3.3}$$

where $m=-\frac{\alpha}{\beta}$ and $\sigma=\frac{\pi}{\beta\sqrt{3}}$. α is the intercept parameter and ß is the slope parameter.

The term on the left hand side is called the logarithm of the “odds” (i.e. odds = probability of success/ probability of failure) and it can be shown that

$$\ln(odds)\propto\ln a \tag{3.4}$$

hence the name “the log-odds model” when applied to hit/miss data [33].The particular parameters in the equation are commonly calculated using maximum likelihood methods [33].

For signal response data the following equation can be used [33]:

$$\ln(\hat{a})=\alpha_1+\beta_1\ln(a)+\gamma \tag{3.5}$$

where $\hat{a}$ is the value of the signal strength, *a* is the flaw size and γ represents the error and is normally distributed with zero mean and constant standard deviation [35]. For signal-response data, a flaw is regarded as ‘detected’ if $\hat{a}$ exceeds a pre-defined threshold $\hat{a}_{th}$. The POD(*a*) function can thus be expressed as:

$$POD(a)=probability\ln(\hat{a})>\ln(\hat{a}_{th}) \tag{3.6}$$

Using standard statistical notification this can be written as:

$$POD(a)=1-F\left[\frac{\ln(\hat{a}_{th})-(\alpha_1+\beta_1\ln(a))}{\sigma_\gamma}\right] \tag{3.7}$$

where F is a continuous distributive function (cdf).

With symmetric properties of the Normal Distribution equation, it can be written as [35]:

$$POD(a)=1-F\left[\frac{\ln(a)-((\ln(\hat{a}_{th})-(\alpha_1)/\beta_1)}{\left(\frac{\sigma_\gamma}{\beta_\gamma}\right)}\right] \tag{3.8}$$

which is the cumulative log-normal distribution function with:

$$mean=\mu(a)=\frac{\ln(\hat{a}_{th})-\alpha}{\beta_1} \tag{3.9}$$

and

$$standarddeviation=\sigma=\frac{\sigma_\gamma}{\beta_1} \tag{3.10}$$

The values for the parameters α_1, β_1 and σ_γ are computed from the POD data using the maximum likelihood method [35] [33].

The confidence interval of the POD can be expressed with the following equation [35]:

$$P(p_1\geq p\geq p_2)=C \tag{3.11}$$

Where C is the “confidence level”, p_1 is the lower confidence limit and p_2 is the upper confidence limit. C is assigned to be 95% which is commonly used for POD analysis [32].

2.1.4.1 MAPOD analysis

Efforts have been made since the mid-1990s to perform computational POD [35], also known as Model-Assisted POD (MAPOD). The advantage of using computer simulations to generate data required for POD calculations is that it is less time consuming and less expensive [36]. This is achieved by reducing the number of physical samples required to perform the POD analysis as those are replaced by simulations. A challenge of MAPOD analysis is to make sure that the model provides data that matches with actual inspection data. A guideline on how to use MAPOD for NDI reliability estimation exist which is the MIL-HDBK-1823A, Appendix H [12]. The guideline of how to use MAPOD is summarized in Figure 2-9. It is important to know that MAPOD does not fully replace experimental data as building a model is an iterative process. The model needs to be adjusted such that the simulated data accurately coincides with experimental data.

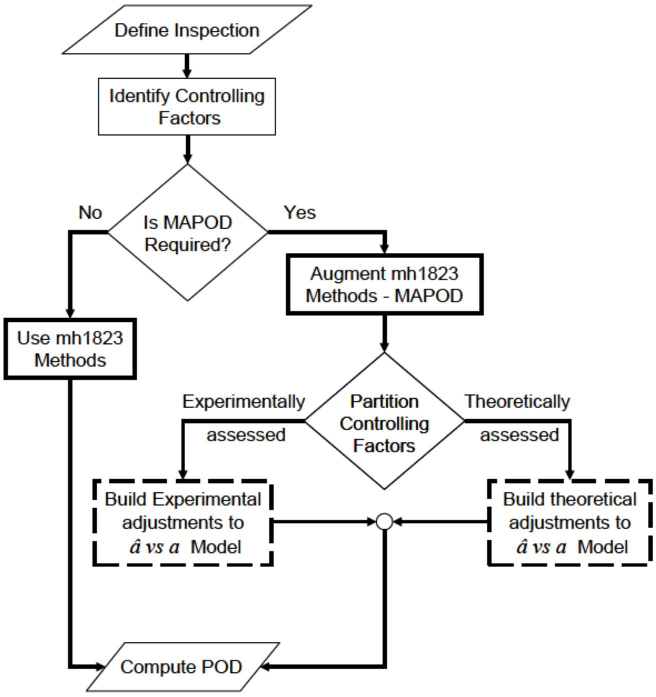

Figure 2-9 Model-assisted POD model building process [12].

MIL-HDBK-1823A Appendix H also states that empirical tests need to be performed so that the results can be analysed to obtain the best mathematical model relating flaw response to flaw size. However for the case study this is not possible as only one test specimen is available containing one notch. Therefore the accuracy of the model shall be determined by relating flaw response to the position of the transducer placed on the test specimen instead.

2.1.5 Simulation of NDI methods

As described in the previous section a lot of empirical data is needed to generate sufficient data to perform an adequate POD analysis. To generate a batch large enough to perform a POD analysis is very costly and time consuming. This is where simulation of NDI method can be used to assist in this process.

Several simulation software on the market are available for UT simulation. In [37] five different simulation software for UT were analysed and reviewed:

- CIVA (French Atomic Energy Commission)
- Imagine3D (UTEX Scientific Instruments Inc.)
- simSUND (Swedish Simulation Centre for NDT)
- UTSIM (Center for Nondestructive Evaluation of Iowa State University)
- VIRTUAL NDE (Electric Power Research Institute)

A trade off was made which software was suitable for the case study of the RNLAF. Based on the criteria that the software must:

- Be able to calculate the interaction between ultrasonic fields and flaws
- Software need to be able to simulate phased array probes
- Software must be able to handle components with complex geometries

Imagine3D was developed for teaching and training and cannot calculate interaction between ultrasonic fields and flaws [38] and thus this software is cannot be used for the research. VIRTUAL NDE is able to simulate interaction with flaws, but the purpose of the software is to train operator for inspections of pipes [39] and so this software is also not suitable. So the only software that could be used were CIVA, SimSUNT and UTSIM. Among these three software, CIVA was determined to be the most capable software due to the fact that it has a wide varieties of inputs of predefined UT probes, a wide variety of selection of materials including isotropic and anisotropic materials and its capability to handle test specimens of complex geometries obtained from 3D CAD drawings [40]. Compared to CIVA the type of flaws SimSunt and UTSIM can analyse are limited [37].

2.2 Research question

Based on the literature study and the case study the following research question was formulated:

How can phased array ultrasound be certified for a complex aluminium aircraft part?

Two sub questions are formulated to answer the research question:

1. What beam forming technique provides the best result for this case considering computation time and accuracy?
2. How can model assisted probability of detection assist in the certification process?

2.3 Research methodology

To answer the research question a case study from the RNLAF is taken as a baseline. The case study will be conducted in cooperation with the Netherlands Aerospace Centre (NLR). The part is aluminium and contains curved sections which are the area of interest (ROI) for NDI. The case study consists of three phases. First a physical experiment will be performed using PAUT equipment provided by the RNLAF. The RNLAF has provided an instruction how the inspection needs to be performed. A limitation to this research is that only one test specimen is available with one notch. Therefore it is not possible to obtain a relationship between flaw size and flaw response or flaw location and flaw response. In order to estimate the accuracy of the model a number of inspection will be performed with a variation of aperture position settings and different guide positions, so that there is a range of inspection data available to compare the simulated inspection data with.

The second step is to construct a model within the CIVA software. Within the CIVA software the physical experiment will be simulated and the results compared. This is to determine the accuracy of the model and the model shall be adjusted if needed to improve accuracy. Adjustment shall be made by positioning the flaw location and the placement of the wedge on the test specimen, such that the simulated result matches with the experimental result.

Finally the model is used to generate a set of empirical data to perform a POD analysis. One output of the POD analysis is to find $a_{90/95}$. The POD analysis is needed in the reliability demonstration, which is part of a further certification process.

Apart from the POD analysis one also needs to analyse the individual inspections to find the variables that have a significant influence on the inspection. An overall conclusion of the inspection and depending on the result of the data analysis, recommendations to improve the inspection procedure might be given.

2.3.1 Phased array NDI

The PAUT inspection is performed using the Olympus Omniscan SX phased array equipment from the RNLAF. The RNLAF already has an inspection procedure for this part with this instrument. The procedure consists of array settings, calibration of the device and the criteria of when further inspection is needed. The procedure of the RNLAF shall be considered as the default case. However inspections with other settings will be performed in this project which can be used to determine the accuracy of the model. The variations are a combination of variation in array setting and wedge position on the specimen. The physical experiment is further elaborated in chapter 3.

2.3.2 NDI simulation

The configuration of the RNLAF shall be modelled in the CIVA software. First the complex aluminium aircraft part will be modelled. The shape will be obtained from a 3D scan performed by the NLR. The next step is to model the phased array ultrasonic device, which is a combination of a transducer and a wedge. The part numbers of both the transducer and the wedge are known and are directly available in the library. Once the model is constructed the positioning of the wedge on the test subject, array settings and simulation settings need to be adjusted. This is explained more in details in chapter 4. In chapter 5 the results of the physical experiments and the simulated results are compared and the accuracy of the model is discussed.

2.3.3 POD analysis

Once the model is determined to be sufficiently accurate, the model will be used to generate empirical data for a POD analysis. The accuracy of the model is determined by the signal strength at the flaw, the shot angle at which the flaw is intersected, and the sound path length. These parameters need to be in agreement with the experimental results. From the procedure of the RNLAF, which gives a threshold in percentage of the full screen height (FSH) at which the aircraft part needs to be removed for further investigation, hit/miss data shall be considered. FSH is the height of the flaw response that can be seen on the PA flaw detector in percentage of the height of the screen. The generated data with a signal strength beyond the threshold are considered as hit while data with a signal strength below the threshold is considered as a miss.

Although CIVA has the capability to perform POD analyses, the POD analyses will be performed in MATLAB. This is because the method CIVA uses to perform the POD analysis is unknown. The method used to obtain the POD for this specific case is the POD curves for hit/miss data described in section 6.2. For the POD analysis the confidence bound of 95% will be included.

Multiple sets datasets are used for POD analysis to test the robustness of the POD model in Matlab.

2.3.4 Certification of the new NDI method using MAPOD

In order to implement a new NDI method, one needs to certify the new method and make sure that the new method is at least as capable as the current method. In order to do that a lot of tests need to performed to simulate the possible conditions the NDI method is being performed. A trivial variable is the parameter of the flaw within a material, like size, orientation and location. But other factors play a role, like environment at conditions and human factors.

Normally there are limited test specimens with unique flaw parameters available, insufficient to perform a reliability within the entire range of the inspection procedure. Gathering or fabricating a large pool of test specimens is costly and time consuming. To overcome this obstacle, MAPOD can provide a solution. Instead of performing a large number of physical experiments, a large number of simulations can be performed which then can be used to assist the certification process. MAPOD has the potential to save a significant amount of time and money as it only requires a computer to run the simulations.

However before MAPOD can even be used, the model that is used to perform the MAPOD analysis needs to be validated against reality as the output of the model needs to predict the outcome of an inspection with sufficient accuracy within a range the inspection is to be performed.

Once the model is validated against real experimental data, a data set is generated for a POD analysis. One needs to determine what variables shall be included in the dataset. The POD analysis performed on the simulated data set shall be used to assist the certification procedure of the NDI method for this case study. Based on the findings on this case study an answer to the research question of how to use MAPOD as a certification method for phased array ultrasound inspections on complex aluminium aircraft parts. The case study where MAPOD is used is supported with experiments so that one can determine how much MAPOD be implemented for certification purposes without the need of using traditional methods which requires a lot of specimens.

3 Physical experiment

This chapter discusses the physical experiment performed by the NLR using the equipment of the RNLAF to determine its capability to detect cracks located on inaccessible side of the aircraft part. The shape of the aircraft wheel is complex as it contains curves, making the phased array inspection more difficult to perform compared with a flat surface.

At first the equipment used for the various inspection will is explained in this chapter. This includes the Phased array (PA) ultrasonic flaw detector, the transducer and the wedge. Also the test specimen and the flaw specification within the will be explained. The next step is to explain the way the inspection will be performed, including how the equipment needs to be calibrated beforehand. Afterwards the test matrix consisting of the various inspections is discussed. The variables of the inspections within the test matrix are a variation in axial positions of the transducer and different aperture positions. Eventually the results of the inspections will be presented with a brief discussion about the results.

3.1 Equipment used

This section describes the equipment used to perform experiments on the aircraft part. The equipment was provided by the RNLAF. The equipment consists of a PA flaw detector including software, a linear transducer and a wedge that should match with the curvature of the complex metallic aircraft part. The equipment are discussed briefly.

3.1.1 PA ultrasonic flaw detector

The PA ultrasonic flaw detector used for the experiment is the Olympus OmniScan SX, shown in Figure 3-1. The OmniScan SX is a portable device with a maximum of 16 PA channels allowing 16 elements to be used simultaneously. The software on the device is the MXU 4.4R5. The device can be used to perform linear scans, sectoral scans and compound scans which is a combination of a linear scan and a sectoral scan. The compound scan utilizes every elements of the transducer.

The application of the RNLAF is to detect cracks within a certain region of interest. This can be achieved by performing a sweep scan. Thus the sectoral scan is used for this application.

Figure 3-1 The Olympus OmniScan SX, which is used to perform the experiment for the RNLAF.

3.1.2 Linear transducer and wedge

3.1.2.1 Transducer

The linear phased array transducer used for this inspection is an Olympus Universal probe with part number 10L32-A10. The specification and dimension of this transducer is shown in Table 3-1.

Table 3-1 Specification and dimension of the transducer [41].

Frequency [MHz]	Number of elements	Pitch [mm]	Active Aperture [mm]	Elevation [mm]	External Dimensions [mm]		
					L	W	H
10	32	0.31	9.9	7.0	23	16	20

3.1.2.2 Wedge

The wedge used for the experiment is a modified SA10-N55S-AID4, from Olympus. The specification and dimension of this wedge is shown in Table 3-2. AID4 of the part number stands for Axial Inner Diameter. The number 4 corresponds to a curvature diameter between 88.9 and 101.6 mm [42].

The wedge used by the RNLAF has a curvature diameter of 101.6 mm, which is much less of the curvature diameter of the aircraft part. Consequently when the inspection is performed, a huge wobble is present due to the mismatch in curvature diameter. This is partially corrected by using tapes, see section 3.2.2. Ideally a new wedge with correct dimensions should be acquired. However due to time and budget constraints of this project, this could not have been achieved.

A guide is mounted on the wedge to fix the axial direction of the wedge when performing the inspection. This is to make sure that the wedge will always be focused of the region of interest when performing the inspection. The transducer, wedge and guide are shown in Figure 3-2.

Table 3-2 Specification and dimension of the wedge [42].

Part Number	Nominal Refracted Angle (in Steel)	Material	Recommended Sweep [°]	Probe Orientation	Wedge dimension* [mm]		
					L	W	H
SA10-N55S-AID4	55° Shear waves	Perspex	30 to 70	Normal	23	40	14

Figure 3-2 The linear PA transducer, wedge and guide used for the inspection.

3.1.3 Reference material

The RNLAF provide a section of the entire part with one notch in the region of interest, shown in Figure 3-3. The location of the notch is and the region of interest are highlighted. The dimensions of the notch are shown in Table 3-3 and is located exactly at the centre of the radius.

Table 3-3 Flaw specification reference material.

Depth [inches]	Length [inches]	Width [inches]
0.0294	0.0980	0.0042

Figure 3-3 View of the used as reference material provided by the RNLAF. The location of the notch and the region of interest are highlighted in the photo.

3.2 Test set up

The test is performed by placing the wedge directly on the opposite side at the location where the notch is present, as shown in Figure 3-4, which is the opposite side of the location shown in Figure 3-3.

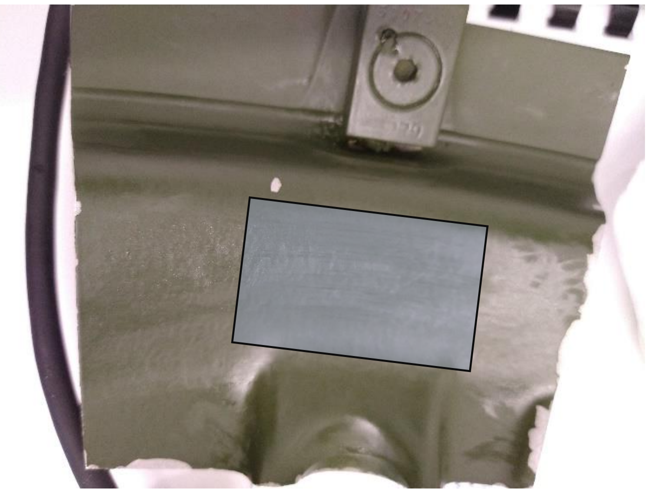

Figure 3-4 The side of the part where the wedge is placed on

The wedge consists of a guide that prevents it from moving in the axial direction of the test specimen. However it can move freely along the radial direction, as shown in Figure 3-5. Consequently, one has to move the wedge along the radial direction for every inspection to find the notch. Since a large number of tests need to be performed, this can be cumbersome. To make the process smoother, tapes are attached on the test specimen as markings to assist the testing procedure. This is shown in Figure 3-6 where the wedge should be positioned between the two pieces of tape.

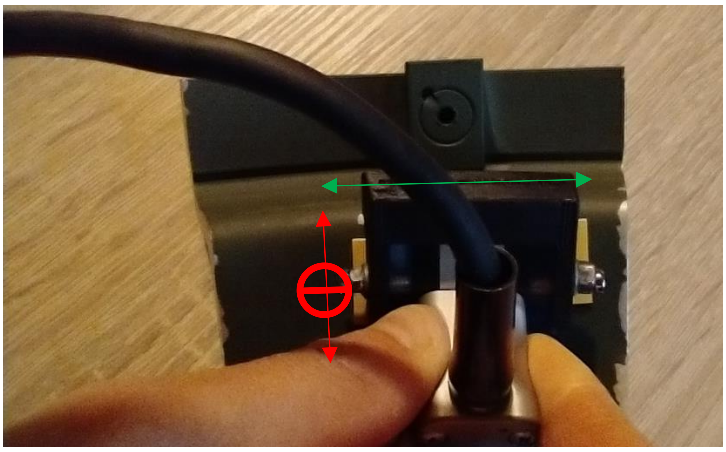

Figure 3-5 Test set up: The wedge is placed on the test specimen. The guide prevents the wedge from moving in the axial direction (red arrow). However the wedge can move freely in along the radial direction (green arrow).

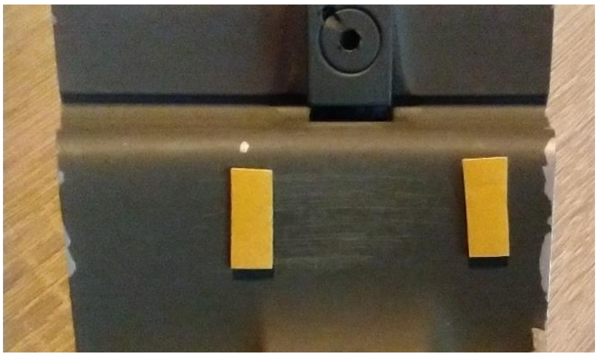

Figure 3-6 Tape is attached on the test specimen to assist the placement of the wedge in the radial direction.

3.2.1 Variation along the axial direction

One of the objectives is to investigate the signal response at the notch along the axial direction. This was achieved by putting layers of stacked posted notes between the guide and the test specimen when the wedge is positioned forward with respect to the guide position as shown in Figure 3-7 (a) or backward with respect to the guide position as shown in Figure 3-7 (b). Each layer of stacked posted notes is 1 mm.

Figure 3-7 Layers of paper put between the guide to adjust the lateral position of the wedge. (a): Layers of paper added in a way that the wedge is positioned in a forward position (+) with respect to the default position. (b): Layers of paper added to move the wedge in a backward position (-) with respect to the default position.

3.2.2 Measurement consistency

The mismatch between the wedge curvature and the test specimen curvature resulted in the presence of a wobble. The presence of the wobble hampers the consistency of the measurements. The effect of the wobbling effect is shown in Figure 3-8 [11].

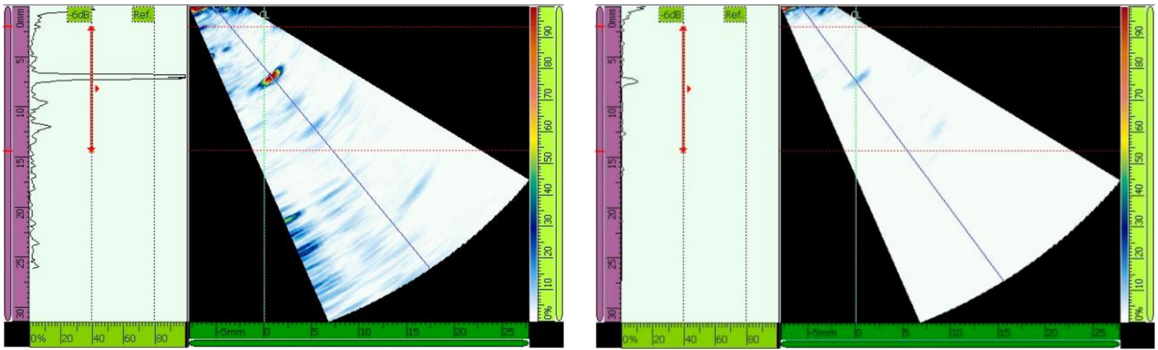

(a) (a)

Figure 3-8 (a) Optimal position without the presence of the wobble. (b) Presence of a wobble [11].

In order to mitigate the wobbling effect and thus to improve consistency tapes are applied to the side of the wedge as shown in Figure 3-9. The effect of the presence of a wobble is further analysed by simulations. The results can be found in Appendix B.1.

Figure 3-9 Tapes are applied on the side of the wedge to mitigate the wobbling effect and thus to improve consistency.

3.2.3 Phased array settings

For the inspection a sectoral scan will be used. This is because the sectorial scan is the only scanning method that is capable to map the ROI of the part. For the sectoral scan, the minimum angle and maximum angle of the beam can be selected. In order to sweep through the area of interest, a beam angle between 25° and 60° shall be used. A schematic view of this inspection is shown in Figure 3-10.

The default array settings are defined in the inspection instruction. However a number of inspections with different array settings were performed which will be used to compare the simulated results with. To make different settings comparable, one default case was used, which is the case the RNLAF uses is selected. Other cases are compared with the default case.

3.2.3.1 Default settings

The default settings the RNLAF uses is an aperture of 16 elements, using the elements 17 to 32. The location of elements are visualized in Figure 3-10. The default wedge position is the position fixed by the guide.

For the default settings a gain is selected so that the signal response at the notch is approximately 80% of the full screen height (FSH). This is in accordance with the procedures of the RNLAF. The gain chosen is 27 dB, which gives a FSH of 74.51 %. The default settings are summarized in Table 3-4. The result is shown in Figure 3-11.

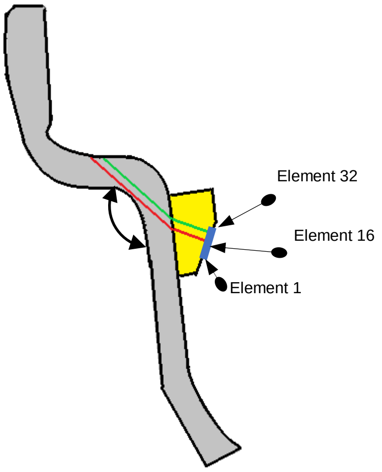

Figure 3-10 Schematic view of a sectoral scan performed on the aircraft wheel. A beam if formed that sweeps through the region of interest for flaw detection. Furthermore the element numbers are shown in this this figure.

Table 3-4 Default phased array settings

Aperture size [# elements]	16
Aperture position [First element number to last element number]	17-32
Sweep angle [deg]	25-60
Gain [dB]	27

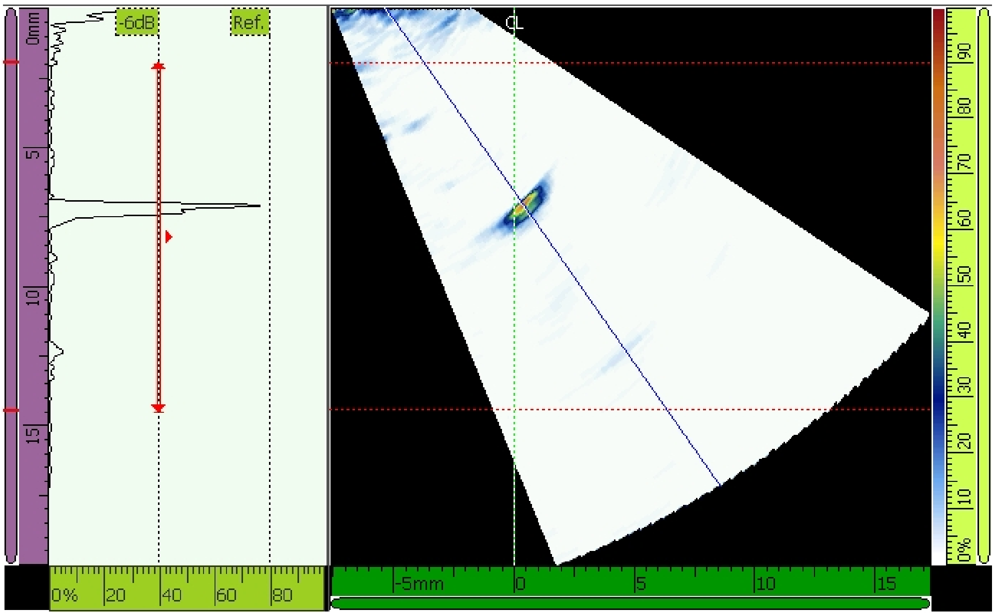

Figure 3-11 Experimental result default settings.

3.3 Test matrix

This section describes the different tests that have been performed. The test specimen consists only one EDM notch so the size and position of the notch remains constant. However the array settings and the wedge position can be varied.

In order to determine the accuracy of the numerical model, which is discussed in chapter 4, a number of experimental results are required. It was determined in [11] that a higher aperture size gives better results. The PAUT system of the RNLAF is capable in handling an aperture size of up to 16 elements. Therefore the aperture size is kept constant of 16 elements. Three different element positions are considered, in combination with 11 different wedge positions. A total of 33 experiments are performed. The experiments are summarized in Table 3-5. The element positions and wedge positions are shown in Figure 3-10 and Figure 3-7 respectively.

3.4 Results

This section shows the results from the test matrix in Table 3-5. The result consists of the signal strength at the flaw location, the shot angle which is the angle where the signal strength is the highest, the sound path, which is the line from where the sound enters the material to when the sound reaches the flaw, and the time of flight (TOF) to the flaw. These parameters can be extracted from the raw data, generated by the Olympus SX, using CIVA. A few examples of the results can be visualised in Figure 3-12. The results of the test matrix are summarised in Table 3-5. The S scans of every single test can be found in Appendix A where the physical inspection results are put next to the simulated inspection results. In some inspections the value Not a Number (NAN) can be seen. This is because the flaw could not be detected.

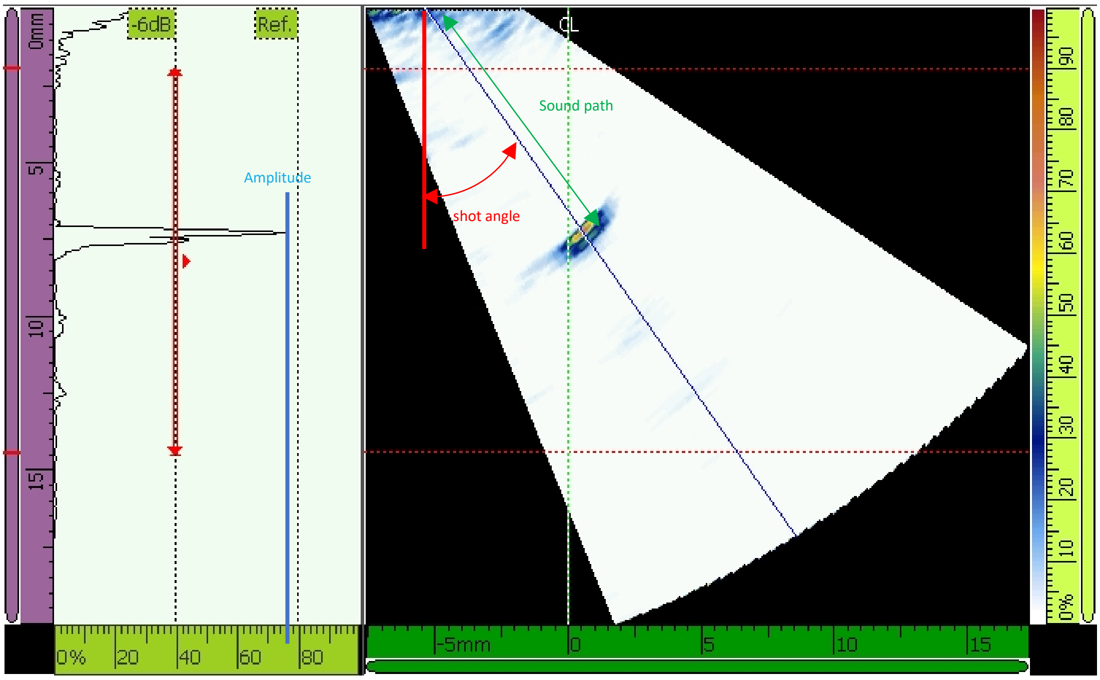

Figure 3-12 Result of test nr 5. This figure provides a visualization of the parameters obtained from experiments.

Table 3-5 Test matrix and results of the experiments. NAN is shown in test cases where the flaw could not be detected during the experiment.

Test nr	Aperture size	Element positions	Wedge position	Signal strength [%]	Shot angle [deg]	Sound path [mm]	TOF [μs]
1	16	17 - 32	Guide -4 mm	55.69	47	9.579	6.18
2	16	17 - 32	Guide -3 mm	59.61	47	9.579	6.18
3	16	17 - 32	Guide -2 mm	63.53	44	9.486	6.12
4	16	17 - 32	Guide -1 mm	72.55	42	9.3	6
5	16	17 - 32	Guide	74.51	39	9.3	6
6	16	17 - 32	Guide +1 mm	70.59	39	9.393	6.06
7	16	17 - 32	Guide +2 mm	64.71	33	8.51	5.49
8	16	17 - 32	Guide +3 mm	51.77	31	8.417	5.43
9	16	17 - 32	Guide +4 mm	33.33	29	8.417	5.43
10	16	17 - 32	Guide +5 mm	NAN	NAN	NAN	NAN
11	16	17 - 32	Guide +6 mm	NAN	NAN	NAN	NAN
12	16	8 - 23	Guide -4 mm	NAN	NAN	NAN	NAN
13	16	8 - 23	Guide -3 mm	NAN	NAN	NAN	NAN
14	16	8 - 23	Guide -2 mm	49.8	53	10.416	6.72
15	16	8 - 23	Guide -1 mm	30.2	47	10.835	6.99
16	16	8 - 23	Guide	53.73	48	10.277	6.63
17	16	8 - 23	Guide +1 mm	47.84	44	9.998	6.45
18	16	8 - 23	Guide +2 mm	66.67	41	9.579	6.18
19	16	8 - 23	Guide +3 mm	78.43	38	8.928	5.76
20	16	8 - 23	Guide +4 mm	76.47	34	8.835	5.7
21	16	8 - 23	Guide +5 mm	61.57	35	8.556	5.52
22	16	8 - 23	Guide +6 mm	25.49	29	8.463	5.46
23	16	1 - 16	Guide -4 mm	NAN	NAN	NAN	NAN
24	16	1 - 16	Guide -3 mm	NAN	NAN	NAN	NAN
25	16	1 - 16	Guide -2 mm	NAN	NAN	NAN	NAN
26	16	1 - 16	Guide -1 mm	NAN	NAN	NAN	NAN
27	16	1 - 16	Guide	19.61	53	12.043	7.77
28	16	1 - 16	Guide +1 mm	29.41	49	11.718	7.56
29	16	1 - 16	Guide +2 mm	34.11	47	11.068	7.14
30	16	1 - 16	Guide +3 mm	61.57	43	10.23	6.6
31	16	1 - 16	Guide +4 mm	77.26	42	9.626	6.21
32	16	1 - 16	Guide +5 mm	81.18	40	9.021	5.82
33	16	1 - 16	Guide +6 mm	87.06	37	8.51	5.49

3.5 Discussion and conclusion

The results show that both the aperture position and the wedge position influences the signal strength, shot angle, sound path and TOF. The results are expected as the aperture position and the wedge position influences the density of soundwaves going through the flaw. The shot angle, sound path and TOF are dependent on the location of the transducer with respect to the flaw. Figure 3-13 shows a comparison between test nr 1, 5 and 9. It can be seen that the signal strength is stronger when the flaw appears at the middle of the section. This is expected as more sound waves will pass through the flaw compared with when the flaw appears at the edge of the section.

The 33 test cases will be used to determine the accuracy of the model which is eventually used to generate result used for a MAPOD analysis.

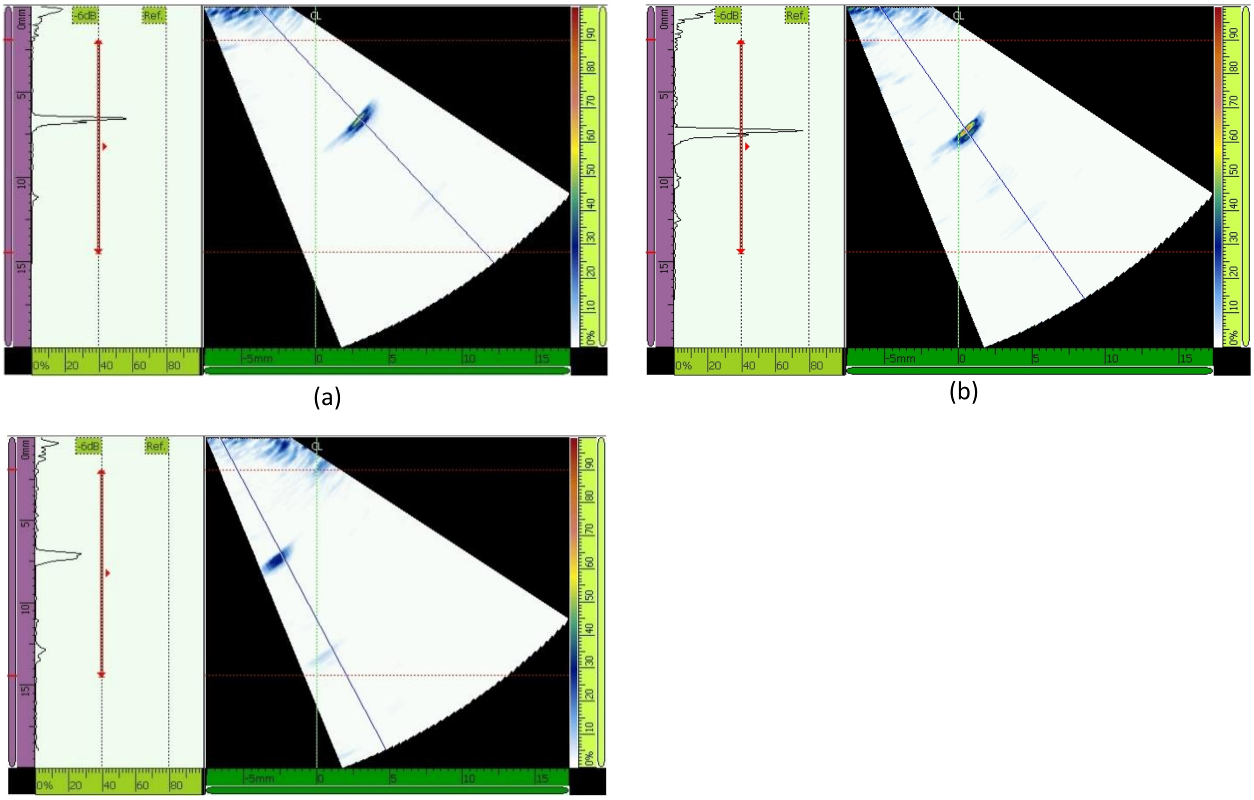

(a)

(b)

(c)

Figure 3-13 Results of test nr 1 (a), test nr 5 (b) and test nr 9 (c). Note that the signal strength at the flaw location is the strongest when the flaw appears in the middle of the section (around shot angle 40). At this position most of the sound waves will get through to the flaw, resulting in a higher signal strength.

4 NDT Simulation

Along with the physical inspections which were described in chapter 3, simulated inspections are performed. For the simulation experiments, the conditions and settings are kept as close to the physical experiments as possible. This includes the geometry and material specifications of the test specimen, the simulation of the PA flaw detector, which the transducer and wedge needs to be modelled according to the physical equipment. The simulations are performed using the CIVA software, developed by Extende. The entire test matrix shown in Table 3-5 shall be simulated. The differences in results will be discussed in chapter 5.

4.1 Test specimen model

The test specimen model was created by making a 3D scan of the part shown in Figure 3-4. The 3D scan is shown in Figure 4-1. The 3D file is in .stl format. However the CIVA software can only use .step files. Since it was not possible to directly convert .stl files to .step files, the 3D model used for the CIVA model needs to be drawn manually. However the 3D scan makes the drawing process easier as it provides the exact dimension of the actual wheel segment. The model which is eventually used in CIVA is shown in Figure 4-2.

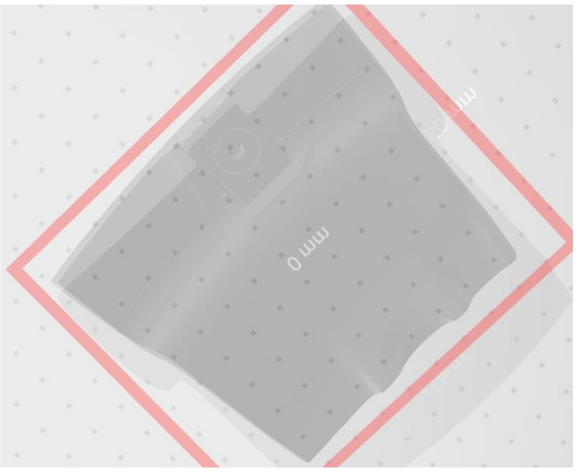

Figure 4-1 Result of the 3D scan of the part segment. This 3D will eventually be used for the NDT model. This is the raw data from the 3D scan and will be used to create the 3D model of the test specimen required in CIVA.

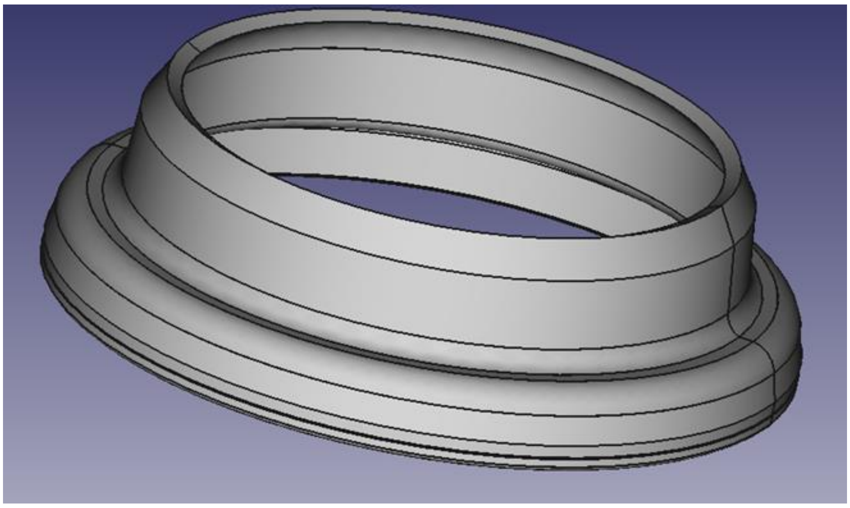

Figure 4-2 The 3D model of the test specimen which is eventually used for the CIVA model.

4.2 Phased array equipment model

To model the PA ultrasound system, the specification of the transducer and the wedge inputted to the software. The CIVA software comes with a library consisting of many commonly used transducers and wedges, including the transducer and wedge used by the RNLAF.

The transducer model, which is the Olympus 10L32-A10 can be directly taken from the library without modifications in the settings.

The wedge is however more challenging as the dimensions of the wedge used by the RNLAF deviates from the default Olympus wedge. This is due to the curvature present on the wedge. The part number of the wedge is SA10-N55S-AID4, which comes with a range in diameter. The problem was solved by making a 3D scan of the wedge to measure the actual diameter, which is discussed in the upcoming sessions.

4.3 CIVA model

Simulations are performed in the CIVA software that matches with the physical experiment as close as possible. First the specimen needs to be defined, which can be imported from a computer aided design (CAD) model. Then the probe and wedge dimensions and parameters need to be defined. A geographic view of the model is shown in Figure 4-3.

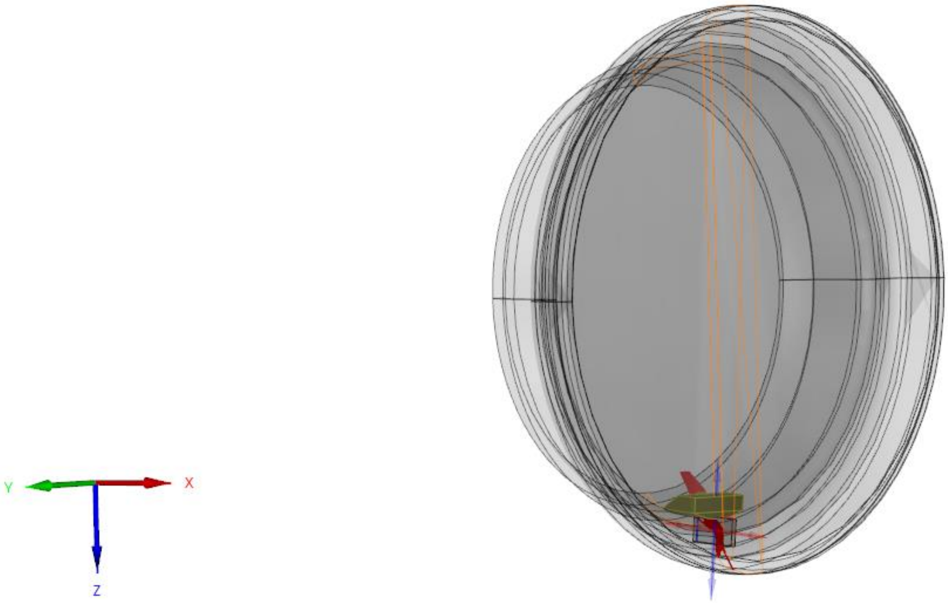

Figure 4-3 Modelling of the RNLAF inspection method in the CIVA software.

4.3.1 Specimen settings

The CAD model created in Freecad can be imported into CIVA as a specimen. In CIVA the material type need to be selected. Based on the material type the material specification is automatically obtained from the material library which is included in the CIVA software. The material specifications are shown in Table 4-1. The longitudinal and transverse wave velocities are slightly modified to match with the velocities of the physical experiment. Both the longitudinal and transverse waves are reduced by 200 m/s. The tolerances are higher than required. From the CIVA manual, the mesh size and tolerance should be smaller than the smallest detail in the CAD model [43]. However since the mesh accuracy did not influence the duration of the simulation, the tolerance and the mesh accuracy were kept at the default value of 1×10^{-6} mm.

Table 4-1 Material specification of the specimen.

Tolerance [mm]	1x10^{-6}
Material	Aluminum 1100
Density [g.cm^{-3}]	2.71
Symmetry	Isotropic
Longitudinal wave velocity [m.s^{-1}]	6300
Transverse wave velocity [m.s^{-1}]	3100
Mesh accuracy	1x10^{-6}

4.3.2 Flaw

Flaws or inclusions can be included in the specimen. CIVA gives the option to include various common flaws into the model. For the simulation of the physical experiments rectangular flaw is assumed normal to the curve radius. The flaw length and width are the values shown in section 3.1.3converted from inches to mm. The flaw is shown in Figure 4-4

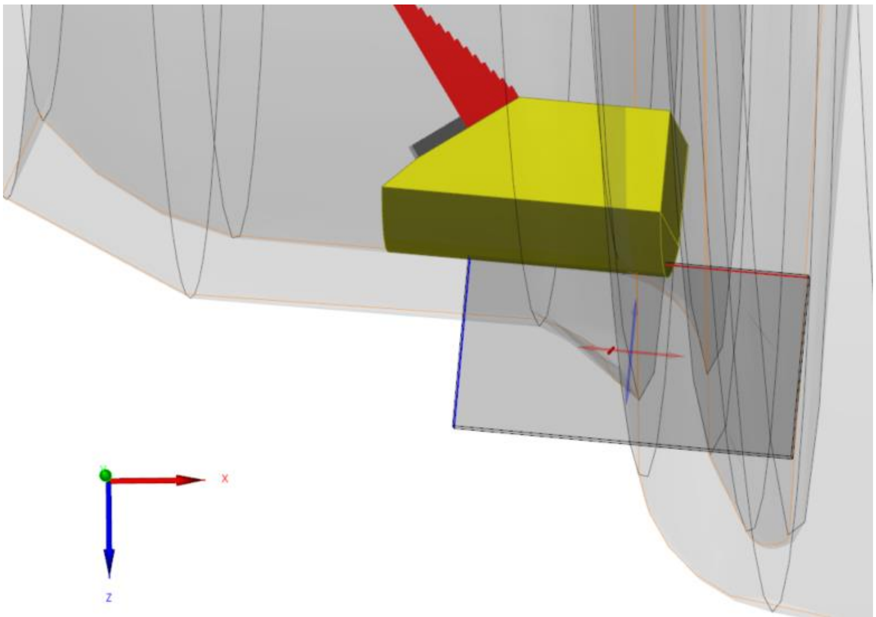

Figure 4-4 Flaw included in the specimen for the simulation.

The flaw is assumed to be rectangular. The definitions of the flaw geometry can be seen in Figure 4-5. Analysing the effect of flaw geometry and position on the signal response can be done easily by simulation experiments. Analysing the effect of flaw geometry and position on the signal response by physical experiments are limited by the available notches on the test specimen.

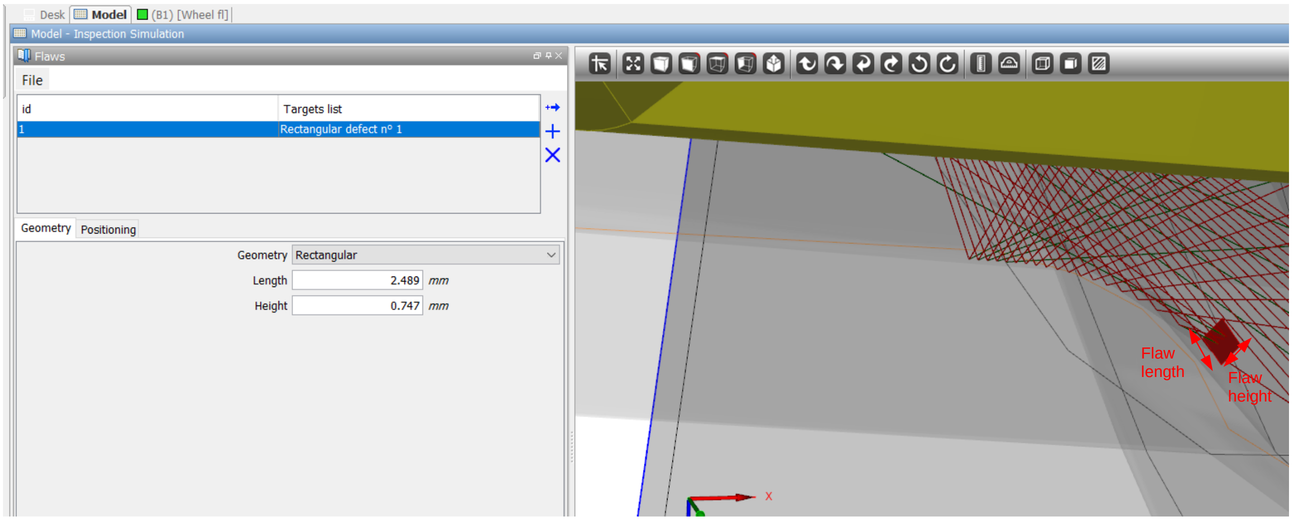

id	Targets list
1	Rectangular defect n° 1

Geometry Rectangular
Length 2.489 mm
Height 0.747 mm

Figure 4-5 Definition of the flaw geometry.

4.3.3 Probe and wedge settings

The settings of the probe are obtained from the CIVA probe library. The dimension and specification of the probe matches exactly with the probe used by the RNLAF and thus the values are unchanged. The values of the probe parameters are shown in Figure 4-6.

The wedge on the other hand is harder to obtain. Even though the SA10-N55S wedges are available in the library, the specific SA10-N55S-AID4 wedge is not present. AID4 stands for Axial Inner Diameter, which determines the curvature in the wedge. AID4 corresponds to an inner diameter between 88.9 and 101.6 mm [42]. The actual curvature of the RNLAF wedge is determined to be 101.6 mm from 3D scan. The other parameters required by CIVA are obtained from the default CIVA libraries. The parameters are shown in Figure 4-7.

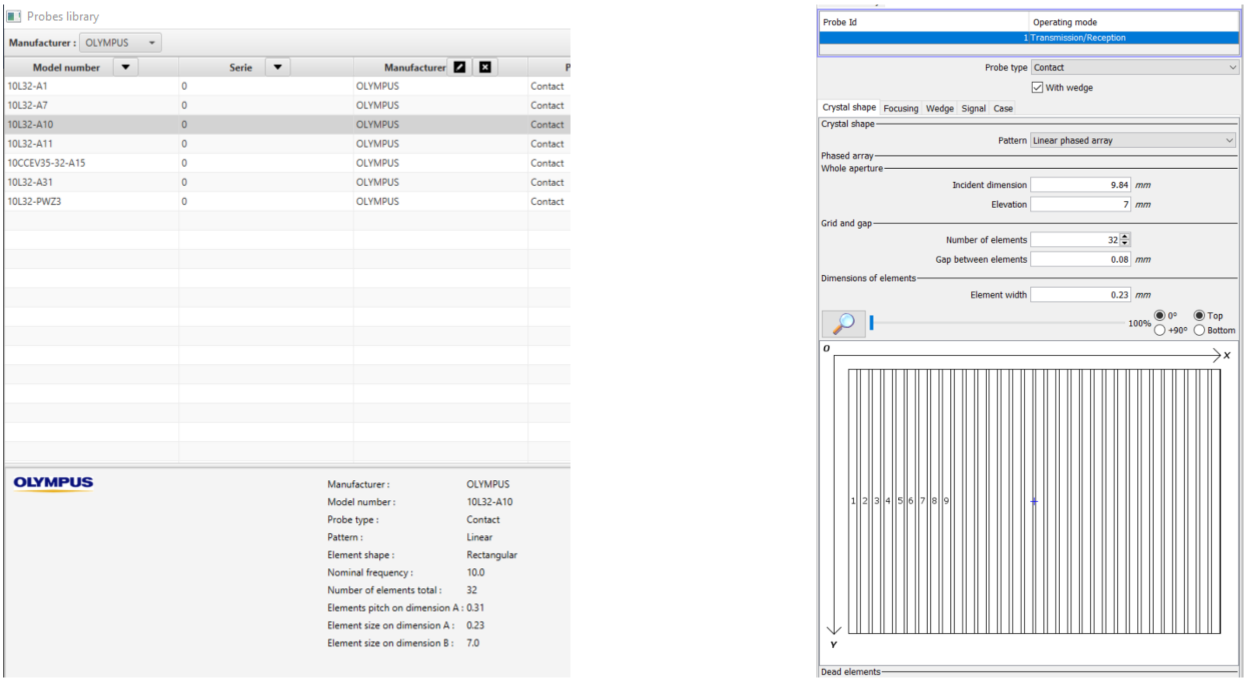

Manufacturer : OLYMPUS

Model number	Serie	Manufacturer	P
10L32-A1	0	OLYMPUS	Contact
10L32-A7	0	OLYMPUS	Contact
10L32-A10	0	OLYMPUS	Contact
10L32-A11	0	OLYMPUS	Contact
10CCEV35-32-A15	0	OLYMPUS	Contact
10L32-A31	0	OLYMPUS	Contact
10L32-PWZ3	0	OLYMPUS	Contact

Manufacturer :	OLYMPUS
Model number :	10L32-A10
Probe type :	Contact
Pattern :	Linear
Element shape :	Rectangular
Nominal frequency :	10.0
Number of elements total :	32
Elements pitch on dimension A :	0.31
Element size on dimension A :	0.23
Element size on dimension B :	7.0

Probe Id	Operating mode
1	Transmission/Reception

Probe type Contact
☑ With wedge
Pattern Linear phased array
Incident dimension 9.84 mm
Elevation 7 mm
Number of elements 32
Gap between elements 0.08 mm
Element width 0.23 mm
● 0° ○ +90°
● Top ○ Bottom

Figure 4-6 Probe settings as obtained from the library. The values are left untouched.

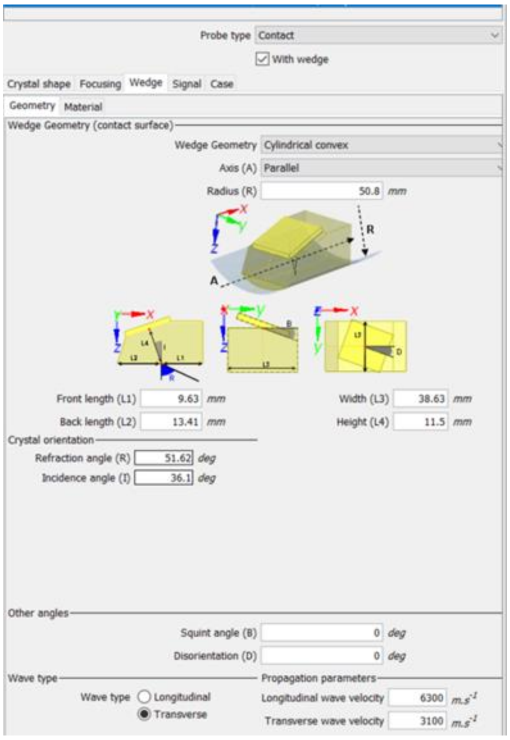

Probe type: Contact

☑ With wedge

Wedge Geometry (contact surface)

Wedge Geometry: Cylindrical convex

Axis (A): Parallel

Radius (R): 50.8 mm

Front length (L1): 9.63 mm

Back length (L2): 13.41 mm

Width (L3): 38.63 mm

Height (L4): 11.5 mm

Crystal orientation

Refraction angle (R): 51.62 deg

Incidence angle (I): 36.1 deg

Other angles

Squint angle (B): 0 deg

Disorientation (D): 0 deg

Wave type

Wave type: ○ Longitudinal ● Transverse

Propagation parameters

Longitudinal wave velocity: 6300 $m.s^{-1}$

Transverse wave velocity: 3100 $m.s^{-1}$

Figure 4-7 The parameters of the wedge required by CIVA. The dimensions are obtained from a 3D scan of the wedge used by the RNLAF.

4.4 Inspection settings

In order to simulate the physical experiments, it is required to position the wedge on the specimen in the same way as the physical experiment. Once the position of the wedge is determined, the array settings should be configured according to the settings used for the physical experiment.

4.4.1 Position wedge with respect to the specimen

The configuration and position of the wedge with respect to the specimen is shown in Figure 4-8. For the physical experiment, a guide on the wedge is present to maintain the position on the X-axis. For the CIVA model the X-position (axial position) is approximated to be at X=-41.5 mm. The positions are determined using variety study where the axial position of the wedge is varied. The axial position that comes the closes with the actual inspection was selected for the default case. For the Y-position (radial position) it is assumed that the wedge is exactly at the top of the flaw which is the at Y=0. The Z-position must be a position at which the wedge makes contact with the specimen.

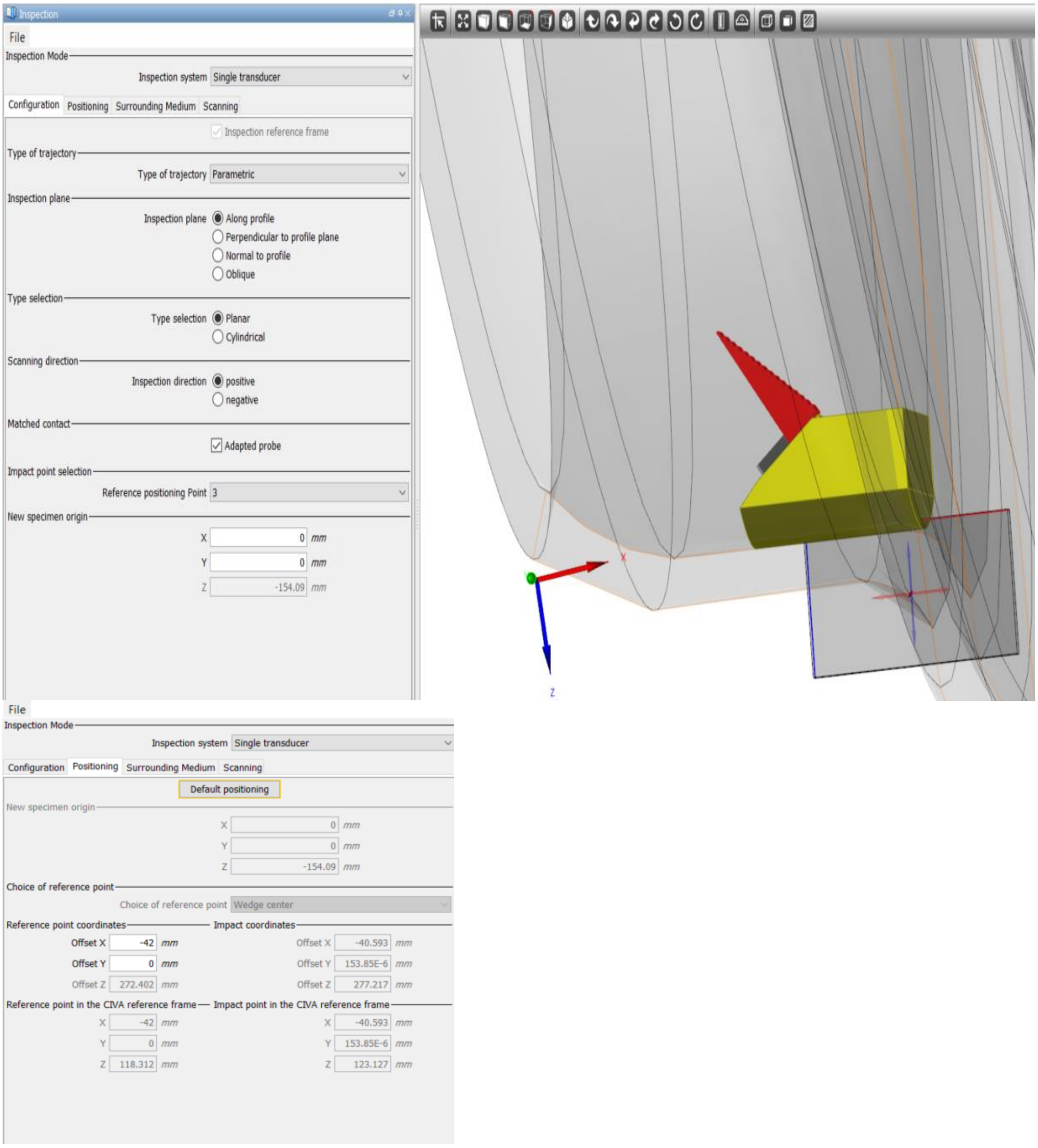

Inspection Mode

Inspection system: Single transducer

☑ Inspection reference frame

Type of trajectory: Parametric

Inspection plane: ● Along profile ○ Perpendicular to profile plane ○ Normal to profile ○ Oblique

Type selection: ● Planar ○ Cylindrical

Scanning direction

Inspection direction: ● positive ○ negative

Matched contact

☑ Adapted probe

Impact point selection

Reference positioning Point: 3

New specimen origin

X 0 mm
Y 0 mm
Z -154.09 mm

Choice of reference point: Wedge center

Reference point coordinates			Impact coordinates		
Offset X	-42	mm	Offset X	-40.593	mm
Offset Y	0	mm	Offset Y	153.85E-6	mm
Offset Z	272.402	mm	Offset Z	277.217	mm

Reference point in the CIVA reference frame			Impact point in the CIVA reference frame		
X	-42	mm	X	-40.593	mm
Y	0	mm	Y	153.85E-6	mm
Z	118.312	mm	Z	123.127	mm

Figure 4-8 Configuration and positioning of the wedge with respect to the specimen.

4.4.2 Array settings

The array settings match with the array settings from the physical experiment described in chapter 3. In all cases an aperture of 16 was chosen and sectoral scans were performed. In CIVA this results in a unisequential function at the initiation of the array settings. In the sequencing tab the elements used can be selected. The sectoral scan can be selected in the tab Transmission. There the initial angle, final angle, number of steps and step size can be selected. Furthermore one can choose the type of waves used for the inspection. The array settings are shown in Figure 4-9, Figure 4-10 and Figure 4-11.

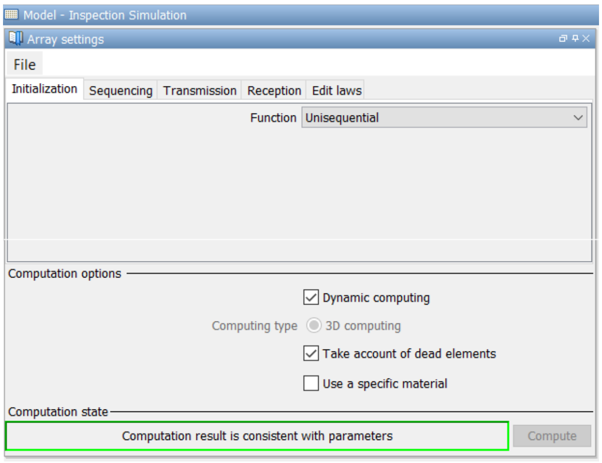

Function Unisequential

Computation options

☑ Dynamic computing

Computing type ○ 3D computing

☑ Take account of dead elements

☐ Use a specific material

Computation state

Computation result is consistent with parameters

Figure 4-9 Array settings – Initiation.

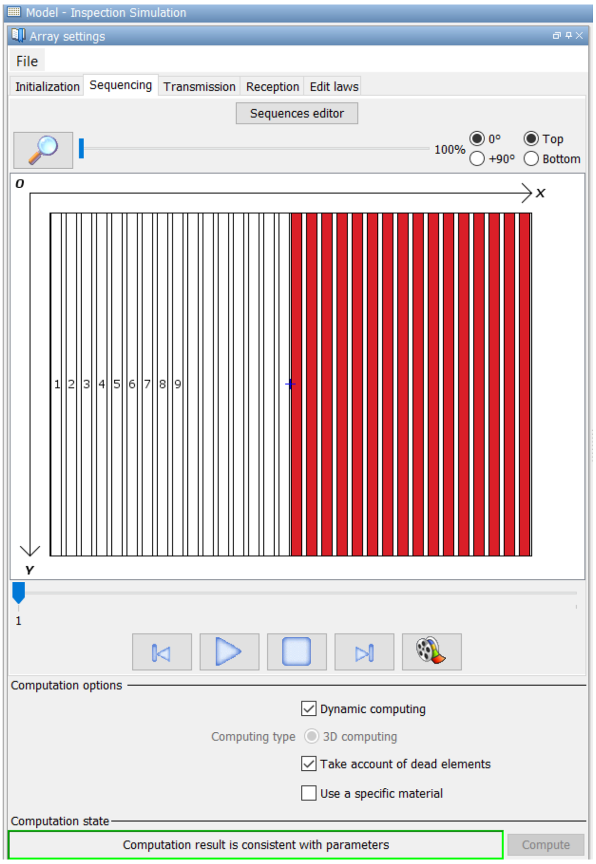

Computation options

☑ Dynamic computing

Computing type ○ 3D computing

☑ Take account of dead elements

☐ Use a specific material

Computation state

Computation result is consistent with parameters

Figure 4-10 Array settings sequencing.

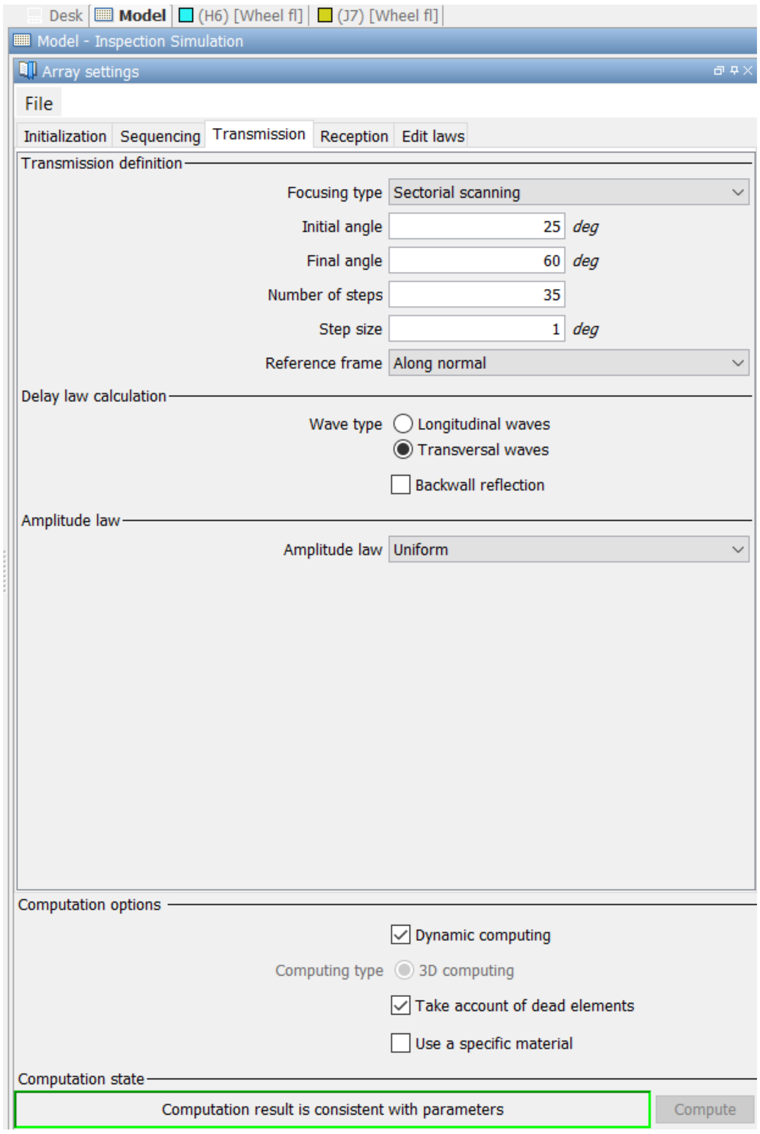

Transmission definition

Focusing type: Sectorial scanning
Initial angle: 25 deg
Final angle: 60 deg
Number of steps: 35
Step size: 1 deg
Reference frame: Along normal

Delay law calculation

Wave type: ○ Longitudinal waves
● Transversal waves
☐ Backwall reflection

Amplitude law

Amplitude law: Uniform

Computation options

☑ Dynamic computing
Computing type: ○ 3D computing
☑ Take account of dead elements
☐ Use a specific material

Computation state

Computation result is consistent with parameters

Figure 4-11 Array settings Transmission. Note that Transversal waves means S waves in CIVA.

4.5 Simulation settings

This section explains the settings for the simulation. Under the simulation panel the tabs Initialization, Interactions, Gates, Option and calibration can be found [43]. Each of these tabs will be discussed briefly.

4.5.1 Initialization

Under the tab Initialization the number of modes to be computed is to be selected. This tab is shown in Figure 4-12. The total number of modes is very dependent on [43]:

- The number of skips allowed
- The involved mode types (Longitudinal waves, Transversal waves, conversions and type of conversions)
- The part (homogeneous versus heterogeneous)
- The type of material (isotropic/anisotropic)
- The multiple interactions between a defect and the specimen surfaces

For the computation configuration as shown in Figure 4-12, the following options can be chosen for control:

- Easy settings, which cover a large majority of NDT cases according to [43]. Under this setting the selection of modes are automated and often direct and corner echoes are selected [43].
- Direct (only one reflection on the defect or the geometry)
- Half-skip (Maximum of 3 successive skips on geometry or defect)
- Full-skip (Maximum of 5 successive skips on geometry or defect)
- N skips typical L0º
- N skips typical T45º
- Double skip on defect
- Advanced definition

The possible control options are illustrated in Figure 4-13. If the advanced definition option is chosen then the user has direct access to all computation parameters, that can be found in interaction.

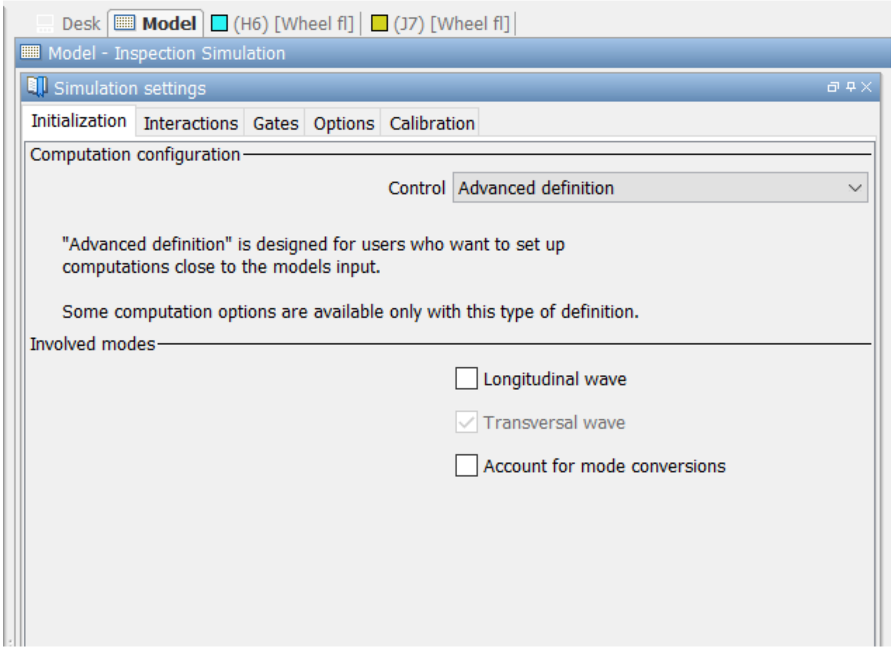

Computation configuration

Control: Advanced definition

"Advanced definition" is designed for users who want to set up computations close to the models input.

Some computation options are available only with this type of definition.

Involved modes

☐ Longitudinal wave

☑ Transversal wave

☐ Account for mode conversions

Figure 4-12 Simulation settings initialization (Advanced definition selected so Kirchhoff model can be used).

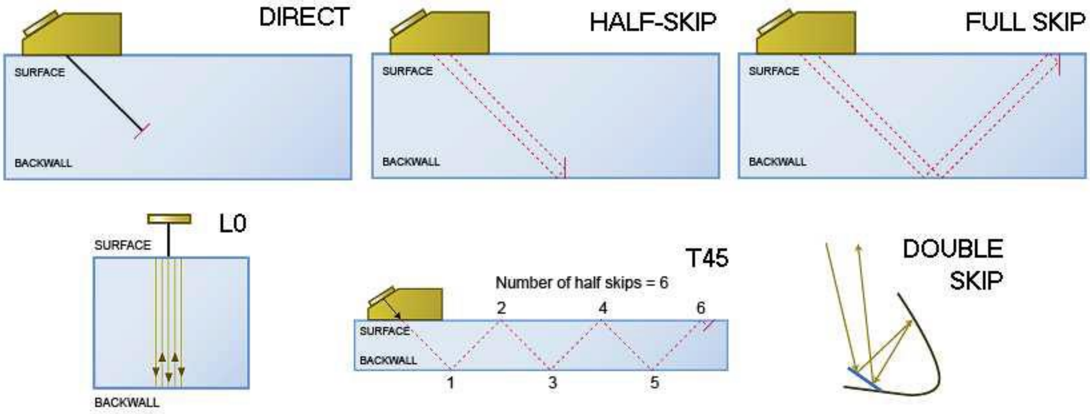

Figure 4-13 Control options computation configuration [43].

4.5.2 Interaction

The next tab is the interaction tab, which is subdivided into the tabs Specimen, flaws sensitivity zones and modes. The available options for the specimen tab are dependent on whether 3D CAD part is used as specimen or other standard parts. In case of 3D CAD parts the surfaces of the specimen considered for the beam interaction computation are not specified by a type like front, backwall, sides or interfaces, but by the positioning 3D zones. Since the testcase utilizes a 3D model for as test specimen, this case is applicable.

If advanced definition has been chosen as control for the computation configuration, then a specimen echo model shall be chosen. The options are Kirchoff or Specular. Since the specimen is a complex part consisting of a crack-liked flaw, the most suitable inspection simulation model is the Kirchhoff model [43]. The Specular model shall not be used due to the lack of the effect of diffraction on singularities [43], while the test specimen has a complex geometry. The Specular model is however more efficient if the test specimen consists of large and regular surfaces [43]. The number of half skips also needs to be chosen if advanced definition was chosen. The number of half skips can either be a maximum number or an exact number, which the user can freely select. The specimen tab for the case study is shown in Figure 4-14.

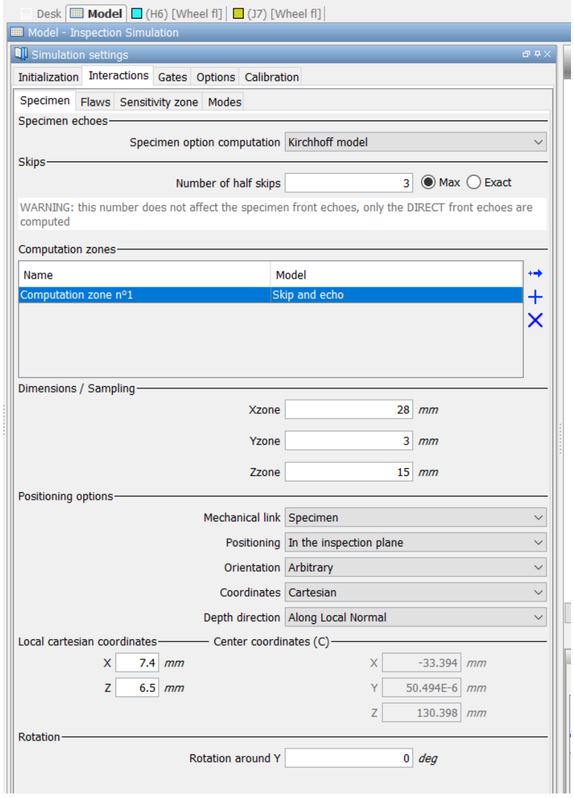

Specimen echoes

Specimen option computation: Kirchhoff model

Skips

Number of half skips: 3 ● Max ○ Exact

WARNING: this number does not affect the specimen front echoes, only the DIRECT front echoes are computed

Computation zones

Name	Model
Computation zone n°1	Skip and echo

Dimensions / Sampling

Xzone: 28 mm
Yzone: 3 mm
Zzone: 15 mm

Positioning options

Mechanical link: Specimen
Positioning: In the inspection plane
Orientation: Arbitrary
Coordinates: Cartesian
Depth direction: Along Local Normal

Local cartesian coordinates

X: 7.4 mm
Z: 6.5 mm

Center coordinates (C)

X: -33.394 mm
Y: 50.494E-6 mm
Z: 130.398 mm

Rotation

Rotation around Y: 0 deg

Figure 4-14 Simulation settings – Interaction.

The flaw tab is to enable or disable flaws for the simulation. This is useful when multiple flaws are included in the model. However for the case study there is only one flaw in the model and therefore the tab flaw does not need to be considered.

The Sensitivity zone tab has the option enable or disable the sensitivity zone. If this option is selected only some reflectors are taken into account to limit calculation time. Since the 3D model consists of curvature which causes reflections, enabling the sensitivity zone is not an option.

Finally the mode tab contains a list of all the selected modes. Under this tabs no settings can be changed as the number of modes are defined by the choices made in the previous tabs. The mode tab is shown in Figure 4-15.

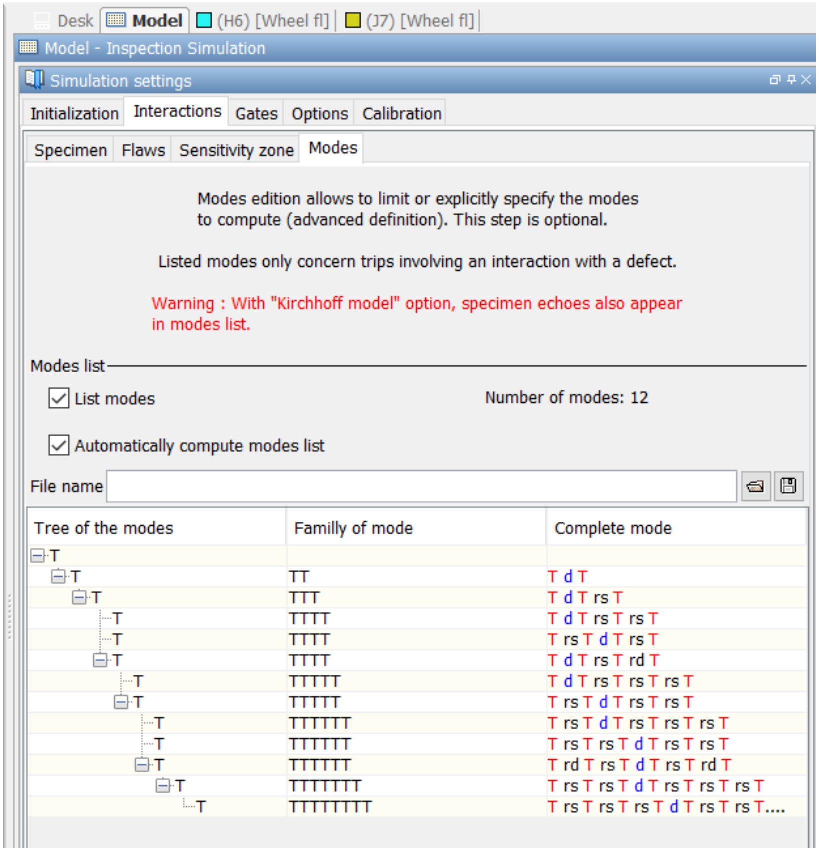

Modes edition allows to limit or explicitly specify the modes to compute (advanced definition). This step is optional.

Listed modes only concern trips involving an interaction with a defect.

Warning : With "Kirchhoff model" option, specimen echoes also appear in modes list.

Modes list

☑ List modes

Number of modes: 12

☑ Automatically compute modes list

File name

Tree of the modes	Familly of mode	Complete mode
T		
T	TT	T d T
T	TTT	T d T rs T
T	TTTT	T d T rs T rs T
T	TTTT	T rs T d T rs T
T	TTTT	T d T rs T rd T
T	TTTTT	T d T rs T rs T rs T
T	TTTTT	T rs T d T rs T rs T
T	TTTTTT	T rs T d T rs T rs T rs T
T	TTTTTT	T rs T rs T d T rs T rs T
T	TTTTTT	T rd T rs T d T rs T rd T
T	TTTTTTT	T rs T rs T d T rs T rs T rs T
T	TTTTTTTT	T rs T rs T rs T d T rs T rs T....

Figure 4-15 Simulation settings - Number of modes (the higher the number of modes, the higher the computation time).

4.5.3 Gates

Under the tab Gates the user can define simulation gates to [43]:

- Explicitely specify the time gate in which the signals have to be recorded
- Synchronize a gate with respect to others
- Specify the storage type in each gate (summed signals, channels signals or summed+channels)

It is also possible to select "Auto" so that the full signals are recorded. For this case study Auto is selected so that the gate is automatically selected by the software.

4.5.4 Options

Under the tab Options the computation options can be defined, which is shown in Figure 4-17. The first option is to select the computation mode, which can either be 2D or 3D. The CIVA user manual recommends to use 3D computation as 2D option is meant for a fast computation which can be used as first approach. To perform a fast computation the field and the flaw interaction are computed in 2D, meaning that the transducer is approximated as a 2D-extruded transducer and that the beam defect interaction is computed only on a line at the intersection of the incidence plane and the defect surface [43]. This is shown in Figure 4-16. Therefore 3D computation will be chosen for the inspection simulations.

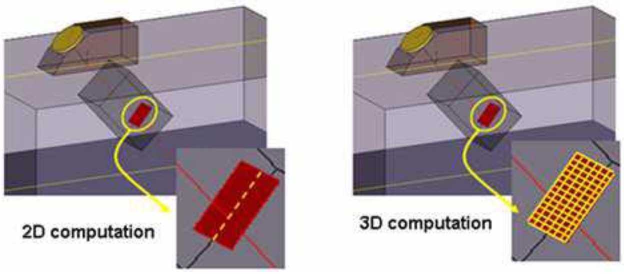

Figure 4-16 Difference between 2D and 3D computation [43].

Next the field/reflector interaction needs to be chosen. Plane wave approximation for incident beam is fast but less precise, especially at the near field. Full incident beam takes more time, but is more precise.

Then the field and defect accuracy needs to be determined. These parameters allow increasing the level of accuracy of the computation. The option field refines the mesh on which the ultrasonic field is computed and hence improves results for configurations with rapidly varying field around the interactions area. The option defect refines the mesh of the flaw on which the beam-defect interaction is computed. Increasing the defect precision can be relevant for small or irregular flaws [43].

To find the required accuracy a variation study was performed to check for convergence. During the variation study the field and defect accuracies are increased with 1 every time. If the accuracy n+1 shows no significant different with respect to accuracy n, then accuracy n shall be chosen as simulations with accuracy n is faster than with accuracy n+1. The settings under options for the case study are summarised in Figure 4-17.

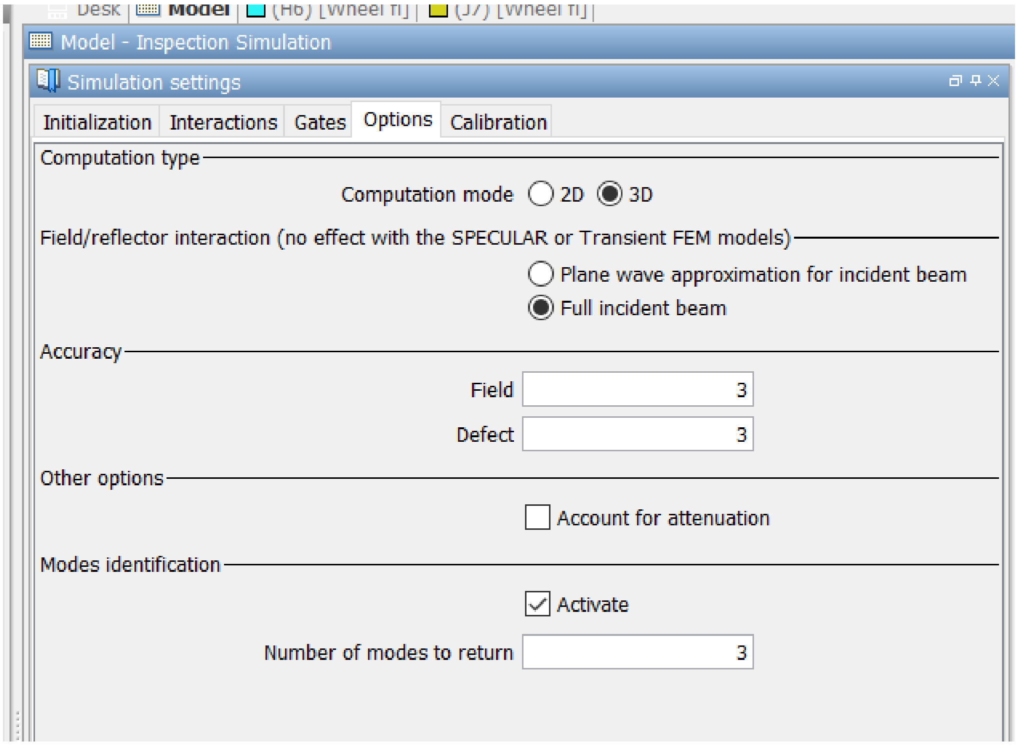

Computation type

Computation mode ○ 2D ● 3D

Field/reflector interaction (no effect with the SPECULAR or Transient FEM models)

○ Plane wave approximation for incident beam
● Full incident beam

Accuracy

Field 3
Defect 3

Other options

☐ Account for attenuation

Modes identification

☑ Activate

Number of modes to return 3

Figure 4-17 Simulation settings – options.

The simulation settings are kept constant for the different simulated cases. Same goes for the simulation of the empirical data for the POD analysis.

4.5.5 Calibration

Under the calibration tab calibration can be performed for the simulation. If no calibration is applied, the simulated result and signal amplitudes are reported in arbitrary units called CIVA points. In this case the maximum signal amplitude is where the most pts are assigned and becomes the reference value of 0 dB or

100% FSH. It is also possible to import a single reference, so that a number of pts can be assigned to the reference value of 0 dB or 100% FSH.

4.6 Default case

In order to keep the cases comparable with the physical experiments the default case was selected as starting point. Case 5 from Table 3-5 is selected as the default case as it uses the default settings used by the RNLAF. First the array settings are used to make sure it matches the array settings of case 5. Then a simulation was run uncalibrated, so that the strongest signal response is 0 dB or 100% FSH. The number of CIVA points corresponding to 100% or 0 dB is then determined. However the default cause was calibrated in such a way that the signal strength was 74.51% at the flaw location, which is also the highest signal return within the sectoral scan. Since the number of CIVA points for 100% is known, the number of CIVA points for 74.51% can be calculated. This number of CIVA point can then be imported as a single reference for under the calibration tab. The signal strength of case 5 in the simulation shall then be identical to the case 5 from the physical experiments.

4.7 Results

This section shows the results of the simulated cases in the same way as in section 3.4 for the physical experiments. The results are shown in Table 4-2, Table 4-3 and Table 4-4.

Table 4-2 Simulated test cases 1 to 11 using an aperture size of 16 elements, using element numbers 16 to 32.

Test nr	Wedge position [mm]	Signal strength [%]	Shot angle [deg]	Sound path [mm]	TOF [µs]
1	Guide -4 mm	59.949	51	10.243	6.61
2	Guide -3 mm	60.321	48	9.859	6.36
3	Guide -2 mm	63.782	45	9.558	6.16
4	Guide -1 mm	71.381	43	9.09	5.86
5	Guide	74.51	40	8.748	5.65
6	Guide +1 mm	71.304	38	8.32	5.37
7	Guide +2 mm	65.92	35	8.019	5.17
8	Guide +3 mm	50.545	33	7.645	4.93
9	Guide +4 mm	30.778	29	7.577	4.89
10	Guide +5 mm	15.1	27	7.241	4.67
11	Guide +6 mm	12.382	25	6.935	4.48

Table 4-3 Simulated test cases 1 to 11 using an aperture size of 16 elements, using element numbers 8 to 23.

Test nr	Wedge position [mm]	Signal strength [%]	Shot angle [deg]	Sound path [mm]	TOF [µs]
12	Guide -4 mm	40.899	57	12.279	7.92
13	Guide -3 mm	47.819	56	11.559	7.45
14	Guide -2 mm	51.9	54	11.044	7.12
15	Guide -1 mm	55.866	51	10.573	6.82
16	Guide	59.245	49	10.013	6.46
17	Guide +1 mm	58.354	46	9.658	6.24
18	Guide +2 mm	66.054	43	9.241	5.96
19	Guide +3 mm	69.81	41	8.752	5.64
20	Guide +4 mm	69.494	38	8.378	5.41
21	Guide +5 mm	64.521	35	8.033	5.18
22	Guide +6 mm	49.833	33	7.633	4.92

Table 4-4 Simulated test cases 23 to 33 of using an aperture size 16 elements, using element numbers 1 to 16.

Test nr	Wedge position [mm]	Signal strength [%]	Shot angle [deg]	Sound path [mm]	TOF [µs]
23	Guide -4 mm	13.51	60	14.384	9.28
24	Guide -3 mm	26.59	60	13.516	8.72
25	Guide -2 mm	34.522	59	12.75	8.22
26	Guide -1 mm	42.867	57	12.097	7.8
27	Guide	47.6	55	11.459	7.39
28	Guide +1 mm	52.525	53	10.91	7.04
29	Guide +2 mm	55.54	51	10.308	6.65
30	Guide +3 mm	56.078	48	9.817	6.34
31	Guide +4 mm	58.093	45	9.427	6.09
32	Guide +5 mm	64.922	42	8.982	5.79
33	Guide +6 mm	66.85	39	8.56	5.52

The simulated results and physical results will be compared in chapter 5.

5 Comparison between experimental and simulated results

This chapter analyses the results obtained from chapter 3 and chapter 4, so that the accuracy of the model can be estimated. The comparison of signal strengths, shot angle, amplitude and time of flights are made. The comparison of signal strength compares the signal return at the flaw location. While the angle of intersection, sound path and time of flight gives an indication of the flaw location. Based these parameters the accuracy of the model can be determined. In some cases the flaw cannot be detected from physical experiment. In that case the signal return is set to 0%. For shot angle, sound path and TOF the value Not a number (NAN) is inserted if no values can be obtained.

5.1 Comparison in signal strengths

The signal strengths of the simulated results and the experimental results have been put in a graph comparison. The results of test cases 1 to 11 are shown in Figure 5-1 with an aperture size of 16 elements, using elements 17 to 32. For this array settings it can be seen that at the data points are the most accurate when the lateral position of the wedge is near 0 (default guide position). The farther away the more deviation can be seen.

Results from test cases 12 to 22 with aperture size 16, using elements 8 to 23 are shown in Figure 5-2. It can be seen that with this array setting the simulated results and the physical experiment results show more deviation. It is noticeable that at guide position -1 the simulated result and the experimental result are not in agreement. The results at guide position 0 and guide position -2 are however quite in agreement with each other. The most likely explanation that a measurement error was made when performing the physical experiment at guide position -1.

Results from test cases 23 to 33 with aperture size 16, using elements 1 to 16 are shown in Figure 5-3. From the three array settings, this setting shows the worst accuracy. Data points at the lateral position wedge -4 to -1 are empty as no results could be obtained from this section. Unlike test cases 1 to 11 the simulated results are actually more in agreement with the experimental results when the guide is position farther away from the default position in the positive direction.

The A scans of the 33 test cases can be found in Appendix A.

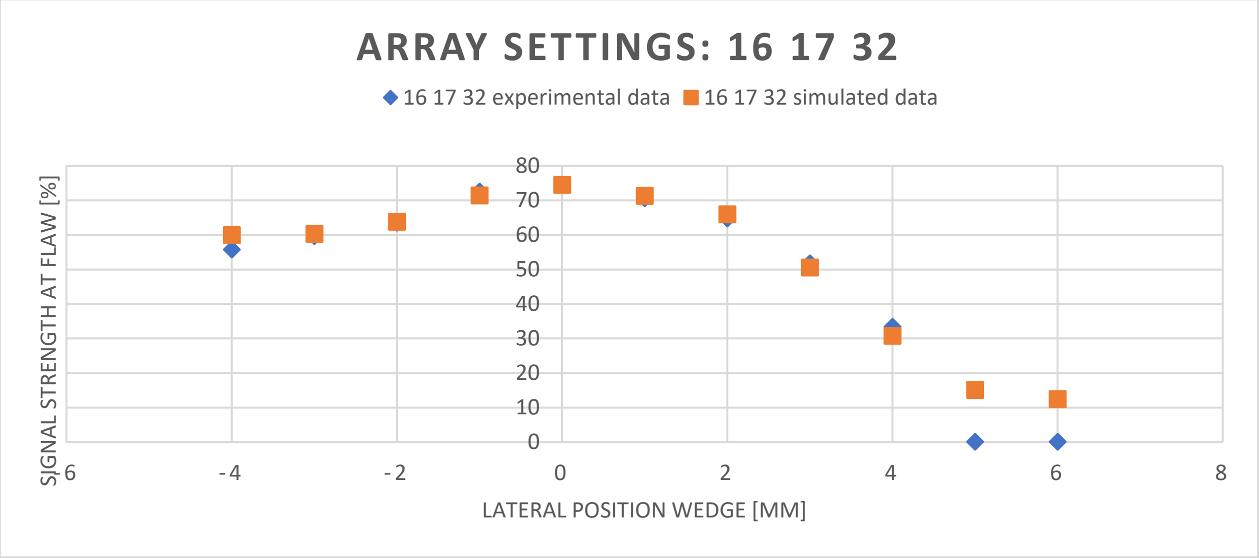

Figure 5-1 Comparison results from cases 1 to 11. Note that the dots on lateral position 5 and 6 are NAN for the physical experiment, because results could not be obtained.

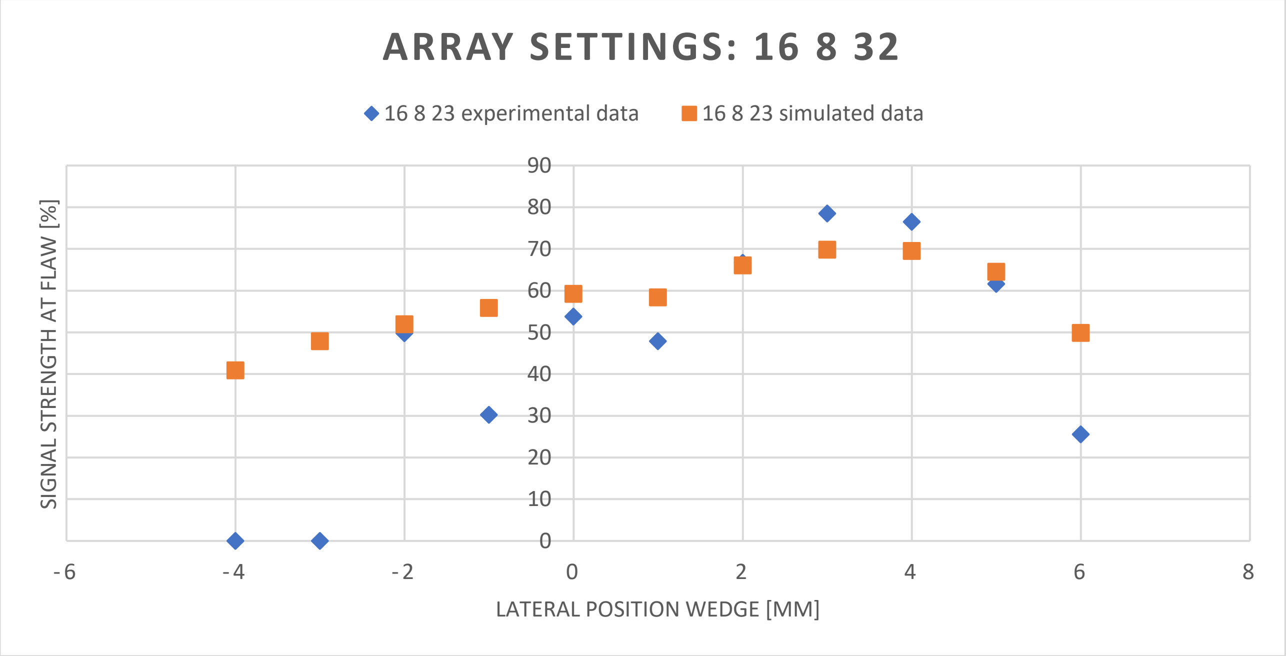

Figure 5-2 Comparison results from cases 12 to 22. Note that the dots on lateral position -4 and -3 are NAN for the physical experiment, because results could not be obtained.

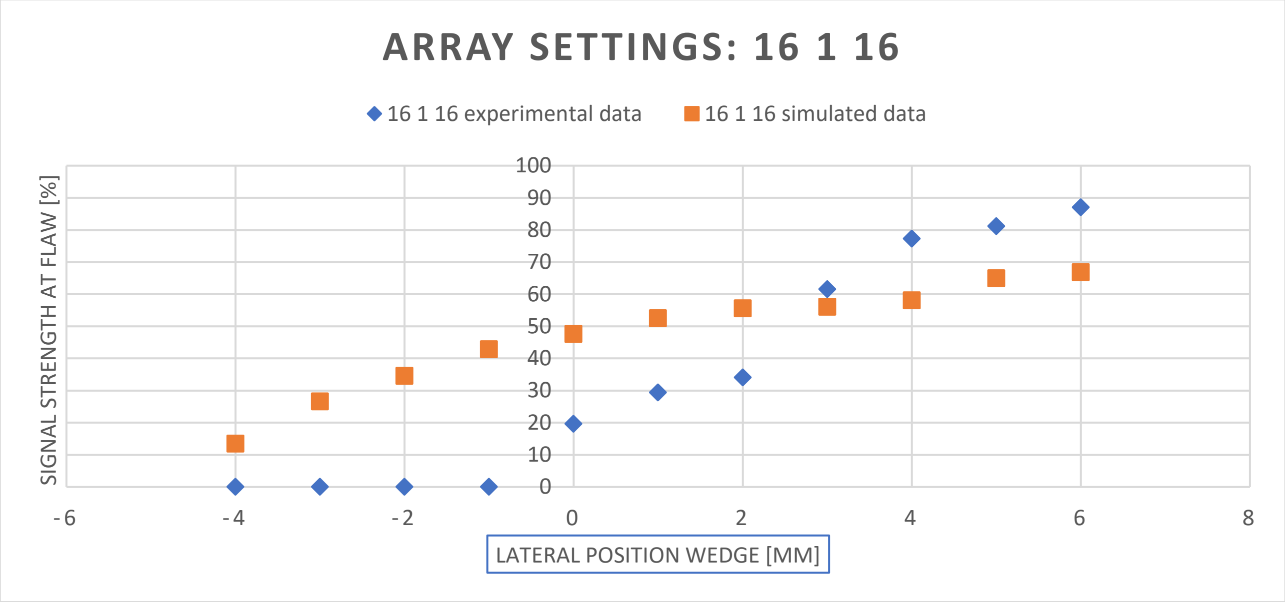

Figure 5-3 Comparison results from cases 23 to 33. Note that the dots on lateral position -4 to -1 are NAN for the physical experiment, because results could not be obtained.

5.2 Comparison in shot angle

This section compares the shot angle of the test cases. The shot angle is determined from the angle where the signal return is the highest, both for the experimental and the simulated results. The shot angle should be between 25 and 60 degrees as this was set in both the Olympus flaw detector and the model.

The results of the shot angles are shown in Table 5-1 to Table 5-3. The tables show the value of the shot angles both from physical experiments and from simulations. Furthermore the difference between the value of the shot angles from the physical experiment and the experiment is shown as a percentage.

Table 5-1 Results comparison between shot angles using an aperture of 16, consisting of elements 17 to 32.

Test nr	Wedge position [mm]	Shot angle experimental [deg]	Shot angle simulation[deg]	Difference in shot angle [%]
1	Guide -4 mm	47	51	7.8
2	Guide -3 mm	47	48	2.0
3	Guide -2 mm	44	45	2.2
4	Guide -1 mm	42	43	2.3
5	Guide	39	40	2.5
6	Guide +1 mm	39	38	2.6
7	Guide +2 mm	33	35	5.7
8	Guide +3 mm	31	33	6.0
9	Guide +4 mm	29	29	0
10	Guide +5 mm	NAN	27	NAN
11	Guide +6 mm	NAN	25	NAN

Table 5-2 Results comparison between shot angles using an aperture of 16, consisting of elements 8 to 23.

Test nr	Wedge position [mm]	Shot angle experimental [deg]	Shot angle simulation [deg]	Difference in shot angle [%]
12	Guide -4 mm	NAN	57	
13	Guide -3 mm	NAN	56	
14	Guide -2 mm	53	54	1.9
15	Guide -1 mm	47	51	7.8
16	Guide	48	49	2.0
17	Guide +1 mm	44	46	4.4
18	Guide +2 mm	41	43	4.7
19	Guide +3 mm	38	41	7.3
20	Guide +4 mm	34	38	10.5
21	Guide +5 mm	35	35	0
22	Guide +6 mm	29	33	12.1

Table 5-3 Results comparison between shot angles using an aperture of 16, consisting of elements 1 to 16.

Test nr	Wedge position [mm]	Shot angle experimental [deg]	Shot angle simulation[deg]	Difference in shot angle [%]
23	Guide -4 mm	NAN	60	NAN
24	Guide -3 mm	NAN	60	NAN
25	Guide -2 mm	NAN	59	NAN
26	Guide -1 mm	NAN	57	NAN
27	Guide	53	55	3.6
28	Guide +1 mm	49	53	7.6
29	Guide +2 mm	47	51	7.8
30	Guide +3 mm	43	48	10.4
31	Guide +4 mm	42	45	6.7
32	Guide +5 mm	40	42	4.8
33	Guide +6 mm	37	39	5.1

5.3 Comparison in sound path lengths

This section compares the results in sound path lengths. The sound path is defined as a line from where the sound enters the material to when the sound reaches the flaw and thus shows the highest amplitude. The sound path obtained from experiments results and from simulated results can be visualized in Figure 5-4.

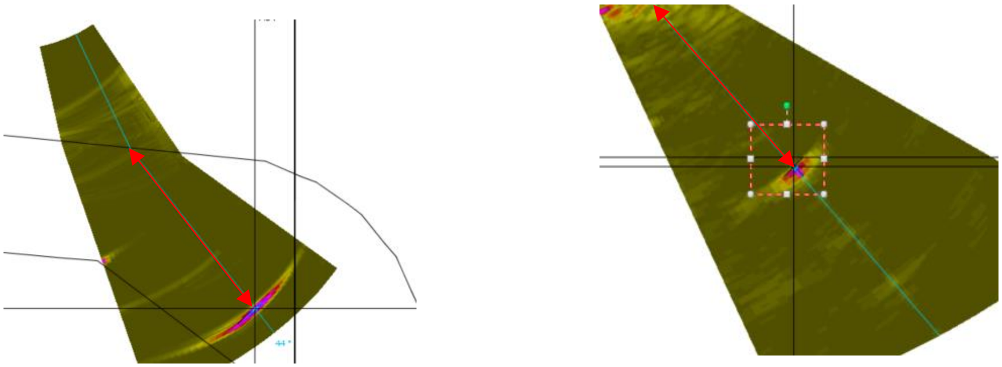

(a) (b)

Figure 5-4 Visualization of the sound path from a simulation result (a) and an experimental result (b).

While the result obtained from experiment immediately shows the true sound path, the sound path of the simulated result goes from the transducer all the way to the flaw. Thus the total sound path of the simulated case is the sound path through the wedge plus the sound path from entering the material to the flaw. To make a comparison of sound paths, the sound path through the wedge is subtracted from the result for the simulated case.

The results of sound paths are shown from Table 5-4 to Table 5-6. The tables show the value of the sound paths both from physical experiments and from simulations. Furthermore the difference between the value of the sound path lengths from the physical experiment and the experiment is shown in percentage.

Table 5-4 Results comparison between sound paths using an aperture of 16, consisting of elements 17 to 32.

Test nr	**Wedge position [mm]**	**Sound path experimental [mm]**	**Sound path simulation [mm]**	**Difference in sound path [%]**
1	Guide -4 mm	9.579	10.243	6.5
2	Guide -3 mm	9.579	9.859	2.8
3	Guide -2 mm	9.486	9.558	0.8
4	Guide -1 mm	9.3	9.09	2.3
5	Guide	9.3	8.748	6.3
6	Guide +1 mm	9.393	8.32	12.9
7	Guide +2 mm	8.51	8.019	6.1
8	Guide +3 mm	8.417	7.645	10.1
9	Guide +4 mm	8.417	7.577	11.1
10	Guide +5 mm	NAN	7.241	NAN
11	Guide +6 mm	NAN	6.935	NAN

Table 5-5 Results comparison between sound paths using an aperture of 16, consisting of elements 8 to 23.

Test nr	Wedge position [mm]	Sound path length experimental [mm]	Sound path length simulation [mm]	Difference in sound path length [%]
12	Guide -4 mm	NAN	12.279	NAN
13	Guide -3 mm	NAN	11.559	NAN
14	Guide -2 mm	10.416	11.044	5.7
15	Guide -1 mm	10.835	10.573	2.5
16	Guide	10.277	10.013	2.6
17	Guide +1 mm	9.998	9.658	3.5
18	Guide +2 mm	9.579	9.241	3.7
19	Guide +3 mm	8.928	8.752	2.0
20	Guide +4 mm	8.835	8.378	5.5
21	Guide +5 mm	8.556	8.033	6.5
22	Guide +6 mm	8.463	7.633	10.9

Table 5-6 Results comparison between sound paths using an aperture of 16, consisting of elements 1 to 16.

Test nr	Wedge position [mm]	Sound path experimental [mm]	Sound path simulation [mm]	Difference in sound path [%]
23	Guide -4 mm	NAN	14.384	NAN
24	Guide -3 mm	NAN	13.516	NAN
25	Guide -2 mm	NAN	12.75	NAN
26	Guide -1 mm	NAN	12.097	NAN
27	Guide	12.043	11.459	5.1
28	Guide +1 mm	11.718	10.91	7.4
29	Guide +2 mm	11.068	10.308	7.4
30	Guide +3 mm	10.23	9.817	4.2
31	Guide +4 mm	9.626	9.427	2.1
32	Guide +5 mm	9.021	8.982	0.4
33	Guide +6 mm	8.51	8.56	0.6

5.4 Comparison in Time of Flight (TOF)

This section discusses the comparison in TOF. The TOF is the time requires for the soundwave to travel from entering the material to the flaw. The TOF is directly related to the sound path which was compared in section 5.3. Same as with the sound path length the TOF is only considered from the moment the soundwave enters the material till the sound wave reaches the flaw location.

The results of the TOF are shown in Table 5-7 to Table 5-9. The tables show the value of the TOFs both from physical experiments and from simulations. Furthermore the difference between the value of the TOFs from the physical experiment and the experiment is shown in percentage.

Table 5-7 Results comparison between TOF using an aperture of 16, consisting of elements 17 to 32.

Test nr	Wedge position [mm]	TOF experimental [µs]	TOF simulation [µs]	Difference in TOF [%]
1	Guide -4 mm	6.18	6.61	6.5
2	Guide -3 mm	6.18	6.36	2.8
3	Guide -2 mm	6.12	6.16	0.7
4	Guide -1 mm	6	5.86	2.40
5	Guide	6	5.65	6.2
6	Guide +1 mm	6.06	5.37	12.9
7	Guide +2 mm	5.49	5.17	6.2
8	Guide +3 mm	5.43	4.93	10.1
9	Guide +4 mm	5.43	4.89	11.0
10	Guide +5 mm	NAN	4.67	NAN
11	Guide +6 mm	NAN	4.48	NAN

Table 5-8 Results comparison between TOF using an aperture of 16, consisting of elements 8 to 23.

Test nr	Wedge position [mm]	TOF experimental [µs]	TOF simulation [µs]	Difference in TOF [%]
12	Guide -4 mm	NAN	7.92	NAN
13	Guide -3 mm	NAN	7.45	NAN
14	Guide -2 mm	6.72	7.12	5.6
15	Guide -1 mm	6.99	6.82	2.5
16	Guide	6.63	6.46	2.6
17	Guide +1 mm	6.45	6.24	3.4
18	Guide +2 mm	6.18	5.96	3.7
19	Guide +3 mm	5.76	5.64	2.1
20	Guide +4 mm	5.7	5.41	5.4
21	Guide +5 mm	5.52	5.18	6.6
22	Guide +6 mm	5.46	4.92	11.0

Table 5-9 Results comparison between TOF using an aperture of 16, consisting of elements 1 to 16.

Test nr	Wedge position [mm]	TOF experimental [μs]	TOF simulation [μs]	Difference in TOF [%]
23	Guide -4 mm	NAN	9.28	NAN
24	Guide -3 mm	NAN	8.72	NAN
25	Guide -2 mm	NAN	8.22	NAN
26	Guide -1 mm	NAN	7.8	NAN
27	Guide	7.77	7.39	5.1
28	Guide +1 mm	7.56	7.04	7.4
29	Guide +2 mm	7.14	6.65	7.4
30	Guide +3 mm	6.6	6.34	4.1
31	Guide +4 mm	6.21	6.09	2.0
32	Guide +5 mm	5.82	5.79	0.5
33	Guide +6 mm	5.49	5.52	0.5

5.5 Results discussion and conclusion

Several physical experiments were performed and the experiments were replicated using a model in which the conditions performed during the experiment were set to be as equal as possible and results compared. In this section the results are discussed. For each array settings the maximum deviation and the average deviation among the test cases are given.

5.5.1 Signal strength

Comparing the signal strengths of the different cases in section 5.1 it can be seen that the accuracy is dependent on the array settings. When the elements 17 to 32 are used one can observe that the simulated results match quite well with the physical experiment results. This is especially true for the case when the signal strength is high. When the signal strength at the flaw is low, the signal gets lost in noise for the experimental case. However this is not the case for the simulated results. This is due to the fact that noise was not included in the model. In CIVA it is possible to include noise. However due to time limitation it was not possible to include noise in the model.

In the cases when elements 8 to 23 are used it can be seen that the results of simulations and physical experiments do not match as well as when elements 17 to 32 are used. However the results are the worst when elements 1 to 16 are used. The S scans of the test cases can be visualized in details in Appendix A.

The maximum deviation in signal strength between simulations and physical experiments among the test cases when elements 17 to 32 are used is 8.3% while the average deviation is 2.65%. For the test cases when elements 8 to 23 are used the maximum deviation is 48.85% and the average deviation is 17.12 %. For the test cases when elements 1 to 16 are used the maximum deviation is 58.8% and the average deviation is 34.21%.

The result shows that the accuracy varies among the elements used and the guide positions. This is not surprising as switching elements has a similar effect to changing the guide position.

From this analysis it can be concluded that the model is the mostly in agreement with the experiments when elements 17 to 32 of the transducer are used and the guide is close to its original position. Accuracy drops sharply when other elements are being used and when the guide is farther away from its neutral position.

5.5.2 Shot angles

In section 5.2 a comparison was made between the shot angles of the results obtained from physical experiments and simulations. Comparing the shot angles determines the accuracy of the flaw location. Deviation in shot angles between simulation and physical experiment results are caused by either discrepancy in the position of the wedge or the position of the flaw.

The maximum deviation in shot angle for the test cases where elements 17 to 32 of the transducer are used is 7.84% while the average deviation is 3.5%. For the test cases where elements 8 to 23 of the transducer are used the maximum deviation is 12.12% while the average deviation is 5.63%. For the test cases where elements 1 to 16 of the transducer are used the maximum deviation is 10.42% while the average deviation is 6.57%. The deviation in percentage does however not show the entire picture. Comparing test nr 15 with 20 it can be seen the differences in shot angle in percentage are not the same while in absolute value the difference in angle is 4 degrees. This is because the shot angles in test nr 20 are have lower values. Looking at the absolute values the minimum difference is 0 degrees and the maximum difference is 5 degrees. While for signal strength the deviation varies significantly among the elements used during inspection this is not the case for the shot angles as the deviations are rather consistent among the test cases.

Looking at the shot angles it can be observed that for the test cases where no experimental results can be obtained, the shot angles from the corresponding simulating provides a shot angle either near 25 degrees or near 60 degrees. Recalling that the beam angle of the sectoral scan is between 25 and 60 degrees, a possible explanation is that for the experimental result the flaw falls outside the beam angle and therefore cannot be detected. The other explanation is that the signal strength at the flaw is lost due to noise.

5.5.3 Sound path lengths and TOFs

Sound path lengths and TOFs are related to each other as the speed of sound wave going through the material is 3100 m/s for transverse wave. This velocity was both defined in the model and in the Olympus flaw detector. Same as the shot angle the sound path length and the TOF provides an accuracy of the wedge position and the flaw location. The maximum deviation of sound path lengths for test cases when elements 17 to 32 are used is 12.90% and the average deviation is 6.54%. When elements 8 to 23 are used the maximum deviation is 10.87% and the average deviation is 4.76%. When elements 1 to 16 are used the maximum deviation is 7.41% and the average deviation is 3.89%. Looking at the TOF when elements 17 to 32 are used, the maximum deviation is 12.85% and the average deviation is 6.53%. When elements 8 to 23 are used the maximum deviation in TOF is 10.96% and the average deviation is 4.76%. When elements 1 to 16 are used the maximum deviation in TOF is 7.39% and the average deviation is 3.86%.

For the sound path lengths and TOF it appears that there is a range in deviations among the test cases. However same as with the shot angles it is useful to look at the absolute differences. Since the sound path length and TOF values are small a slight variation can cause rather high percentages. Looking at the absolute deviations, the maximum absolute deviation is test case nr 6, which is 1.07 mm. The values of the absolute deviations of all the other cases are well below 1 mm.

The largest absolute TOF deviation is also test case nr 6 which is 0.69 µs. This is expected since the TOF is proportional to the sound path length as the TOF is the time, the sound path length is a distance and the velocity of the sound wave in aluminium is constant.

5.5.4 Overall conclusion

Comparing the results of the test cases obtained from physical experiments and simulations it can be seen that when it comes to the signal strength at the flaw location, the results are most accurate when elements 17 to 32 of the transducer are used. The discrepancies between signal strengths from simulations and physical experiments are significant when elements 8 to 23 or elements 1 to 16 or the transducers are used. Analysing the signal strength at the flaw location the range of which the model provides sufficient accuracy was determined.

Since noise was not modelled, the simulated results usually give an overestimated signal strength at the flaw. This is especially prominent when the signal strength is low (below 60%). That also explains why in cases when no results can be obtained from physical experiments, the model does provide results.

The discrepancy in shot angles, sound path lengths and TOFs gives an indication of the deviation in flaw location. The deviations are rather consistent along the test cases. Maximum deviations in shot angles, sound path lengths and TOFs do not exceed 13%. In absolute values the maximum deviation of sound path length is 1.07 mm and the maximum deviation of TOF is 0.69 µs. Based on these values it is determined that the flaw location is modelled sufficiently accurately and the positioning of the wedge on the test specimen in the model matches quite accurately with reality. Other possible causes of discrepancies are:

- Presence of a wobble (partly corrected, but not fully eliminated)
- Uncertainty of the wedge placements when performing the physical inspection as distances were determined by using layers of papers
- Less contact between wedge and test specimen when the guide position deviates from its default position (see Figure 3-7 (a))

Based on the analysis the model is accurate enough to provide data for a POD analysis. The condition is that the default settings shall be used which corresponds to test case 5 from Table 3-5.

6 MAPOD analysis

This chapter analyses the probability of detection (POD) of the method the RNLAF used to inspect their wheel rims. In order to perform a POD analysis inspection results from a large sample sets is required. The RNLAF requires in their procedure to remove the wheel rim for further inspection when the PA inspection gives a signal strength of 40%. From this definition a signal strength of ≥ 40% is considered as a hit, while anything below 40% is considered a miss.

Thus in this case the hit/miss approach will be used for the MAPOD analysis. For the hit/miss approach a minimum of 60 flaws is recommended [33]. In NDE the reliability is often given with a crack size with a POD of 90% within a confidence bound of 95%, which is often noted as $a_{90/95}$ [12].

In chapter 5 the accuracy of the model is analysed. For the default settings described by the RNLAF the model provides sufficiently accurate results. Therefore the model can be used to generate inspection results to perform a POD calculation.

6.1 Sample sets

To perform the POD analysis a samples set is generated by including three variables: the crack length, crack height and crack positions. A total of 90 samples were generated with crack lengths between 1 and 3 mm, crack heights between 0.55 and 0.95 mm and crack position around the region of interest as shown in Figure 9-36. The combinations of parameters are fully randomized as shown in Figure 6-1.

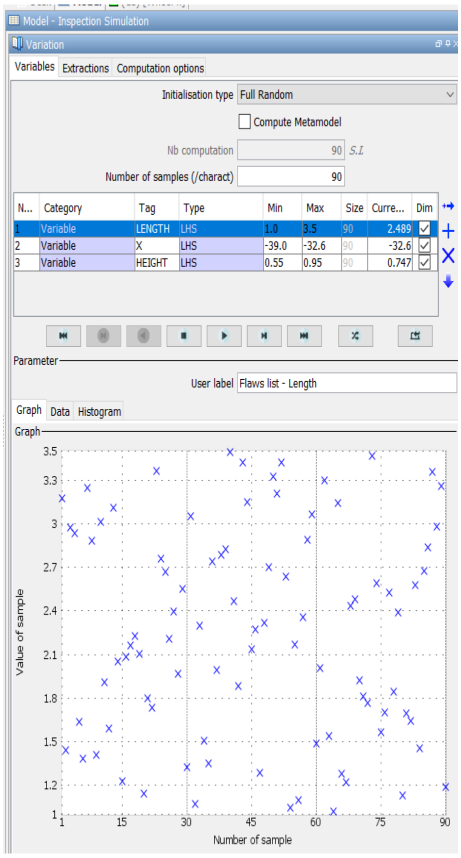

Initialisation type: Full Random

☐ Compute Metamodel

Nb computation: 90 S.I

Number of samples (/charact): 90

N...	Category	Tag	Type	Min	Max	Size	Curre...	Dim
1	Variable	LENGTH	LHS	1.0	3.5	90	2.489	☑
2	Variable	X	LHS	-39.0	-32.6	90	-32.6	☑
3	Variable	HEIGHT	LHS	0.55	0.95	90	0.747	☑

User label: Flaws list - Length

Figure 6-1 Sample set used for the POD analysis.

A larger sample set size with more variation in each variable would give a more accurate POD analysis. However the number of samples are limited due to time constraint. Thus the number of samples used is a compromise between quality of the POD analysis and the practical limitations bounded by time and computation power. Generating a sample set with 90 samples requires a computation time of 36 hours.

6.2 POD calculation method

Since the hit/miss method is used to perform a POD analysis the results samples are divided in two groups: hit and miss based on the earlier defined threshold. The threshold is defined to be 40% in signal strength. Thus when 40% FSH is reached during inspection, the aircraft part shall be removed for further inspection and will be considered as hit. Anything below 40% FSH is considered as a miss. The next step is to put the samples on a chart with the crack length on the x-axis and the POD (between 0 and 1) on the y-axis, as shown in Figure 6-2.

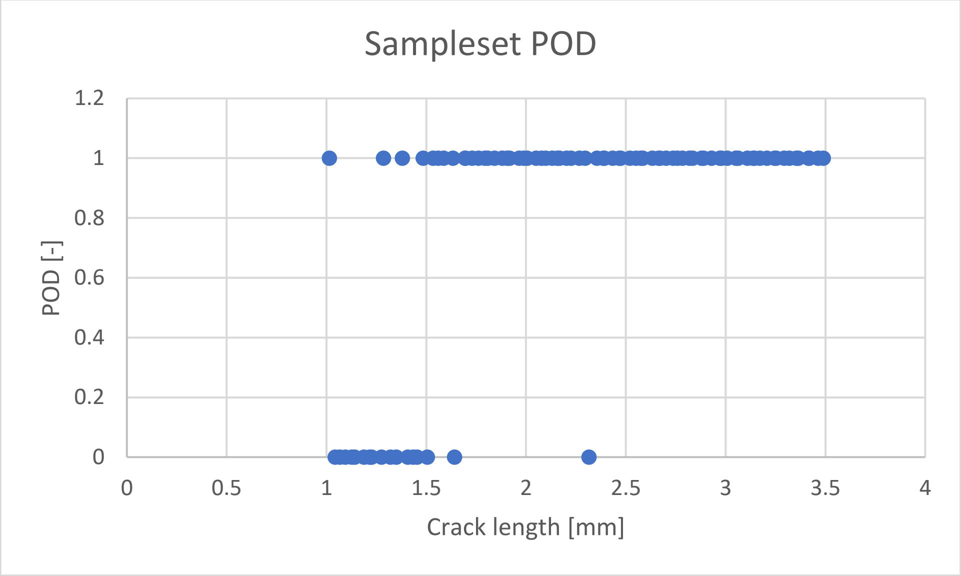

Figure 6-2 Sample set data used for the POD analysis plotted in a chart.

As expected a larger crack length is more likely to be detected than a smaller crack length. However other factors, like crack height and crack position, which are variables in included in the sample set, also influence the POD. Therefore it is possible that a larger crack length can be missed while a smaller crack length can be a hit.

From the data in Figure 6-2 a POD curve can be obtained using models like Logit and Probit [12]. The POD curve is obtained in Matlab using the logit.

6.3 Results POD analysis

The first POD curve generated is obtained from data with 2 variables: crack length and crack depth having 60 samples in total. The dataset of this sample can be found in Appendix C. The result of the POD curve is shown in Figure 6-3

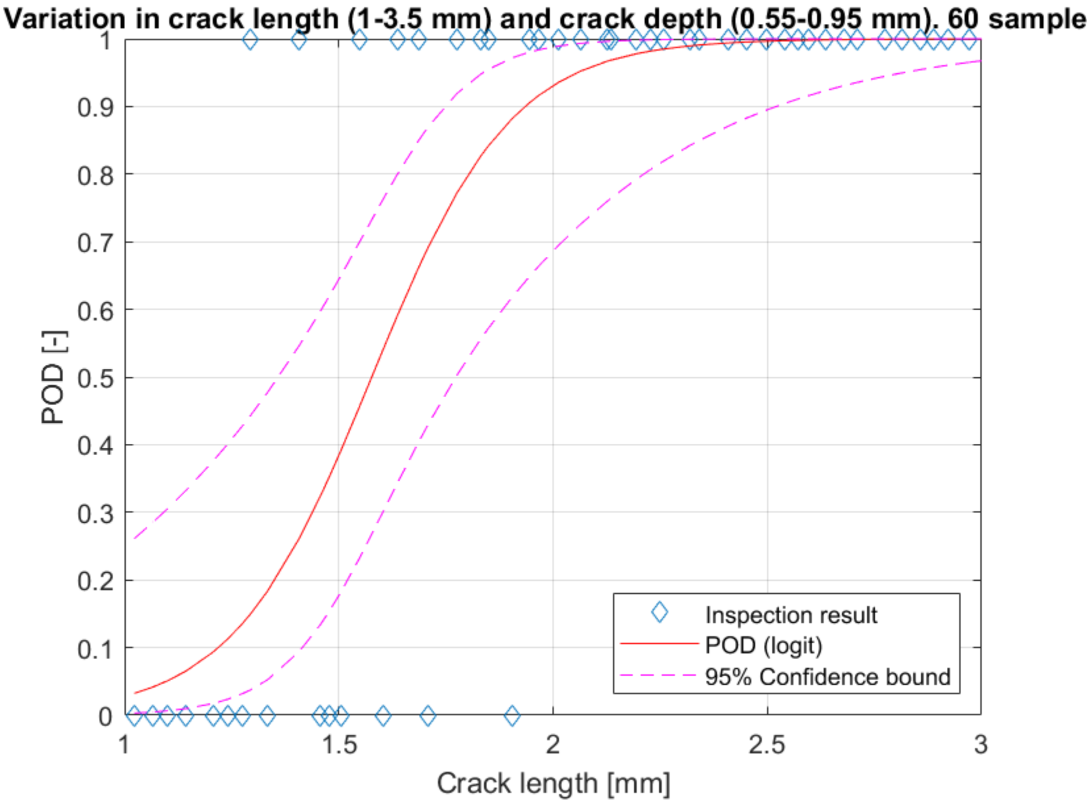

Figure 6-3 POD analysis crack length and crack depth variation. $a_{90/95}$ is found to be 2.5 mm in this case.

Eventually the POD analysis was performed with 90 samples having a variation in crack length, crack height and crack position. This POD curve is shown in Figure 6-4.

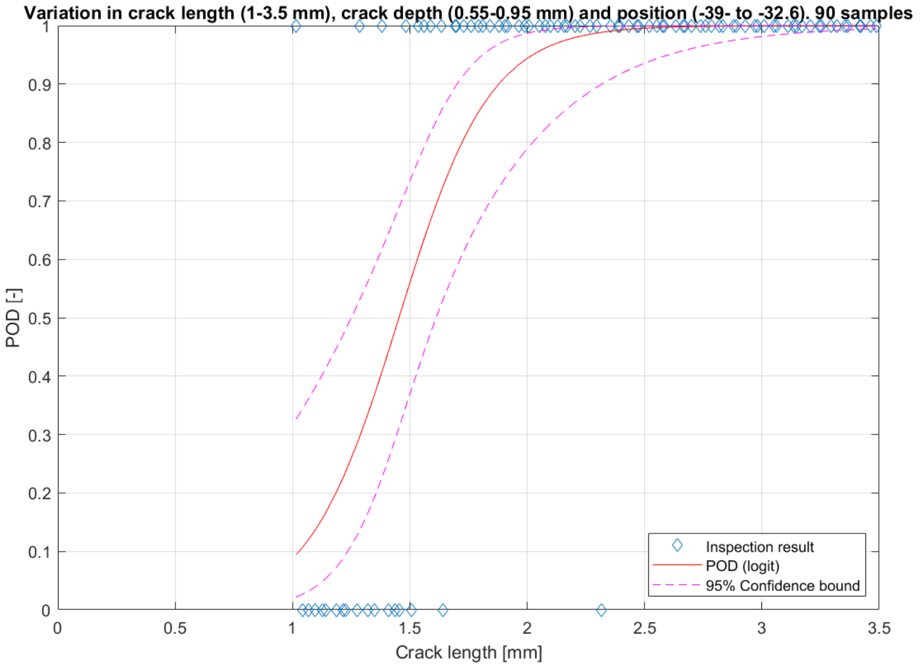

Figure 6-4 POD analysis with 90 samples with a variation in crack length, crack height and crack position. The corresponding $a_{90/95}$ value is 2.32 mm.

$a_{90/95}$ was found to be 2.32 mm, which exceeds the critical crack length of 2 mm mentioned in [10]. In the POD calculation the following parameters have not taken into account:

- Noise (attenuation)
- Human factors
- Variation in the sensor (transducer)
- Uncertainty of wedge position (transducer is always perpendicular to the flaw)
- Presence of a wobbling due to mismatch of radius between the wedge and the test specimen

The influences of not taking the above mentioned variables into account are discussed in chapter 7, where the POD analysis is used to decide whether the inspection method is suitable for the RNLAF to achieve the goal of the inspection.

The effect of the wobble can be seen in Appendix B.1. A wobble of 1 degree causes a reduction of 23% in signal strength.

The POD is a parameter that is required to certify the NDI method. The certification process of NDI methods will be discussed in chapter 7.

7 Certification of the NDI method

The goal of certifying an NDI method is to determine its reliability to detect flaw before it reaches a critical value. It is important to make sure that the new NDI method is capable to ensure structural integrity. Before an NDI method can be put into operational used, it should be evaluated in terms of the limits of operational parameters and range of application to demonstrate that the system is in control [12].

The chosen NDI method that is chosen needs to meet criteria which are defined beforehand. If a new NDI method is proposed to supersede a currently used NDI method, then the criteria that needs to be fulfilled can be used as baseline. However, just demonstrating that the new NDI method is capable in detecting a smaller flaw length is not sufficient to proof that it is suitable to replace the current NDI method. This is due to the fact that the entire system is influenced by a multitude of factors.

7.1 Variables to consider for certification

In order to certify an NDI method, variables which are relevant to the inspection need to be identified an tested. The most trivial variable is the sensitivity of a certain NDI method, like what flaw size can it detect and from which material. However there are other variables that play a role in the results of the inspection. Which variables are significant vary case by case. MIL-HDBK-1823 gives the following types of variables that should be considered as a minimum to perform a reliability test of the NDI method [12]:

- Specimen pre-processing
- Inspector
- Inspection materials
- Sensor
- Inspection setup (Calibration)
- Inspection process
- Imagine consideration

7.2 Certification procedure

Based on these variables a test matrix needs to be constructed for the reliability demonstration. The test matrix is a list with test conditions that need to be evaluated. The number of experiments that needs to be performed depends of the number of significant variables that need to be evaluated. If all combinations of variables need to be tested then a very large number of tests need to be performed and the number of test specimen required are enormous. One can reduce the number of tests by measuring the influence and variability of important valuables. Constructing a test matrix is an interactive process and the definitive test matrix shall be a compromise between number of variables, range of the variables, and availability of resources like number of specimen, time available and money.

The required number of specimen for a reliability analysis depends on whether the inspection is a hit/miss inspection or $\hat{a}$ vs a (signal strength) inspection. For hit/miss inspections the reliability analysis requires a minimum of 60 test specimen to be evaluated and for a $\hat{a}$ vs a the minimum required number of specimen is 40 [32]. If one needs to determine the false positive rate then unflawed test specimen needs to be included. To reduce the number of test specimens required, MAPOD can be considered as described in section 2.3.4.

Once the required experiments are performed on the test specimen according to the final test specimen a probabilistic analysis shall be made, the POD analysis with a POD(a) curve as an output. The POD(a) curve gives the relation between the POD and the flaw size.

7.3 Result presentation

Once the reliability analysis has been performed and the POD curve for the NDI method is obtained the results need to be analysed and presented to the operator. From MIL-HDBK-1823A data should be reported in 4 areas, namely the description of the system, the experimental design, the individual test results and a summary of the results.

7.3.1 The description of the system

The description of the system describes how the inspection needs to be performed. Which details of the system needs to be reported depends on the type of NDI method. The purpose of recording this information is to identify the specific system that has been evaluated. As general guideline the description of the system for ultrasound inspection should contain information about:

- Test parameters
- Fixed process parameters (specifications of the equipment used)
- Specimen fabrication and maintenance
- Testing procedure (objective of the test)
- Presentation of the results (including all raw data from the tests)

7.3.2 The experimental design

The experimental design describes the batch of test specimens used for the demonstration inspection. In this recording the classification (hit/miss or $\hat{a}$ vs a inspection) shall be mentioned as well as the specification required and calibration of the equipment.

7.3.3 Individual test results

This is basically the record of each result from every tests performed. It is important to record all the variables of each individual test specimen used for the reliability demonstration, so that one can see what influences certain variables have on the inspection.

7.3.4 Summary test results

From the individual test result report a summary of the test results can be made. In the summary the data analysis results shall also be presented.

7.4 Certification of PAUT for a complex aluminium aircraft part.

Now a general description has been given how to certify a new NDI method in general, the research question can now be considered. The research question is “How can phased array ultrasound be certified for a complex aluminium aircraft part?”.

To start of one needs to define the intended use of the inspection carefully, like the shape of the material and the type of flaw that needs to be detected and in what conditions the experiment will be performed. For a complex aluminium aircraft part the geometry, material specifications, part processing, surface condition and the operational characteristics need to be known in order to predict the possible failure mode(s) of that specific aircraft part.

If the goal of the phased array ultrasound inspection is meant to replace a previous NDI method, then the goal of the inspection and the specifications of the aircraft part are known. However if a totally new inspection is being introduced then the purpose of the inspection needs to be defined along with the requirement in sensitivity as it should be known what the minimum flaw size is that needs to be detected, or the maximum flaw size that can be missed.

Once the purpose of the inspection is known one can start making the reliability demonstration plan by looking at what variables are relevant that has a significant impact on the inspection. Having determined the significant variables a test matrix can be constructed. Once the final test matrix has been constructed the question is how many test specimens are required and types of flaws those need to contain. Since complex aluminium aircraft parts are scarce it is very likely that MAPOD needs to be used to assist in the certification process. A model needs to be constructed first and the test specimen in the model must match the aircraft part when the inspection is performed. The simulation of the inspection must be calibrated such that it matches with inspection performed on physical components. The model shall be validated against actual inspection results, either by comparing the results of inspections performed on different test specimen or inspecting the same test specimen multiple time by performing the inspection differently. If the model does not provide accurate data within the range the inspection is expected to be performed, the model needs to be fine-tuned to improve on accuracy. Once the model is constructed, different inspections need to be performed according to the test matrix. The results shall then be used to obtain a POD – flaw size relationship.

The POD – flaw size relation shall be used to determine the reliability of the phased array ultrasound inspection method. An evaluation shall be made whether the reliability test performed on the system is sufficient to proof that the system is capable to perform the inspection it is intended to. If the reliability analysis has determined that the inspection procedure is insufficient to perform its task then the procedure should be re-evaluated and updated accordingly. The certification process shall be performed again.

7.4.1 Case study RNLAF

The case study for the RNLAF was used to find out what is needed to certify phased array ultrasound on a curved aircraft part made of aluminium. The new NDI method is to supersede the currently required eddy current inspection which cannot be performed easily as it requires removal of the part. Phased array ultrasound inspection omits the need to remove the part as inspection can be performed on the accessible side of the aircraft part. This saves time and costs and prevents unwanted wear and tear due to removal / installation procedures. The intention of the inspection is already known, well as the specification of the material and the type of flaw it needs to detect. Furthermore the RNLAF already has an inspection procedure written down. The procedure contains instruction how to calibrate the phased array flaw detector and gave a decision criteria when to remove the aircraft part for a detailed inspection. The goal of the case study is to certify the procedure of using phased array for crack detection of the aluminium aircraft part.

7.4.1.1 Certification procedure

For the certification of this procedure there is only one test specimen available containing an EMD notch. Originally this specimen was used to calibrate the eddy current NDI sensor. The specimen is described in detail in section 3.1.3. Since there is only one test specimen available containing only one flaw it is not possible to perform physical experiments only and MAPOD is required to assist in the certification process. With MAPOD it can be investigate how the flaw detector react at different properties of the flaw like length, depth and location. A model was constructed in CIVA which was explained in chapter 4. Since there is only one EMD notch present at the physical test specimen, the model cannot be validated against differences in flaw orientations. However the accuracy of the model can be validated by simulating inspections performed in different ways. For validation purpose of the model a test matrix was constructed with different combinations in the guide position, which determines the transducer position applied at the test specimen. The test matrix is shown in section 3.3 and the test experiments in the test matrix were performed physically and simulated. The comparison of the physical experimental results and simulated results and the accuracy of the model are discussed in chapter 5. It was determined that the model was accurate enough when the right aperture position was chosen and the guide position was neutral. The most accurate situation corresponds with settings required by the RNLAF inspection instruction.

The next step is to perform a large number of simulated inspections based on the RNLAF's instructions with a variety in crack length, crack depths and crack location within the region of interest. The results of the simulated inspections shall be used for a POD analysis where the POD(a) will be obtained and the $a_{90/95}$ of this inspection shall be determined. A total of 90 inspections were simulated, which was a compromise between accuracy and computation time. It took 1.5 days to complete the simulation. The simulated results gave an $a_{90/95}$ value of 2.32 mm.

7.4.1.2 MAPOD limitations

The MAPOD analysis performed came with some limitations. Firstly the simulated inspections were performed on 90 specimen with a combination of 3 variables and no other uncertainties were taken into account. The variables were all relate to the flaw dimensions. Uncertainties from the phase array ultrasound flaw detector as well as from human factors are not taken into account.

For this case study human factors have a large influence on the outcome of the inspection. The first and most influential parameter is the presence of a wobble between the aircraft part and the wedge due to a mismatch in the radius. The effect is shown in Appendix B.1. It can be seen that wobble of 1 degree causes a 20% reduction in signal strength. A wobble of 4 degrees causes an 80% reduction in signal strength.

Another uncertainty that may occur from performing the inspection is the influence of the guide position. The effect is less severe compared with the presence of a wobble, which is demonstrated in Appendix B.2. However both uncertainties can be mitigated. The wobble can be mitigated by applying tapes on the edges of the wedge such that the radius of the wedge matches with the radius of the aircraft part much better. As for the guide position, this can be fixed by tighten the screws and movement of the guide during the inspection is no longer possible. Because these uncertainty could be mitigated in such a way that when multiple physical inspections are performed at the same specimen, the results are consistent.

Another factor that was left out in the model is noise attenuation. The effect of noise can be witnessed in the S scans comparison section, which can be found in Appendix A. When the signal strength is strong, noise is not an issue. Noise is an issue when the signal strength is below 50% if we include the comparisons with different aperture positions as shown in section 5.5.1. However when we only look at the aperture position when elements 17 to 32 are being used, it can be seen that simulated signal strengths and signal strengths from physical inspections are consistent up until 30 %. Let's recall that at a signal strength of 40% the aircraft part needs to be removed. Therefore even when noise is not included in the model, the model provide accurate enough results within the range the inspection is expected to be performed.

7.4.1.3 Discussion results case study RNLAF inspection procedure

Based on the MAPOD analysis the inspection of the RNLAF does not meet the criteria of the intention of the inspection. The critical crack length was previously determined to be 2mm [9], but the obtained value for $a_{90/95}$ is 2.32 mm. The raw data used to perform the POD analysis can be found in Appendix C. Looking at the raw data it can be seen that the largest flaw length that was missed was 2.3mm. The flaw in this specimen has the following properties:

Length [mm]	Pos [mm]	Height [mm]	Amplitude [%]	Hit/miss
2.316	-33.30	0.58	23.39	0

The miss of this inspection is mainly caused by the position of the flaw, for which the definition is shown in Appendix B.6. The flaw is thus located far away from the centre radius and is far near the edge which is a location the soundwaves cannot reach easily. The second largest and third largest crack lengths that can be missed are 1.64 mm and 1.5 mm respectively. The smallest value that can be detected is 1.01 mm. The properties of the smallest flaw that can be detected are:

Length [mm]	Pos [mm]	Height [mm]	Amplitude [%]	Hit/miss
1.01	-36.05	0.75	41.52	1

It can be seen that the flaw is located at a more favourable position and the flaw height is bigger. Thus by analysing the raw data it can be observed that the position of the flaw has a large influence on the detectability of the flaw with a certain length. The crack height also influences the detectability of the flaw, but the effect is not as large as the position.

7.4.1.4 Recommendation for the case study

Based on the results the potential PAUT inspection technique for the aircraft part is insufficient for the RNLAF for fatigue cracks as it has the potential to miss cracks exceeding the critical crack length of 2 mm. However when the raw data was investigated it could be seen that the miss is largely caused by the unfavourable position of the flaw. Based on this finding an investigation should be conducted about the likelihood of where fatigue cracks initiate. If the result turns out that cracks initiate most often at or near the centre radius, then the current inspection is sufficient. However if cracks initiate as often at the edge of the radius as at the centre radius, then the inspection method needs to be revised. Ways to improve the detectability of flaw at the region of interests are performing the inspections multiple times using different aperture positions or reduce the decision criteria to remove the aircraft part for further inspection. A possible disadvantage is that the aircraft part would be removed more often than necessary, which thus increases the chance of getting false positives. To overcome this disadvantage one could analyse the chance this inspection gives a false positive, which was not analysed throughout this certification process.

8 Conclusions and recommendations

The purpose of this study was to find out how phased array ultrasound can be certified for a complex aluminium aircraft part. This research question was formulated after a thorough literature study was performed on the aircraft material, including NDI techniques, phased array ultrasound, POD analysis and certification procedures of new NDI methods. To put this in practice a case study was taken from the RNLAF where phased array ultrasound inspection is being used to supersede a less practical eddy current inspection. The eddy current inspection requires the aircraft part, made of aluminium, to be removed as the inspection needs to be performed at the side where possible cracks are present. Phased array ultrasound inspection has the potential to perform the inspection at the opposite side, which is accessible on-aircraft. This would simplify the inspection procedure, save time and reduce risks caused by the removal / installation procedure of the aircraft part.

However new NDI cannot be bought off the shelve and replace the current NDI method by using the newly acquired equipment. Before the new NDI procedure can be used it has to be certified that it is airworthy. Certifying a new NDI method is an intensive task as various aspects need to be taken into account to ensure that the method is suitable to perform the inspection and detect the types of flaws it is required to detect.

In order to certify a phased array ultrasound inspection on a metallic part, a detailed instruction of the inspection needs to be available, including the test specimen, the settings of the NDI equipment, the calibration procedure and the decision criteria. For the test specimen, the material specification, the type of flaws the NDI inspection is required to detect and the geometry need to be known. In some cases the production procedure and the operational environment needs to be known as these information can be used to predict the initiation of flaws. If the phased array ultrasound inspection is used to replace an existing inspection, then the criteria of the previous inspection can be used as baseline and the new inspection procedure should demonstrated to be at least equivalent to the previous inspection method.

Furthermore, variables that significantly influence the outcome of the inspection need to be identified. Once these variables have been identified, a test matrix can be constructed a to determine how many test specimens are required for the reliability demonstration. In the test matrix all combinations of variables and in which range each individual variable needs to be can be included.

Since complex aircraft parts, and producing sufficient test specimens are expensive, manufacturing each specimen containing flaws with a combination of different parameters is not always feasible, and thus MAPOD can be considered. To use MAPOD a model needs to be created where both the test specimen and the inspection conditions shall be modelled in such a way that simulation results can be obtained that is representative to the physical inspection conditions. The model shall be validated against actual inspection results to make sure that the model provides sufficiently accurate data within the range of the inspection.

Once the model can predict inspection results accurately, a POD analysis can be performed from the (simulated) inspection results. The results can either be hit/miss data or $\hat{a}$ vs a (signal response) data. The minimum number of inspections is required for an accurate POD analysis depends on the type of inspection. Both the accuracy of the model used to perform simulations and the number of simulated inspections that can be generated are a compromise of accuracy, time, computation power available and money available. The POD analysis shall provide the relation between the POD and flaw size. The output shall be the value of $a_{90/95}$, which is the crack length having a probability of detection of 90% within the confidence bound of 95%. The critical flaw size should be below the $a_{90/95}$ value, which means that the inspection is sensitive enough to detect the flaw before it becomes critical.

Apart from the POD analysis, the raw data used for the POD analysis needs to be investigated and each inspection result shall be reported. If the $a_{90/95}$ value seems to be higher than desired, one can trace back and see under which circumstances the largest flaw size can be missed. For the case study it showed to be very valuable. Looking at the raw data it was figured out that the largest flaw that was missed during the inspection was due to the fact the flaw was located at a very unfavourable position. When analysing the individual data one should look carefully at the largest flaw size that was missed and the smallest flaw size that was detected. One should also look at the entire dataset to see what variables really have huge influences on the detectability of the flaw, so that the inspection method can be revised to improve the detectability of smaller flaw size if needed.

8.1 Conclusion to the research question

The purpose of this research is investigate how phased array ultrasound can be certified for a complex aluminium aircraft part. The main research question was: How can phased array ultrasound be certified for a complex aluminium aircraft part? In order to answer this main question two sub questions were formulated:

1. What beam forming technique provides the best result for this case considering computation time and accuracy?
2. How can model assisted probability of detection assist in the certification process?

8.1.1 What beam forming technique provides the best result for this case considering computation time and accuracy?

To answer the first question the purpose of the inspection needs to be defined as different beam forming techniques are suitable for different applications. However when complex aluminium aircraft parts are involved most of the time sectoral scans shall be used due to its capability to sweep through the ROI. Using high aperture settings provide the clearest results. The beam angle need to be selected such that the most common flaw location is located at the centre of the beam. Synthetic beamforming like SAFT, FMC and TMC are not recommended because the data processing requirement increases the inspection time significantly.

8.1.2 How can model assisted probability of detection assist in the certification process?

In order to answer the second sub question the case study can be used as reference. In order to use MAPOD to assist in the certification process a model needs to be constructed that is capable of predicting inspection results with sufficient accuracy within the range the inspection is to be performed. Thus it is important to have a software package, like CIVA, which can simulate the inspection that needs to be certified. In order to achieve high accuracy one needs to model the test specimen. It is crucial to get the dimensions and the material specifications correct as the result depends on the interaction between the transducer, the wedge and the test specimen. The material specification is important to predict the sound propagation through the material. Generally standard material specifications can be chosen for aluminium parts as aluminium parts are homogenous materials.

The next step is to simulate the phase array flaw detector. For the phased array flaw detector model it is important to select the right transducer and the right wedge. If standard part numbers are used, there is a chance that the specific equipment is already included in the database.

When the model is constructed, it should be validated against the actual physical inspections. At least two measurement points are needed to determine the accuracy of the model. One measurement is the standard case to calibrate the model. A second physical measurement is needed to determine if the model provides the same change if a variable is changed. Ideally this should be another flaw with other dimension. For the case study it would have helped if extra notches were included in the test specimen.

The answer to this sub question is: *MAPOD can assist in the certification process by providing simulated results required to perform a POD analysis. This is especially useful when a large number of test specimen cannot be obtained. However the accuracy and the limitations of the model shall be known and a decision has to be made whether the accuracy and the limitations are acceptable.*

8.1.3 Overall conclusion

In order to certify a phased array ultrasound inspection for complex aircraft parts, it is important to determine the purpose and the requirements of the inspection. Every phased array ultrasound inspections that need to be certified against air worthiness is different but based on this research a general guideline can be given how to certify phased array ultrasound inspections for complex aluminium parts.

The answer to the research question is as follows: *phased array ultrasound testing can be certified when the intended use of the inspection is known. Based on the intended use of the inspection the type of beam forming technique shall be selected and a reliability analysis shall be performed to ensure that the inspection is capable in detecting the type of flaws under the conditions at which the inspection is expected to be performed. Normally a large number of inspection results is required for the certification process. However MAPOD can be used to assist the certification process by providing simulated inspection results required for the reliability analysis.*

8.2 Recommendations

For the case study MAPOD was used to assist the certification procedure of a PA ultrasound inspection on a complex metallic aircraft part. On overall the case study has shown that MAPOD is useful as it provided a sufficiently large number of simulated results which could be used to perform a POD analysis. Throughout the process of the case study lessons were learned how to make the process smoother. In this section some recommendations are given for the physical experiment, the simulation procedure and the POD analysis.

8.2.1 Recommendations on the physical experiment

During the physical experiment phase it was found out that the wedge did not match with the aircraft part. As a result a wobble was present making it harder to get consistent inspection results. The problem was partly solved by applying tapes on the side of the wedge as shown in Figure 3-9. A recommendation is to make sure that the test equipment matches with the test specimen before performing inspections.

For the case study only one specimen was available with one flaw present. This limits the possibility to obtain a relationship between flaw response and flaw size from experiments, which would have been helpful in validating the model used to perform the MAPOD analysis. A recommendation is to add another notch on the same test specimen so that a relationship between flaw response and flaw size can be obtained which is a better parameter to validate the model as for the POD analysis a POD curve versus flaw size *a* is to be obtained. The goal of MAPOD is to reduce the number of test specimens and number of inspections required. However the number of test specimens and number of inspections required cannot be reduced to zero.

For the MAPOD analysis not all variables that influences the inspection result can be simulated. One of the variable that cannot be simulated is human factors. In order to determine the effect of human factors, multiple inspectors can perform an inspection and the inspection results can be analysed for consistency. It is important that the inspectors performing the inspections are representative to the inspectors that will perform the inspection.

8.2.2 Recommendations on the NDT inspection simulation

The model used to perform the NDT inspection simulation was determined to be accurately enough to be used to generate data for the POD analysis when the guide position and the array settings match with the default case. The model can be made more accurately by including noise. This can be seen in Appendix A where the S scans of the physical inspections and the simulated inspections are compared. It can be seen that the S scans of the simulated inspections are much cleaner. The discrepancy in shot angle, sound path length and TOF can be further optimized by approximating the axial position of the wedge better. This can be achieved by performing a variation study with smaller intervals between axial positions.

8.2.3 Recommendations on the MAPOD analysis

For the MAPOD analysis it is recommended to construct a test matrix beforehand including all the identified variables that influences the inspection. A clear overview of which variables are included in the MAPOD analysis. The test matrix can also be used to determine how significant a variable has on the inspection, and it can show which variables cannot be included in the MAPOD analysis, like human factors.

For the MAPOD analysis it is recommended to include a larger sample set with more variables. For example a variation in squint angle could have been included to simulate the presence of a wobble, which is partly corrected but not fully eliminated. A larger sample set results in a more accurate POD - *a* relationship, but due to time constraint the MAPOD analysis was limited to 3 variables and a sample set of 90 test results.

9 Bibliography

[1] G. J. Weaver, “NDT of Medical Devices,” Quality Magazine, 29 November 2020. [Online]. Available: https://www.qualitymag.com/articles/96308-ndt-of-medical-devices. [Accessed 6 May 2022].

[2] A. Bahadori, “General Requirements for the Purchase of Pipes for Use in Oil and Gas Industries,” in *Oil and Gas Pipelines and Piping Systems*, Lismore, Gulf Professional Publishing, 2017, pp. 155-193.

[3] A. Mouritz, “Chapter 23 - Nondestructive inspection and structural health monitoring of aerospace,” in *Introduction to Aerospace Materials*, Cambridge, Woodhead Publishing, ISBN: 9780857095152, 2012, pp. 534 - 557.

[4] G. Workman, Nondestructive Testing Handbook Ultrasonic Testing, 3 ed., vol. 7, American Society for Nondestructive Testing, ISBN: 978-1-57117-105-4, 2007.

[5] X. Wang, “Three-dimensional damage quantification of low velocity impact damage in thin composite plates using phased-array ultrasound,” *Ultrasonics,* vol. 110, 2021.

[6] S. Azeez, “Radiography examination of friction stir welds of dissimilar aluminum alloys,” *Materials Today: Proceedings,* vol. 57, 2022.

[7] North Star Imaging, Inc, “A Guide to Using Digital Radiography in the Aerospace Industry,” AZoM, 04 April 2022. [Online]. Available: https://www.azom.com/article.aspx?ArticleID=13526. [Accessed 7 May 2022].

[8] B. Kenaston, “Ultrasonic Drone Inspections Take NDT Safety to New Heights,” *e-Journal of Nondestructive Testing (NDT),* no. 2021-05, 29 April 2021.

[9] E. Amsterdam, “Failure analysis of a wheel rim, NLR-CR-2016-170,” NLR, Amsterdam, 2017.

[10] E. Amsterdam, “Fractography on a wheel rim, NLR-CR-2019-466,” NLR, Amsterdam, 2019.

[11] J. Platenkamp, “Phased Array Ultrasonic Testing on aircraft wheels for crack detection, NLR-CR-2020-347,” Royal Netherlands Aerospace Centre, Marknesse, 2020.

[12] MIL-HDBK-1823A ”Nondestructive Evaluation System Reliability Assessment”,”, Ohio: Department of Defense, 2009.

[13] A. Mouritz, “Chapter 3 - Materials and material requirements for aerospace structures and engines,” in *Introduction to Aerospace Materials*, Cambridge, Woodhead Publishing, ISBN: 9780857095152, 2012, pp. 39-56.

[14] A. Mouritz, “Chapter 15 - Fibre–polymer composites for aerospace structures and engines,” in *Introduction to Aerospace Materials*, Woodhead Publishing, ISBN: 9780857095152, 2012, pp. 338-393.

[15] J. Cutler and J. Liber, Understanding Aircraft Structures, Wiley, ISBN: 978-1-405-12032-6, 2006, p. 224.

[16] AMS, Fatigue and Fracture, vol. 19, ASM International, ISBN: 9780871703859, 1996, p. 1057.

[17] H. A. Wood and R. M. Engle, “USAF Damage tolerant design handbook Guidelines for the Analysis, ADA078216,” United States Air Force, Ohio, 1978.

[18] “Basic Principles of Ultrasonic Testing,” Iowa State University, [Online]. Available: https://www.nde-ed.org/NDETechniques/Ultrasonics/Introduction/description.xhtml. [Accessed 27 February 2022].

[19] N. Dubé, Introduction to Phased Array Ultrasonic Technology Applications, Waltham: Olympus, ISBN 0-9735933-0-X, 2004.

[20] K. Hashimoto, Surface Acoustic Wave Devices in Telecommunications, Berlin: Springer Berlin Heidelberg, ISBN 978-3-642-08659-5, 2000.

[21] N. Dubé, Advances in Phased Array Ultrasonic Technology Applications, Waltham: Olympus, ISBN 0-9735933-4-2, 2007.

[22] ASM, Nondestructive evaluation and quality control, vol. 17, Metals Park, Ohio: ASM International, ISBN: 9781615834365, 1989.

[23] P. S and M. Reddy, “Impact damage assessment in carbon fiber reinforced composite using vibration-based new damage index and ultrasonic C-scanning method,” *Structures,* vol. 28, pp. 638-650, 2020.

[24] M. Caminero, I. C. Moreno, G. Rodríguez and J. Chacón, “Internal damage evaluation of composite structures using phased array ultrasonic technique: Impact damage assessment in CFRP and 3D printed reinforced composites,” *Composites Part B: Engineering,* vol. 165, pp. 131-142, May 2019.

[25] Olympus, *Using the Total Focusing Method to Improve Phased Array Ultrasonic Imaging,* Olympus, 2020.

[26] E. Carcreff, D. Braconnier and G. Dao, “Fast total focusing method for ultrasonic imaging,” *IEEE International Ultrasonics Symposium (IUS),* pp. 1-2, 2015.

[27] C. Holmes, B. W. Drinkwater and P. D. Wilcox, “Post-processing of the full matrix of ultrasonic transmit-receive array data for non-destructive evaluation,” *NDT & E International,* vol. 38, pp. 701-711, 2005.

[28] J. Zang, B. W. Drinkwater and P. D. Wilcox, “Effects of array transducer inconsistencies on total focusing method imaging performance,” *NDT & E International,* vol. 44, no. 4, pp. 361-368, 2011.

[29] M. Sutcliffe, M. Weston, P. Dutton, P. Charlton and K. Donne, “Real-time full matrix capture for ultrasonic non-destructive testing with acceleration of post-processing through graphic hardware,” *NDT & E International,* vol. 51, pp. 16-23, 2012.

[30] G. Giovanis, “Damage detection using phased array ultrasound and data analysis using artificial intelligence.,” University of Patras, Patras, 2020.

[31] W. Rummel, “Recommended practice for a demonstration of non-destructive evaluation (NDE) reliability on aircraft production parts,” *Material Evaluation,* vol. 40, 1982.

[32] P. W. Hovey and A. P. Berens, “Statistical Evaluation of NDE Reliability in the Aerospace Industry,” *Review of Progress in Quantitative Nondestructive Evaluation,* pp. 1761-1768, 1988.

[33] G. A. Georgiou, “Probability of Detection (PoD) curves Derivation, applications and Limitations,” Jacobi Consulting Limited, London, 2006.

[34] M. S. Safizadeh, D. S. Forsyth and A. Fahr, “The effect of flaw size distribution on the estimation of POD,” *Insight - Non-Destructive Testing and Condition Monitoring,* vol. 46, no. 6, pp. 355-359, 2004.

[35] A. Keprate and R. Ratnayake, “Probability of detection as a metric for quantifying nde reliability: The state of the art,” *The Journal of Pipeline Engineering,* vol. 14, pp. 199-209, 2015.

[36] A. Keprate, “Probability of detection: History, development and future,” *Pipeline Technology Journal,* vol. 8, no. 3, pp. 41-45, 2016.

[37] H. Shan and L. H. Chen, “The Developments of Simulation Software for Ultrasonic Testing,” *17th World Conference on Nondestructive Testing,* p. 6, 2008.

[38] “Imagine3d ultrasonic simulation software version 2.5 user’s Manual,” 2008. [Online]. Available: https://www.utex.com/webapps/utexsupport.nsf/wPages/MSZI-7AXTNL5256/$File/i3dmanual2.5.pdf. [Accessed 7 May 2022].

[39] H. H. Douglas and J. Spanner, “Virtual NDE operator training and qualification,” *The e-Journal of Nondestructive Testing,* vol. 104, no. 10, 1999.

[40] “CIVA in a few words,” Extende, [Online]. Available: https://www.extende.com/civa-in-a-few-words. [Accessed 7 May 2022].

[41] Olympus, *Phased Array Probes and Wedges,* Waltham: Olympus, 2010.

[42] Olympus, “Univertal Probes,” [Online]. Available: https://www.olympus-ims.com/en/probes/pa/universal/.

[43] *CIVA NDE 2020 User Manual,* Extende, 2020.

Appendix A S Scans test matrix

In this appendix the S scans of the test cases of Table 3-4 are shown. The S scans obtained from physical experiments and from simulations are put next to each other so that the figures can be compared easily.

Appendix A.1 Results S scan using elements 17 to 32

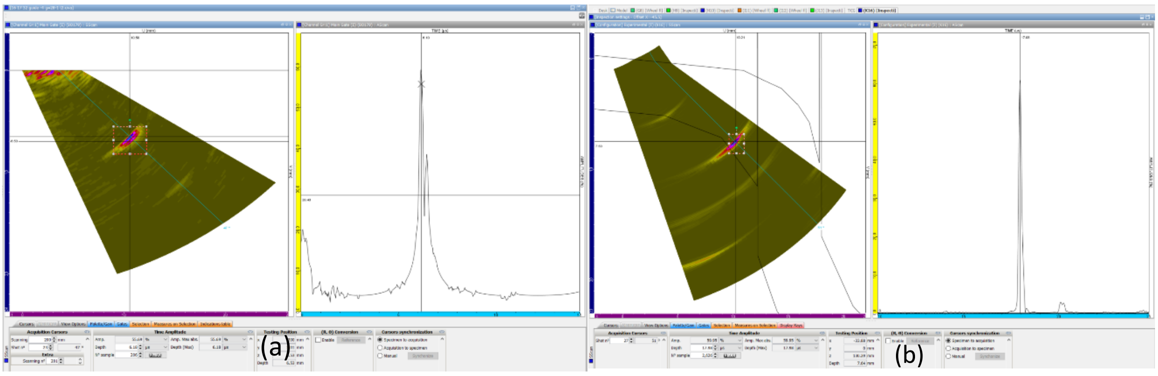

Figure 9-1 Result S scans test case 1 obtained from physical experiment (a) and simulation (b).

b).

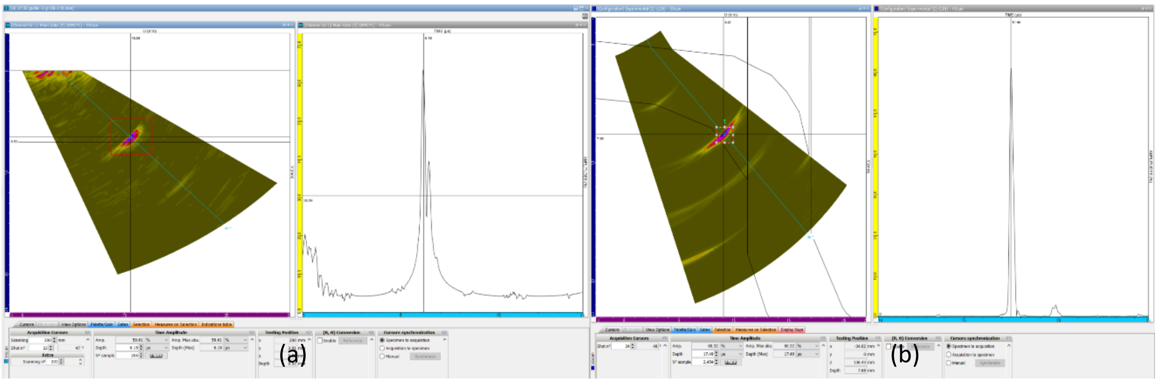

Figure 9-2 Result S scans test case 2 obtained from physical experiment (a) and simulation (b).

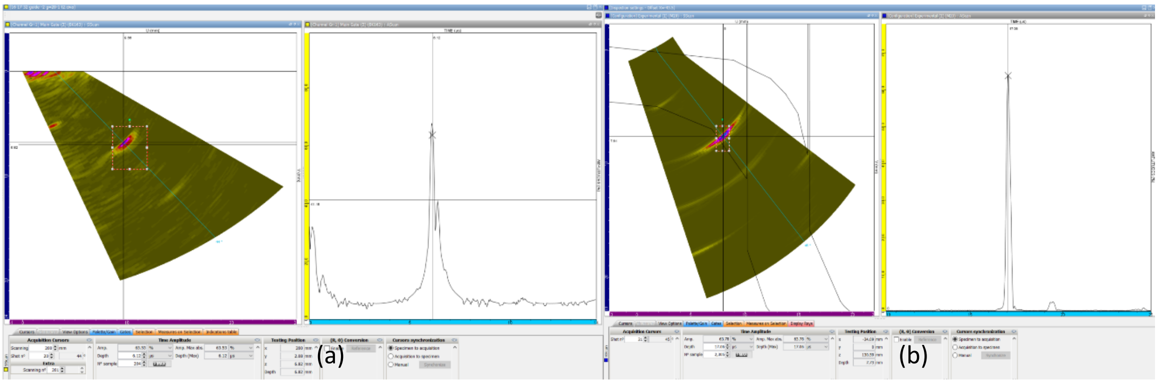

Figure 9-3 Result S scans test case 3 obtained from physical experiment (a) and simulation (b).

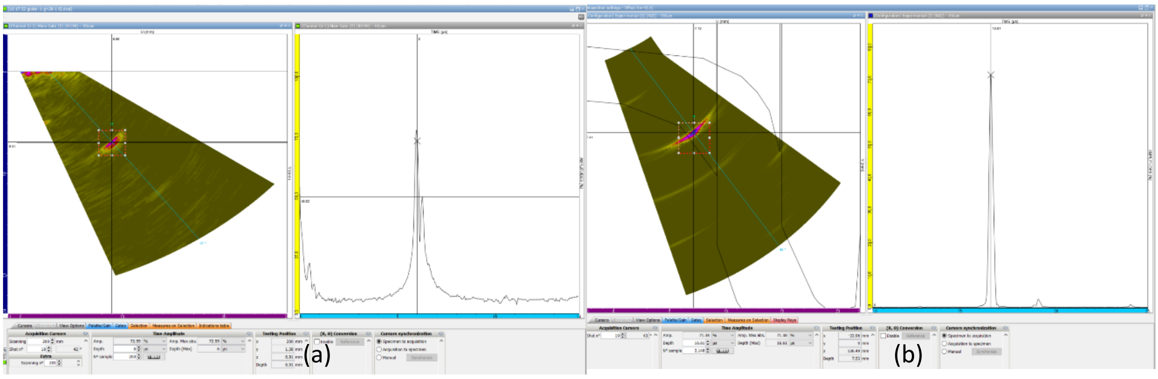

Figure 9-4 Result S scans test case 4 obtained from physical experiment (a) and simulation (b).

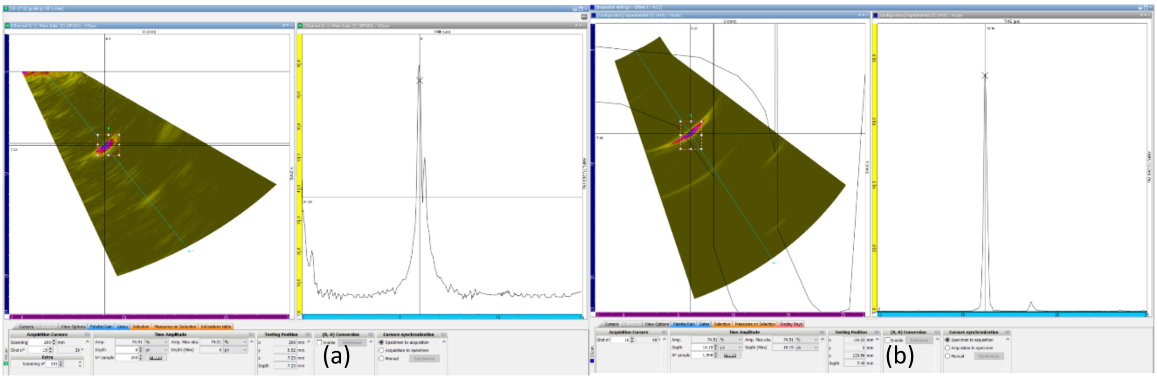

Figure 9-5 Result S scans test case 5 obtained from physical experiment (a) and simulation (b).

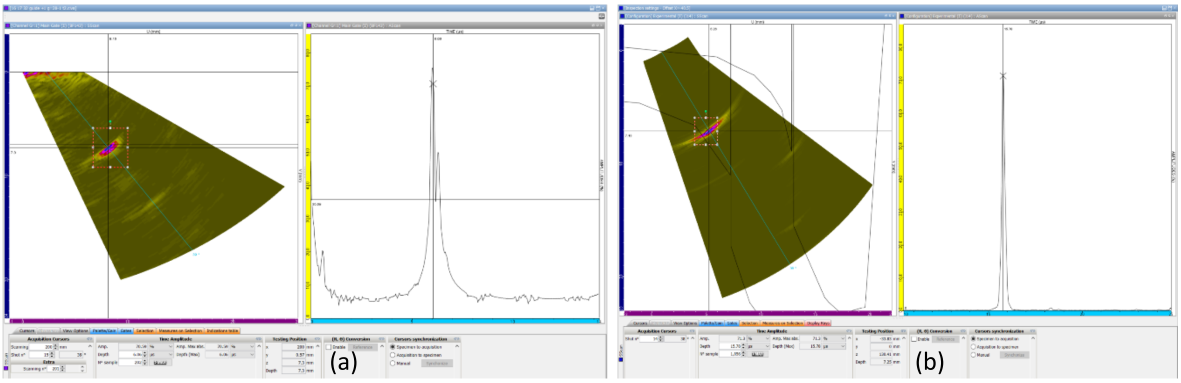

Figure 9-6 Result S scans test case 6 obtained from physical experiment (a) and simulation (b).

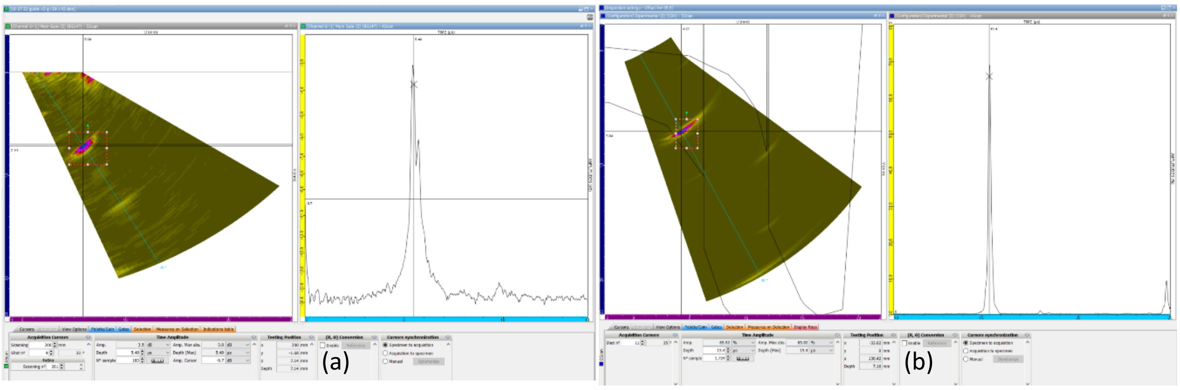

Figure 9-7 Result S scans test case 7 obtained from physical experiment (a) and simulation (b).

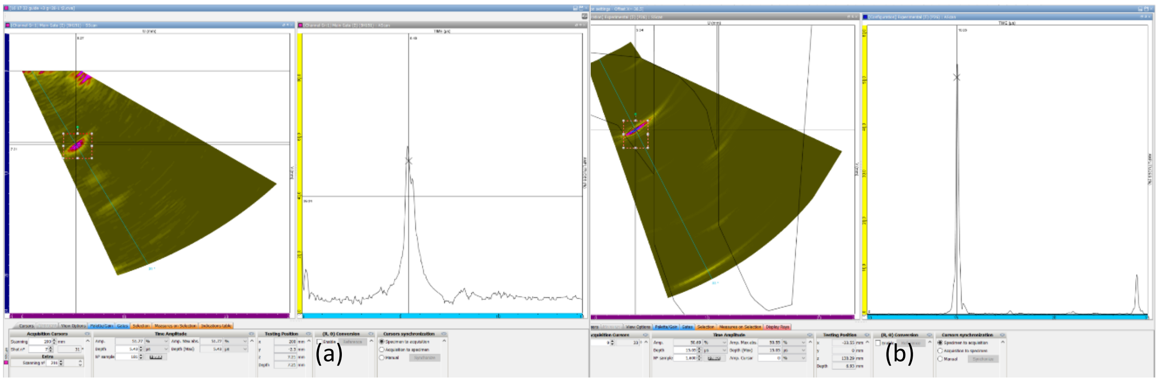

Figure 9-8 Result S scans test case 8 obtained from physical experiment (a) and simulation (b).

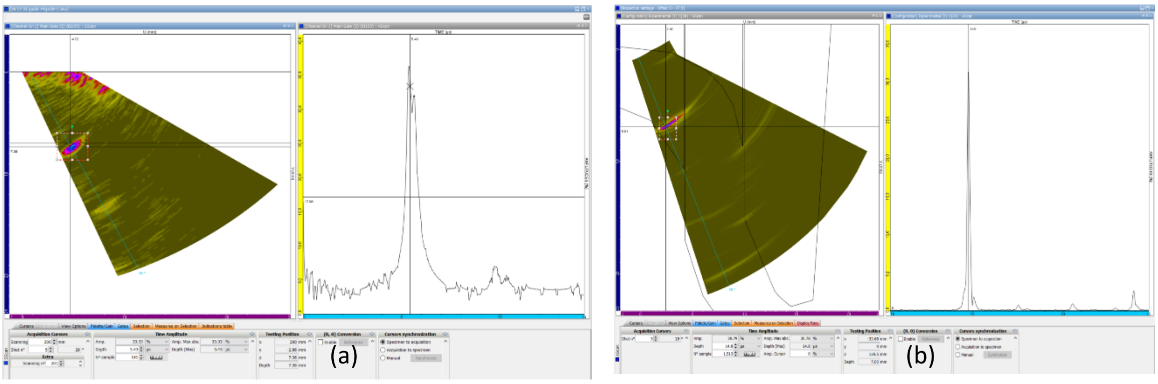

Figure 9-9 Result S scans test case 9 obtained from physical experiment (a) and simulation (b).

Appendix A.2 Results S scans using elements 8 to 23

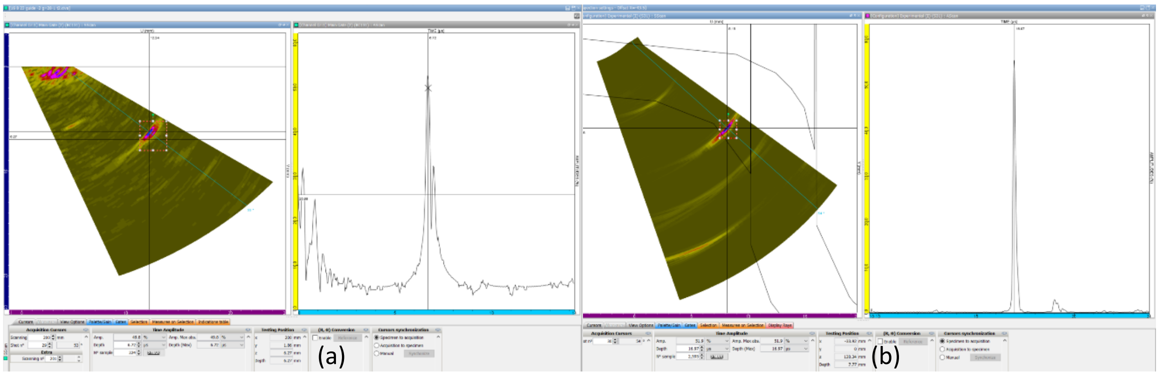

Figure 9-10 Result S scans test case 14 obtained from physical experiment (a) and simulation (b).

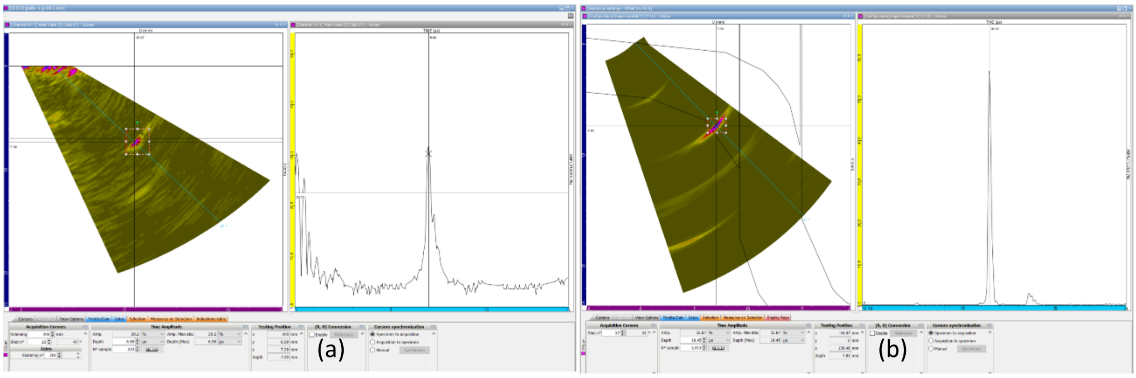

Figure 9-11 Result S scans test case 15 obtained from physical experiment (a) and simulation (b).

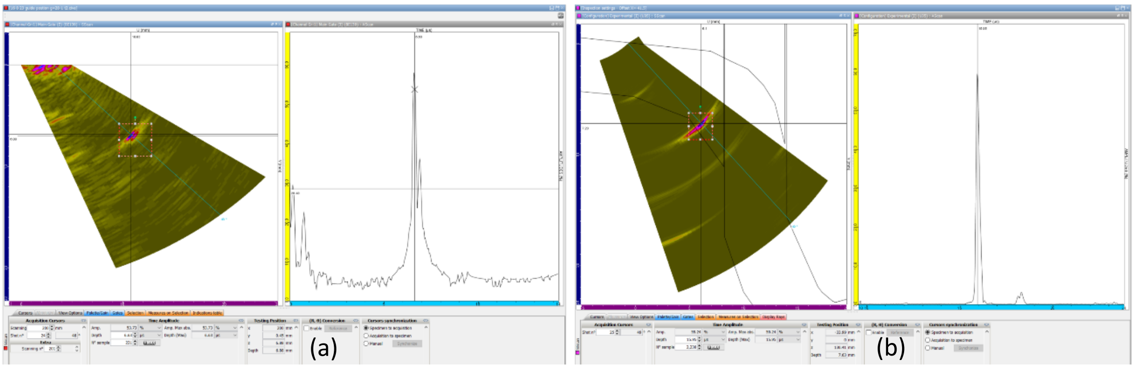

Figure 9-12 Result S scans test case 16 obtained from physical experiment (a) and simulation (b).

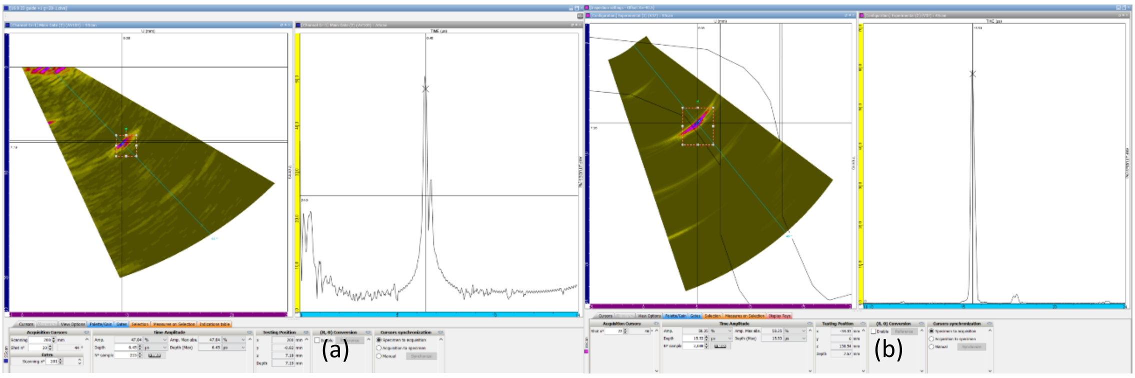

Figure 9-13 Result S scans test case 17 obtained from physical experiment (a) and simulation (b).

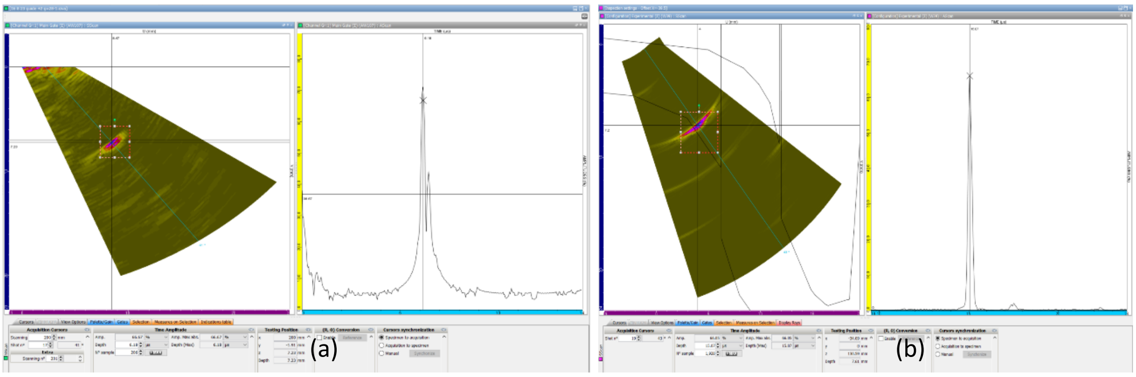

Figure 9-14 Result S scans test case 17 obtained from physical experiment (a) and simulation (b).

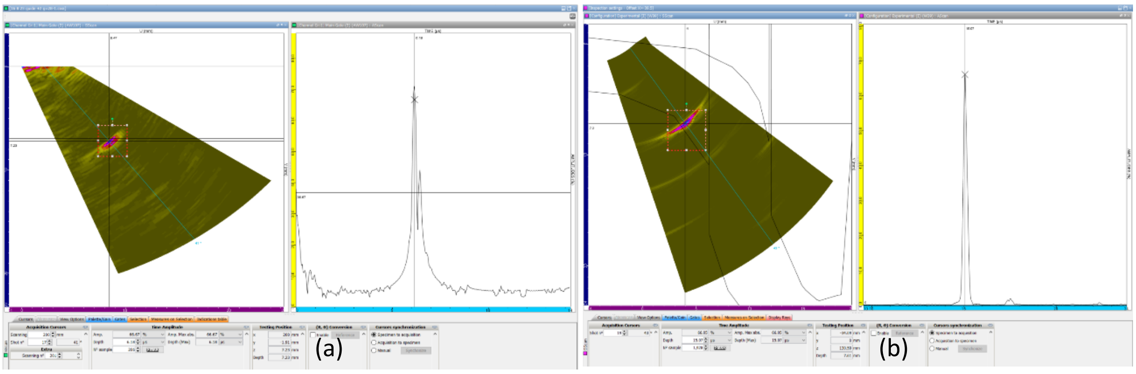

Figure 9-15 Result S scans test case 18 obtained from physical experiment (a) and simulation (b).

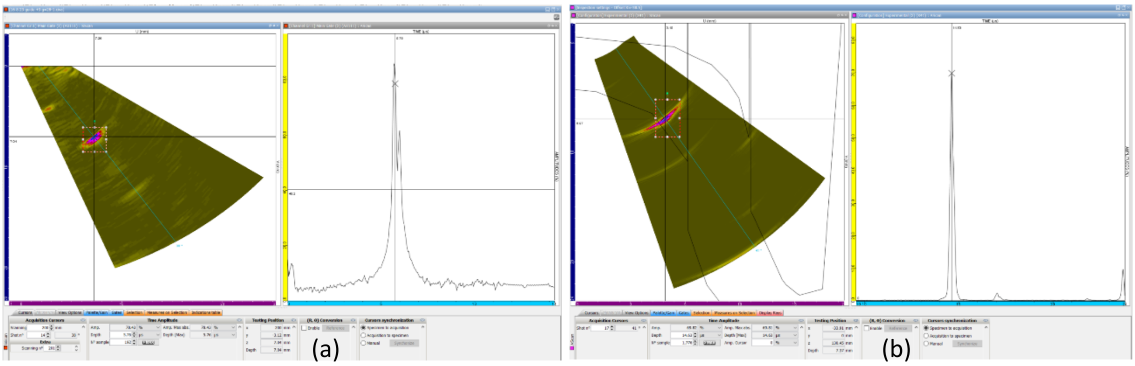

Figure 9-16 Result S scans test case 19 obtained from physical experiment (a) and simulation (b).

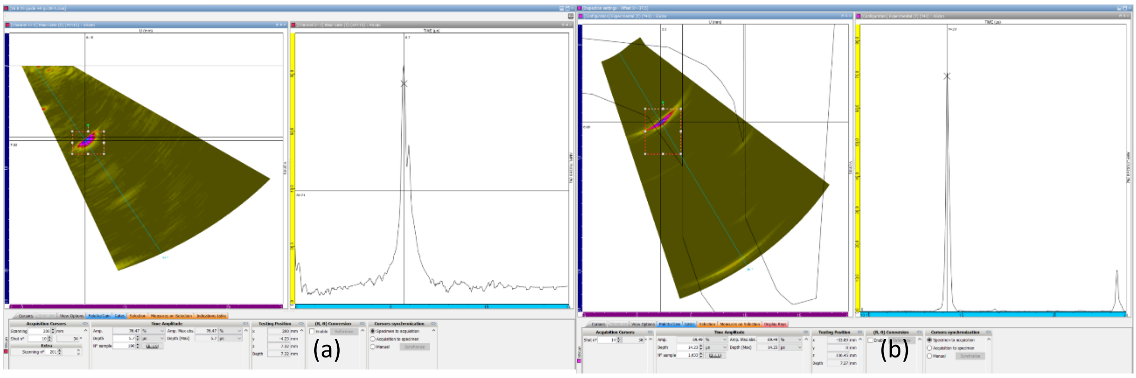

Figure 9-17 Result S scans test case 20 obtained from physical experiment (a) and simulation (b).

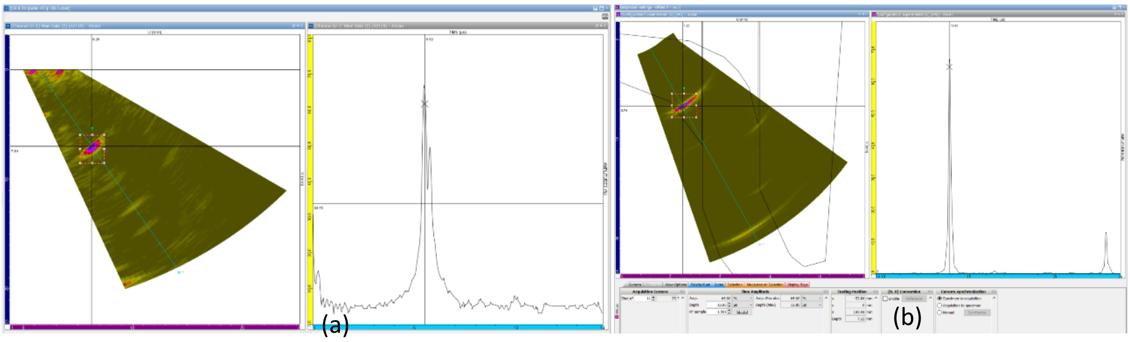

Figure 9-18 Result S scans test case 21 obtained from physical experiment (a) and simulation (b).

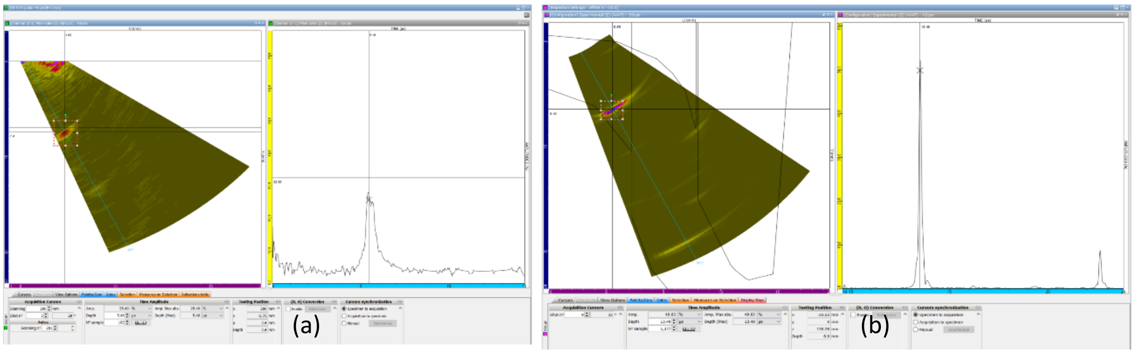

Figure 9-19 Result S scans test case 22 obtained from physical experiment (a) and simulation (b).

Appendix A.3 Results S scans using elements 1 to 16

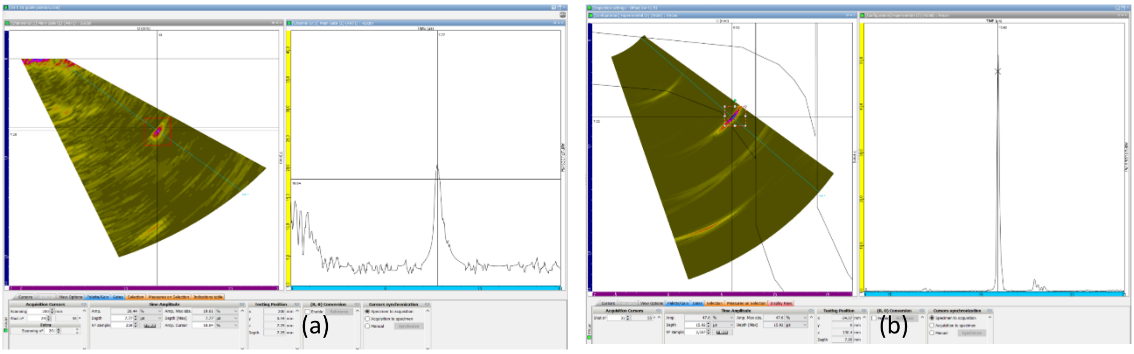

Figure 9-20 Result S scans test case 27 obtained from physical experiment (a) and simulation (b).

).

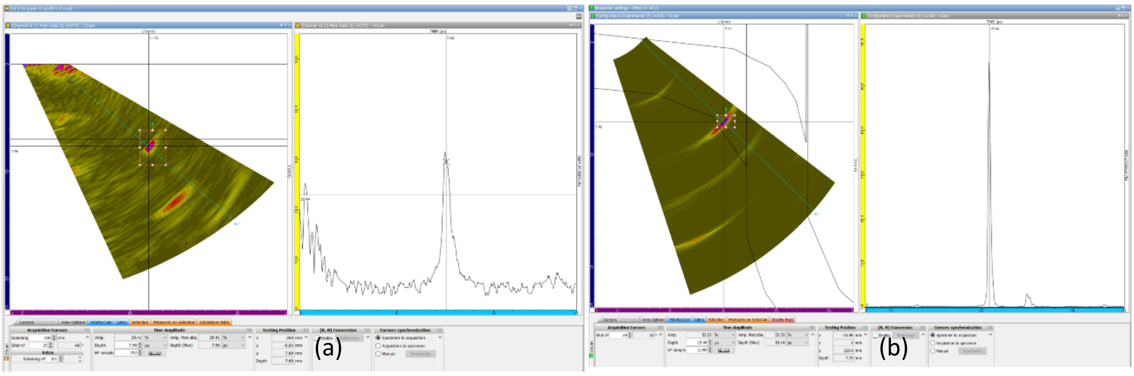

Figure 9-21 Result S scans test case 28 obtained from physical experiment (a) and simulation (b).

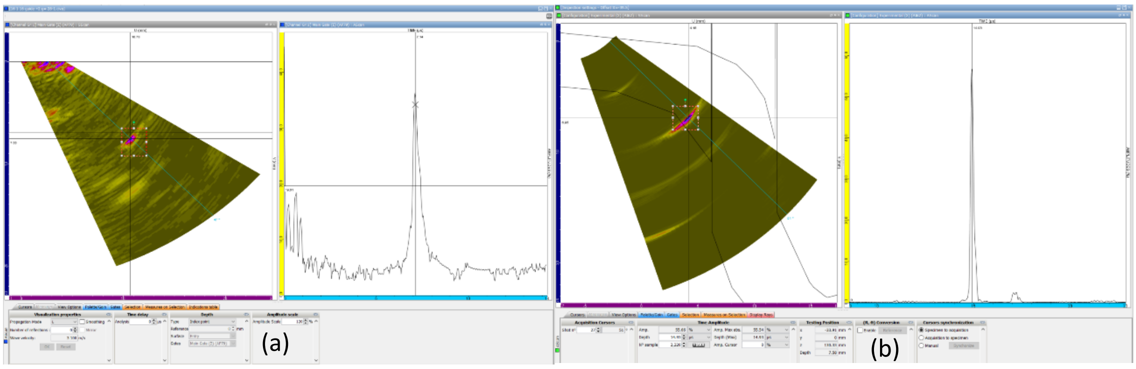

Figure 9-22 Result S scans test case 29 obtained from physical experiment (a) and simulation (b).

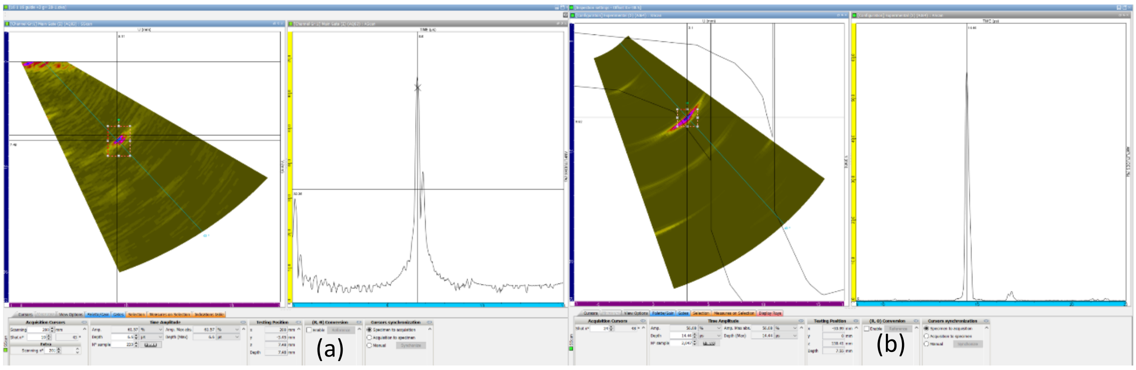

Figure 9-23 Result S scans test case 30 obtained from physical experiment (a) and simulation (b).

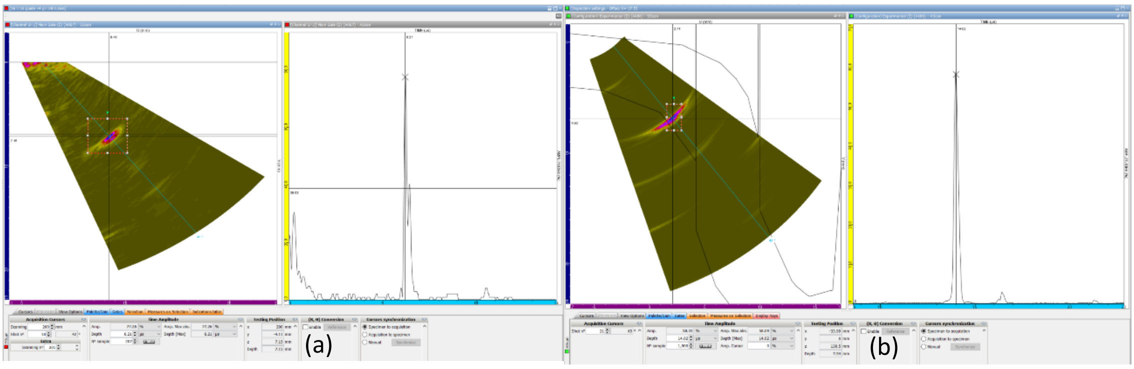

Figure 9-24 Result S scans test case 31 obtained from physical experiment (a) and simulation (b).

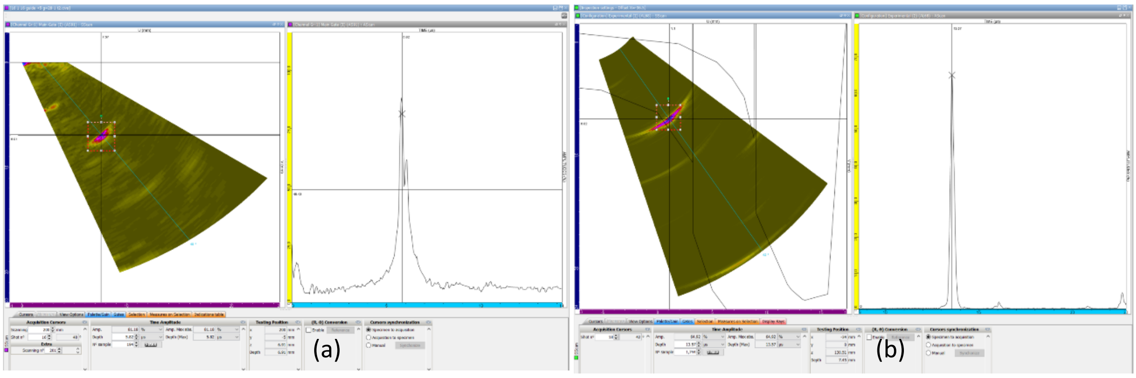

Figure 9-25 Result S scans test case 32 obtained from physical experiment (a) and simulation (b).

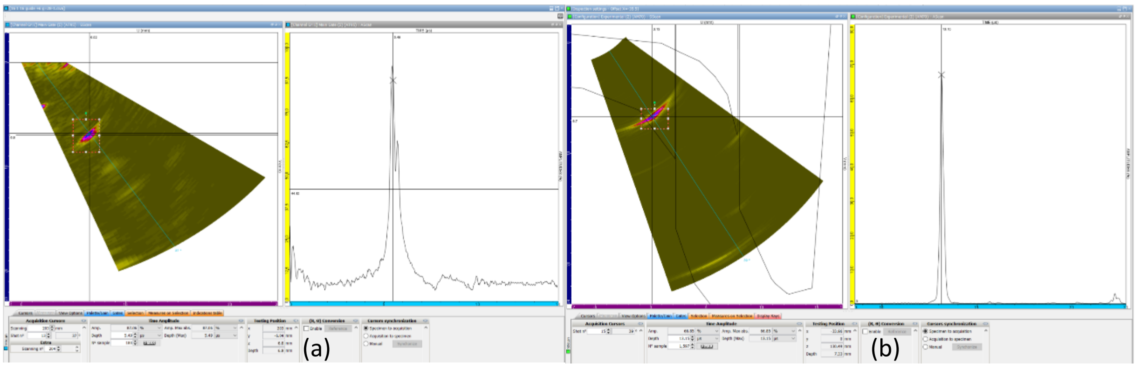

Figure 9-26 Result S scans test case 33 obtained from physical experiment (a) and simulation (b).

Appendix B Variation studies

In this appendix the effect of other parameters that influences the results are being analysed. The largest effect encountered is the wobbling effect. Furthermore the effect of the guide and the influence of the notch parameters are analysed.

Appendix B.1 Influence of the wobble

Since there is a large mismatch between the curvature of the wedge and the curvature of the specimen, a wobble occurs during the performance of the experiment. The definition of the wobble is shown in Figure 9-27. To analyse this effect a variation study was performed where the squint angle was varied. In ideal condition the squint angle is 0 degrees. In the variation study this angle is varied from 0 to 5 degrees. The definition of the squint angle is shown in Figure 9-28. The array settings are kept constant using an aperture size of 16 elements, using elements 17 to 32.

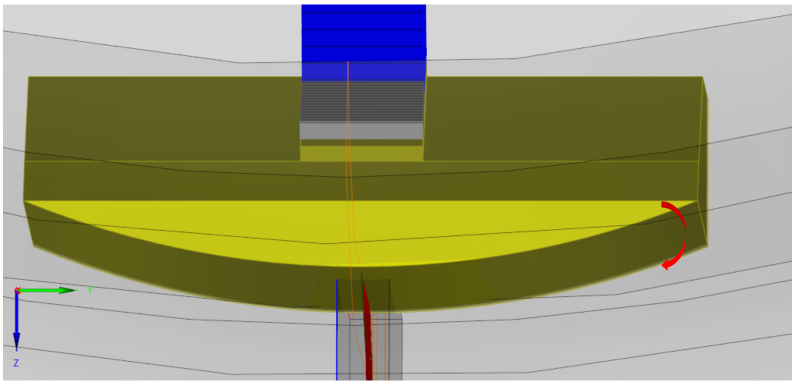

Figure 9-27 Definition of the wobble.

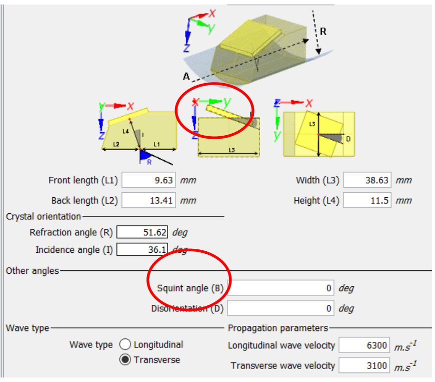

Front length (L1) 9.63 mm
Back length (L2) 13.41 mm
Width (L3) 38.63 mm
Height (L4) 11.5 mm

Crystal orientation
Refraction angle (R) 51.62 deg
Incidence angle (I) 36.1 deg

Other angles
Squint angle (B) 0 deg
Disorientation (D) 0 deg

Wave type
Wave type ○ Longitudinal
● Transverse

Propagation parameters
Longitudinal wave velocity 6300 $m.s^{-1}$
Transverse wave velocity 3100 $m.s^{-1}$

Figure 9-28 Definition of the squint angle.

The results of the variation study can be seen in Figure 9-29. It can be seen that the squint angle has a large influence of the signal return at the flaw location, especially when it gets larger than 1 degree. The S scans and the A scans of the corresponding variation study is shown in Figure 9-30. One way to overcome this problem is to make a wedge that matches the curvature of the aircraft component.

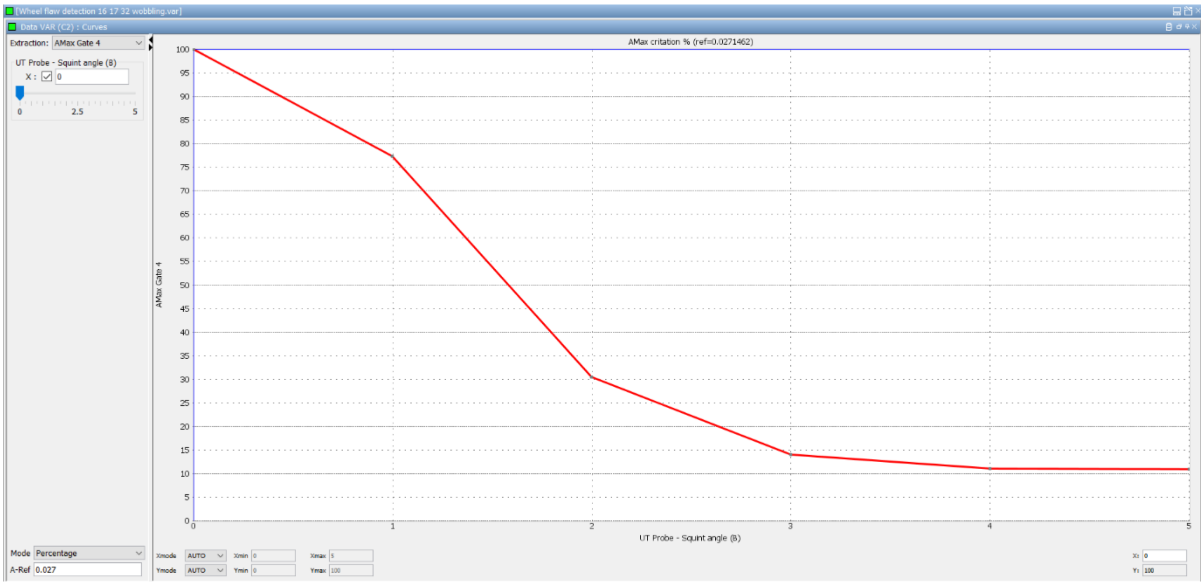
[Wheel flaw detection 16 17 32 wobbling.var]

Data VAR (C2) : Curves

Extraction: AMax Gate 4

UT Probe - Squint angle (B)

X : ☑ 0

Mode: Percentage

A-Ref: 0.027

Xmode: AUTO Xmin: 0 Xmax: 5

Ymode: AUTO Ymin: 0 Ymax: 100

X: 0

Y: 100

Figure 9-29 Variation study: on the horizontal axis the squint angle [deg] is shown and on the vertical axis the percentage of the signal strength with respect to a squint angle of 0 degrees is shown [%].

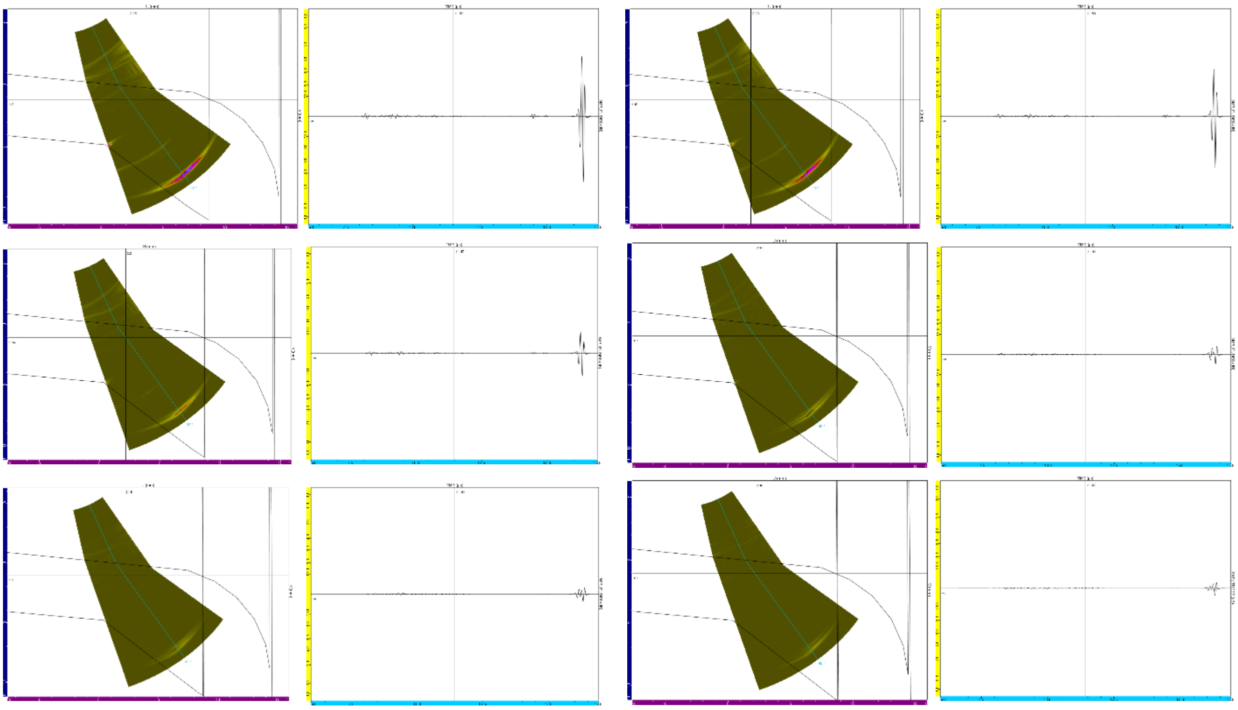

Figure 9-30 S scans and A scans of the variation study with the squint angle varied. The results are calibrated with a squint angle of 0 degrees, so that the signal loss can be visualized.

Appendix B.2 Influence of the guide position

The guide on the wedge is supposed to keep the x-position of the wedge fixed. This is shown in Figure 9-31 and Figure 9-32. The guide can be mounted on either position A or position B as shown in Figure 9-31. To analyse the effect of the guide, a variation study is performed to have the X location of the wedge varied from -44 to -39 mm as visualized in Figure 9-32. The array settings for the variation study is kept constant with an aperture size of 16 elements, using elements 17 to 32.

Figure 9-31 The guide on the wedge. It can be either mounted at position A (shown in the figure) or at position B.

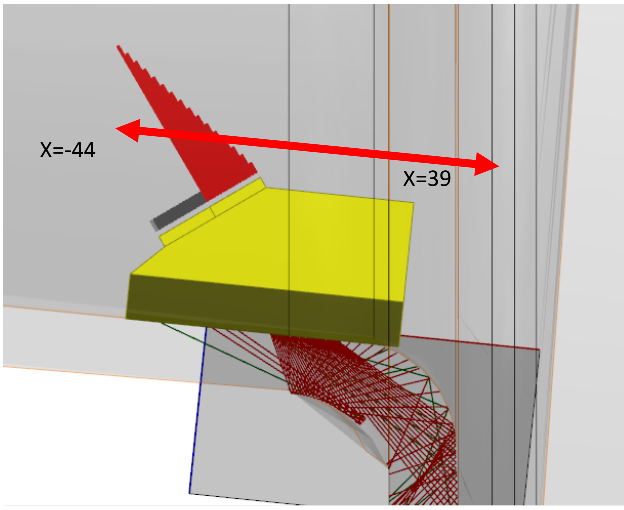

Figure 9-32 X-position of the wedge. The guide is supposed to keep the X-position constant.

The results of the variation study is shown in Figure 9-33. It can be seen that for a higher signal strength, the wedge should actually be position closer to X=-44 mm. However, this is expected to be only for this specific case. A different array setting or a different notch position is expected to give a different result.

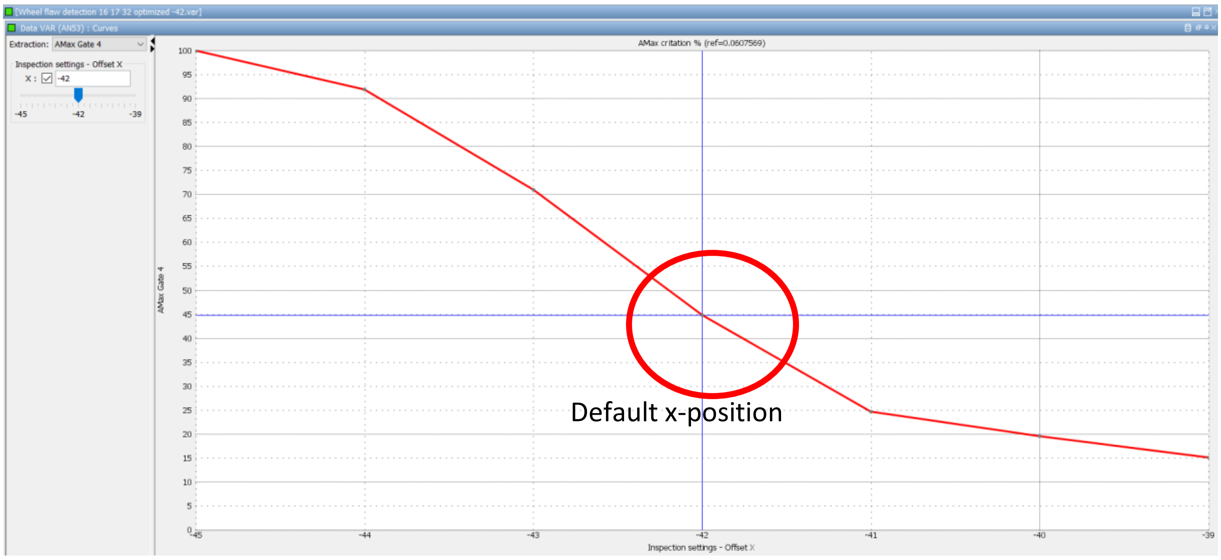

[Wheel flaw detection 16 17 32 optimized -42.var]

Data VAR (AN53) : Curves

Extraction: AMax Gate 4

Inspection settings - Offset X

X : ☑ -42

Figure 9-33 Results variation study with a variable X-position. The horizontal axis shows the X-position of the wedge and the vertical axis shows the percentage of the signal strength with respect to the A-max value.

Appendix B.3 Influence of notch parameters

The notch geometry and position is expected to have a large influence in the detectability of the notch. Therefore three variation studies are performed to analyse the influence of notch parameters. The first variation study is to analyse the crack length, followed by a variation study to analyse the crack height. Finally a variation study is performed to analyse the influence of the position of the notch. The definition of the crack length and crack height are shown in Figure 4-5.

For the variation studies the array settings are kept constant at an aperture size of 16 elements using elements 17 to 32.

Appendix B.4 Effect of the crack length

Using the definition of the crack length from Figure 4-5, the crack length is varied from 0.5 mm to 2.5 mm. The result is shown in Figure 9-34. A strong linear correlation is shown between signal strength and crack length. As expected, it can be seen that the larger the crack length, the stronger the signal response will be.

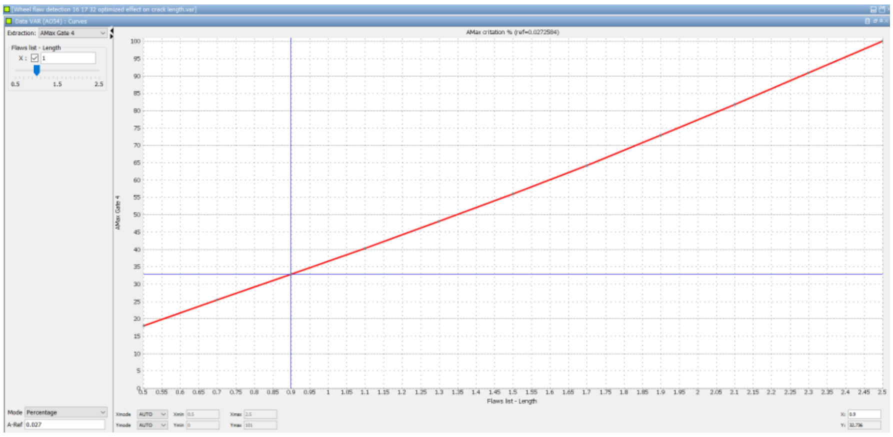

[Wheel flaw detection 16 17 32 optimized effect on crack length.var]

Data VAR (A054) : Curves

Extraction: AMax Gate 4

Flaws list - Length

X : ☑ 1

Mode Percentage

A-Ref 0.027

Xmode AUTO Xmin 0.5 Xmax 2.5

Ymode AUTO Ymin 0 Ymax 101

Figure 9-34 Effect of the crack length. The horizontal axis shows the crack length and the vertical axis shows the percentage of A-max.

Appendix B.5 Effect of the crack height

Using the definition of the crack height from Figure 4-4, a variation study is performed to analyse the effect of the crack height. The crack height is being varied from 0.6 mm and 1.2 mm. The results are shown in Figure 9-35. Unlike the effect of the crack length, there is not a strong correlation between the crack height and the signal response, apart from between crack height of 1 mm and 1.2 mm. A surprising effect is that there is a small decrease in signal response with an increase in crack height between 0.5 and 1 mm.

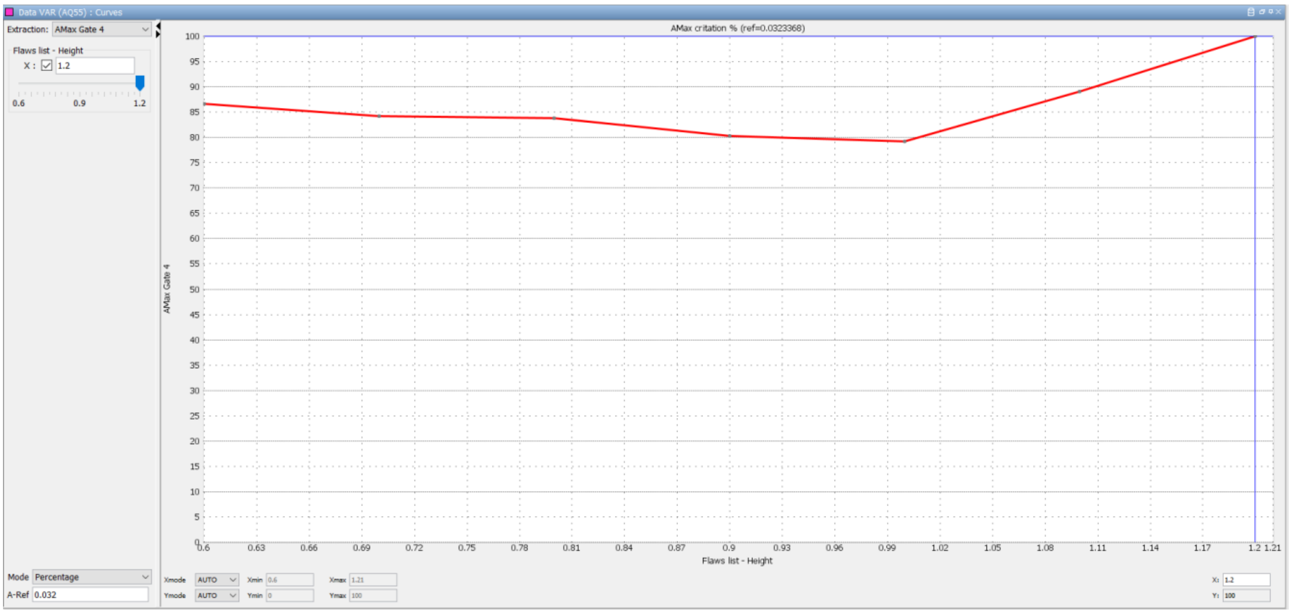

Data VAR (AQ55) : Curves

Extraction: AMax Gate 4

Flaws list - Height

X : ☑ 1.2

Mode Percentage

A-Ref 0.032

Xmode AUTO Xmin 0.6 Xmax 1.21

Ymode AUTO Ymin 0 Ymax 100

X: 1.2

Y: 100

Figure 9-35 Effect of the crack length. The horizontal axis shows the crack height and the vertical axis shows the percentage of A-max.

Appendix B.6 Effect of the crack position

Lastly the effect of the crack position is analysed. The geometry of the notch is kept constant and only the X-position of the notch varies. The notch is set to be normal to the surface of the material at all time. The X-position varies from X=-40 to X=-32, which is basically at the curve of the specimen, as shown in Figure 9-36.

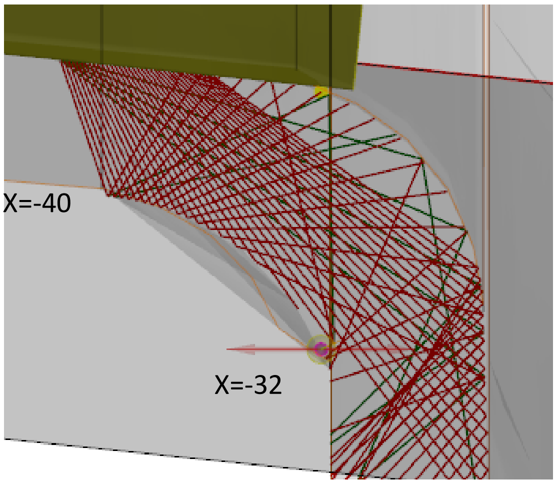

Figure 9-36 Variation of notch positions.

The result of this variation study is shown in Figure 9-37. The signal response is the largest when the notch occurs at X=-33 mm. However this can be different if the aperture settings are change, like using elements at different locations.

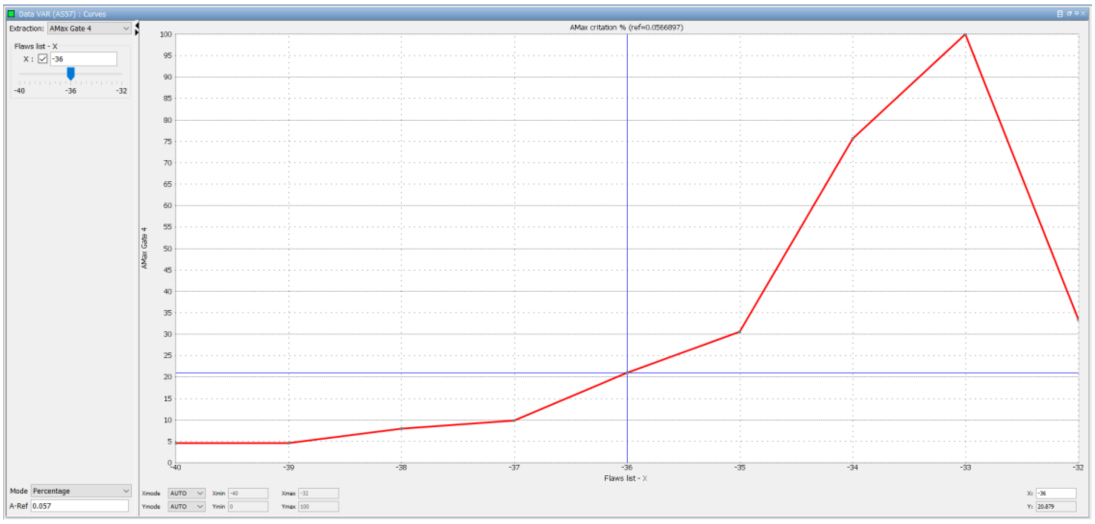

Data VAR (AS57) : Curves

Extraction: AMax Gate 4

Flaws list - X

X : ☑ -36

Mode: Percentage

A-Ref: 0.057

Xmode: AUTO Xmin: -40 Xmax: -32

Ymode: AUTO Ymin: 0 Ymax: 100

X: -36

Y: 20.879

Figure 9-37 Effect of the notch position. The horizontal axis shows the position of the notch and the vertical axis shows the percentage of A-max.

Appendix C Dataset POD analysis

In this appendix the raw data used for the POD analysis is shown. The definition of the variables of the simulations are explained in section 4.3.1.

Appendix C.1 Dataset POD with two variables: flaw length and flaw height

Length [mm]	Height [mm]	Amplitude [%]	Hit/miss
1.022867203	0.57922292	19.23285831	0
1.066781759	0.79403228	30.83984439	0
1.100985646	0.90714836	36.83473676	0
1.143232822	0.80413467	33.9239382	0
1.206819296	0.87013406	39.02568028	0
1.241321921	0.81942844	37.58332191	0
1.273668528	0.75758791	35.14730921	0
1.294626474	0.85444939	41.45646325	1
1.334175825	0.71959066	34.48948742	0
1.407423139	0.87669796	46.55808592	1
1.457442403	0.74496281	39.8723122	0
1.477561593	0.71242476	37.83076237	0
1.504928112	0.56029922	27.93963425	0
1.547639728	0.73107541	41.70624874	1
1.605077028	0.64609772	36.00619877	0
1.636023164	0.81079149	50.63681075	1
1.685672879	0.9405418	60.95811438	1
1.70911622	0.65516156	39.36797237	0
1.775503993	0.77064735	52.07428565	1
1.83098948	0.86144221	61.70636759	1
1.848312855	0.68121213	45.44716137	1
1.904067993	0.61580008	39.50727912	0
1.94444859	0.90050769	69.33172639	1

1.967099309	0.89641458	70.03193769	1
2.013142824	0.59724754	41.04240678	1
2.065424919	0.9223094	76.43699168	1
2.124515533	0.86455458	74.16812273	1
2.133703232	0.67411292	52.56559413	1
2.193879604	0.7011376	57.86081728	1
2.227762938	0.58685929	45.8017517	1
2.256623745	0.76579148	68.36186139	1
2.319013834	0.62199438	50.11837452	1
2.341524363	0.84952867	81.84803793	1
2.409208059	0.72401363	68.20698961	1
2.451581001	0.73835528	71.55590619	1
2.499019146	0.94795018	97.06360407	1
2.54069829	0.93264335	98.0239457	1
2.572469234	0.63426614	58.64457538	1
2.595116854	0.83729291	90.00068292	1
2.637339115	0.92531627	101.6033384	1
2.679915905	0.88513339	98.60012394	1
2.711006165	0.69040149	71.8112223	1
2.773608446	0.68624687	72.50913634	1
2.813468695	0.66045624	68.59954924	1
2.857331038	0.75073582	85.53490998	1
2.888273716	0.83176929	98.83499871	1
2.922158241	0.62853688	64.15547373	1
2.970391989	0.91635168	111.6460237	1
3.024438143	0.56763929	57.79580141	1
3.07620573	0.55476791	56.32478457	1
3.111575603	0.79692793	98.36997741	1
3.155632973	0.6674509	73.28529102	1
3.177031279	0.59617066	58.63750688	1
3.233001709	0.57594514	57.29347945	1
3.259294987	0.70419282	80.64107253	1
3.310296774	0.60888416	60.85758886	1

3.362478256	0.64296448	68.16724363	1
3.408908129	0.82794982	104.0757849	1
3.453379393	0.77730733	94.18700177	1
3.495072365	0.78645766	95.46018182	1

Appendix C.2 POD dataset with 3 variables: flaw length, flaw height and flaw position within the region of interest

Length [mm]	Pos [mm]	Height [mm]	Amplitude [%]	Hit/miss
1.042913437	-37.9183728	0.878322899	32.15744614	0
1.067710757	-38.2164416	0.659952283	25.50918322	0
1.093984485	-37.5699289	0.557315111	23.60134505	0
1.126890182	-33.7641613	0.71576637	22.44493136	0
1.141309142	-34.6891393	0.732027054	32.27979566	0
1.188282132	-33.8527315	0.596471787	20.88866507	0
1.216643333	-34.9324447	0.586192668	26.98315881	0
1.225507617	-33.0724898	0.734917283	22.33781255	0
1.276240826	-35.382711	0.661645293	31.00330822	0
1.321345329	-33.4231335	0.697866678	23.34065831	0
1.350335956	-37.8363584	0.626009107	33.17360265	0
1.408267498	-34.859632	0.563171864	31.92548951	0
1.435295463	-38.7303662	0.683019102	24.50239486	0
1.453206301	-33.9496426	0.702216685	31.61882886	0
1.505802155	-33.3624797	0.711987197	27.01506019	0
1.64155829	-38.6430067	0.565683961	29.01075551	0
2.315765619	-33.3027533	0.584580123	23.38937126	0
1.015244842	-36.0543036	0.752903104	41.51925349	1
1.285126567	-35.0983906	0.830932617	37.69431645	1
1.38005054	-36.6051331	0.782920837	46.00999065	1
1.484405637	-37.0754384	0.933292568	55.07728037	1
1.534813643	-38.6497354	0.915088236	36.04742054	1
1.559971333	-35.6982102	0.676769972	52.02720372	1

1.587171793	-33.6810278	0.787571311	39.76452714	1
1.633916497	-37.615729	0.879713953	56.97158571	1
1.6937989	-36.8192064	0.819232106	58.40419863	1
1.695533037	-35.8982745	0.581016064	60.81566979	1
1.730448365	-36.7749756	0.855241716	61.45875041	1
1.761507273	-36.2695818	0.927349865	77.40450211	1
1.793516755	-37.7085291	0.722804904	49.63198056	1
1.808165073	-37.1426683	0.794335663	57.60497581	1
1.842182517	-37.4926875	0.864058137	62.03514357	1
1.881009102	-34.0067984	0.942363262	64.63202911	1
1.905180931	-34.3616061	0.63553077	44.37130709	1
1.916797042	-36.7230146	0.644972086	49.92643132	1
1.964866519	-35.6267829	0.848576009	68.51316549	1
1.988226652	-34.1596623	0.809312701	60.95269838	1
2.006196737	-36.8968216	0.623645306	49.97811734	1
2.051289082	-33.1890233	0.930375457	75.04150271	1
2.078161001	-35.2617528	0.552678943	46.18472587	1
2.099479914	-38.8987623	0.762852967	36.13934924	1
2.131257057	-36.5137999	0.739600778	69.74072506	1
2.15677762	-35.005573	0.888906419	71.71226809	1
2.16719985	-34.3817335	0.575922728	45.43778128	1
2.202502251	-36.3191481	0.923068583	94.36527124	1
2.225985289	-37.2503221	0.601633906	55.74358197	1
2.266413212	-37.2950073	0.892336249	80.63331628	1
2.295891762	-38.2338323	0.683919072	60.45592137	1
2.355727673	-38.7943628	0.828800559	49.72627816	1
2.386652231	-32.812165	0.743016779	44.59918501	1
2.39304018	-33.4875946	0.780435622	63.43644972	1
2.43376565	-34.7543528	0.708098888	68.2683184	1
2.46687007	-32.6665632	0.812363744	57.51881175	1
2.474143505	-35.8498999	0.688591957	95.26219697	1
2.520057201	-38.3856056	0.641805887	62.72242619	1
2.55155015	-38.5114658	0.763778806	62.59685526	1

2.575833082	-38.9491421	0.903719068	46.42318266	1
2.584842682	-33.1558557	0.884291172	89.1285638	1
2.633158207	-36.372249	0.607527793	83.75423077	1
2.664669037	-35.991888	0.6543051	102.9567363	1
2.671241522	-32.8636695	0.860651851	78.58790744	1
2.701052666	-38.0499906	0.872614741	91.19669214	1
2.73710084	-36.1199058	0.568093479	97.59324483	1
2.758665085	-36.9900168	0.803415656	99.73853444	1
2.782949924	-35.1815162	0.632902682	71.92578453	1
2.819179296	-38.1027958	0.772217095	84.63992331	1
2.834945202	-32.9162885	0.837731361	81.20284631	1
2.880454063	-35.0880559	0.695906401	76.31133478	1
2.889574528	-36.4690104	0.79604435	110.2540642	1
2.929269314	-32.6863891	0.823839843	74.50268723	1
2.971953869	-33.5435836	0.591842949	36.13160732	1
2.979536772	-38.4694059	0.801204622	83.43191674	1
3.008889437	-37.2021115	0.617239654	86.23974446	1
3.050862551	-35.5366124	0.726411223	94.03807613	1
3.063153982	-37.7208268	0.75842911	100.9266632	1
3.109799862	-36.1639655	0.609720171	105.9144831	1
3.137426853	-35.7591591	0.868926108	124.8487868	1
3.144814253	-34.5957892	0.911760271	110.6190376	1
3.1724298	-38.0001617	0.748088718	102.0742437	1
3.207321644	-34.549162	0.947713912	116.2806287	1
3.246218204	-34.0551766	0.907855034	109.9965225	1
3.253668547	-32.9734284	0.673077643	55.60251287	1
3.293483973	-34.2757748	0.651501954	70.17619717	1
3.319112778	-35.4647651	0.615185618	83.13911848	1
3.354592323	-34.2086932	0.840019345	104.4329924	1
3.363428354	-33.6177786	0.940797925	130.7270275	1
3.41560936	-34.4916821	0.666968823	75.07544584	1
3.419452667	-38.3228908	0.772944391	89.60421651	1
3.463053226	-35.3645284	0.844719112	92.92285794	1

3.488511324	-37.4286506	0.898329616	125.2288524	1